Adaptive protein synthesis in genetic models of copper deficiency and childhood neurodegeneration.

Alicia R. Lane[1], Noah E. Scher[1*], Shatabdi Bhattacharjee[2*], Stephanie A. Zlatic[1], Anne M. Roberts[3,4], Avanti Gokhale[1], Kaela S. Singleton[1], Duc M. Duong[3], Mike McKenna[5], William L. Liu[6], Alina Baiju[6], Felix G Rivera Moctezuma[7], Tommy Tran[2], Atit A. Patel[2], Lauren B. Clayton[9], Michael J. Petris[8], Levi B. Wood[7], Anupam Patgiri[6], Alysia D. Vrailas-Mortimer[9], Daniel N. Cox[2], Blaine R. Roberts[3,4], Erica Werner[1#], Victor Faundez[1#]

[1]Department of Cell Biology, Emory University, Atlanta, Georgia, USA, 30322; [2]Neuroscience Institute, Georgia State University, Atlanta, GA 30303; [3]Department of Biochemistry, Emory University, Atlanta, Georgia, USA, 30322; [4]Department of Neurology, Emory University, Atlanta, Georgia, USA, 30322; [5]NanoString Technologies, 530 Fairview Ave N, Seattle, WA 98109; [6]Department of Pharmacology and Chemical Biology, Emory University, Atlanta, Georgia, USA, 30322; [7]George W. Woodruff School of Mechanical Engineering and Parker H. Petit Institute for Bioengineering and Bioscience, Georgia Institute of Technology, Atlanta, GA 30332; [8]Departments of Biochemistry, Molecular Microbiology and Immunology, Ophthalmology, and Christopher S. Bond Life Sciences Center, University of Missouri, Columbia, MO, 65211; [9]Department of Biochemistry & Biophysics and Linus Pauling Institute, Oregon State University, Corvallis, OR 97331

[*]These authors contributed equally.
[#]Co-corresponding author

Email: vfaunde@emory.edu, ewerner@emory.edu

Author Contributions: Conceptualization, VF, AL, and EW; Methodology and Validation, AL, SB, SZ, AR, DD, LW, AP, AV, DC, BR, EW; Formal Analysis, VF, AL, and MM; Investigation, VF, AL, NS, SB, SZ, AR, AG, KS, DD, MM, WL, AB, FRM, TT, AP, LC, EW; Resources, VF, AL, SB, DC, MP, AV,; Writing – Original Draft, VF, AL, SB, MM, FRM, AV; Writing – Review & Editing, VF, AL, SB, SZ, AG, KS, MM, FRM, MP, LW, AP, AV, DC, EW; Visualization, VF, AL, SB, MM, AV; Supervision, VF, EW, LW, AP, AV, DC, BR; Funding Acquisition, VF, AL, KS, DC, AP, EW.

Competing Interest Statement: N/A

This PDF file includes:

Main Text
Figures 1 to 7 (with 8 supplementary figures)
Tables 1 to 3 (with 2 supplementary files)

Abstract

Rare inherited diseases caused by mutations in the copper transporters *SLC31A1* (CTR1) or *ATP7A* induce copper deficiency in the brain and throughout the body, causing seizures and neurodegeneration in infancy. The mechanistic underpinnings of such neuropathology remains unclear. Here, we characterized the molecular mechanisms by which neuronal cells respond to copper depletion in multiple genetic model systems. Targeted deletion of CTR1 in neuroblastoma clonal cell lines produced copper deficiency that was associated with compromised copper-dependent Golgi and mitochondrial enzymes and a metabolic shift favoring glycolysis over oxidative phosphorylation. Proteomic and transcriptomic analysis revealed simultaneous upregulation of mTORC1 and S6K signaling, along with reduced PERK signaling in CTR1 KO cells. Patterns of gene and protein expression and pharmacogenomics show increased activation of the mTORC1-S6K pathway as a pro-survival mechanism, ultimately resulting in increased protein synthesis as measured by puromycin labeling. These effects of copper depletion were corroborated by spatial transcriptomic profiling of the cerebellum of *Atp7a*$^{flx/Y}$ *::* *Vil1*$^{Cre/+}$ mice, in which copper-deficient Purkinje cells exhibited upregulated protein synthesis machinery and expression of mTORC1-S6K pathway genes. We tested whether increased activity of mTOR in copper-deficient neurons was adaptive or deleterious by genetic epistasis experiments in *Drosophila*. Copper deficiency dendritic phenotypes in class IV neurons are partially rescued by increased S6k expression or 4E-BP1 (Thor) RNAi, while epidermis phenotypes are exacerbated by Akt, S6k, or raptor RNAi. Overall, we demonstrate that increased mTORC1-S6K pathway activation and protein synthesis is an adaptive mechanism by which neuronal cells respond to copper depletion.

Significance Statement

Copper dysregulation is present in neurodevelopmental, neurodegenerative, and neurological conditions ranging from rare conditions such as Menkes disease and CTR1 deficiency to more common diseases like Alzheimer's, Parkinson's, and amyotrophic lateral sclerosis. However, the precise mechanisms through which copper deficiency leads to pathology and the survival mechanisms by which the brain exhibits resilience remain unknown. We demonstrate that in a human cell line, *Drosophila*, and the mouse cerebellum, copper-depleted neuronal cells exhibit increased protein synthesis through two distinct signaling pathways: mTORC1 activation and decreased PERK (EIF2AK3) activity. This upregulation of protein synthesis facilitates resilience of neuronal cells to copper deficiency, including partial restoration of dendritic arborization. Our findings offer a new framework for understanding copper deficiency-related pathology in neurological disorders.

Introduction

Copper is an essential micronutrient but can be toxic to cells if not regulated appropriately (1, 2). Neurodevelopment has stringent requirements for copper levels and localization within organelles and across tissues and organs, and the expression of copper transporters, chaperones, and copper-dependent enzymes is tightly regulated both temporally and spatially. For example, the copper transporter ATP7A exhibits age-dependent changes in expression in early development in the neocortex, cerebellum, hippocampus, and olfactory bulb (3, 4) and traffics to neuronal processes prior to synaptogenesis (5). A failure of mechanisms controlling copper homeostasis is causative of or associated with a variety of neurodevelopmental and neurodegenerative diseases, which can stem from sources such as increased copper levels due to environmental exposure, mutations impairing the function of copper transporters or chaperones, and/or disturbances in processes upstream or downstream of copper handling pathways (6, 7). Defects in copper homeostasis are linked to dysfunctional neuronal differentiation, organization, migration, and arborization; axonal outgrowth; synaptogenesis; and neurotransmission in multiple brain regions (1, 3, 4, 8-11).

As copper is a redox active metal required for oxidative phosphorylation, it is tightly linked to metabolism and bioenergetics (12). Thus, tissues with high energy demands, metabolic activity, and oxygen consumption, like the brain, are particularly susceptible to copper toxicity as well as depletion of copper (9). Neurodevelopment is a particularly vulnerable time due to the high energy consumption and transitions in metabolism by the brain during this period (13). While the fetal brain produces energy by glycolysis, after birth there is a shift toward a reliance on mitochondrial respiration; brain consumption of glucose and oxygen in humans peaks at age 5, nearly doubling the consumption of the adult brain (14-17). This transition from glycolysis to oxidative phosphorylation is in part cell-autonomous, as it is also observed in differentiating neurons and muscle cells in culture (18-21) and is necessary for neurodevelopment (19, 22-24). In fact, aberrant hyperglycolytic metabolism in neurons causes mitochondrial redox stress and induces neuronal dysfunction and damage in vitro and in vivo (25).

Mutations affecting copper homeostasis provide an opportunity to understand how copper-dependent mechanisms and metabolism interact to drive brain development. For example, mutations affecting the copper transporter ATP7A cause conditions of varying severity and age of onset but which all present with prominent neurological symptoms (OMIM: 309400, 304150, 300489; 26). In its most severe form, Menkes disease, overt neurological symptoms and neurodegeneration appear between 1-3 months of age (26-29). Similar to humans, most Menkes mouse models exhibit substantial neurodegeneration by postnatal days 10 to 14, typically culminating in death prior to weaning at day 21 (26, 30-35). This delay in Menkes disease onset determines the window when copper supplementation can be effective in mice and humans (26, 30-32, 36-39). These differences in ATP7A-related disease severity and the timing of onset after birth have been attributed solely to the nature of the ATP7A genetic defect. However, whether this delay in disease appearance is also determined by increasing neurodevelopmental demands for copper and/or neurodevelopmental-sensitive mechanisms conferring resilience to copper depletion has not been considered.

Here, we sought to identify cell-autonomous mechanisms in neurons downstream of copper depletion. We generated *SLC31A1*-null cells that lack the ability to import copper through the plasma membrane copper transporter CTR1. *SLC31A1* genetic defects (OMIM: 620306) cause symptoms similar to Menkes disease, including neurodegeneration and seizures (40, 41). We discovered that these copper-deficient cells have defects in Complex IV, producing reduced ATP-dependent and basal respiration concurrent with increased glycolysis. Using multiomics approaches, we discovered that mTORC1 signaling pathway activity was upregulated, with the most dramatic change being a decrease in levels of DEPTOR, an mTOR inhibitor (42). Among the mTOR substrate proteins, we identified increased phosphorylation of Ribosomal Protein S6

(RPS6). Concomitantly, we also identified decreased expression and phosphorylation of EIF2AK3 (PERK, eukaryotic translation initiation factor 2 alpha kinase 3) in CTR1 mutant cells. The convergence of these changes in RPS6 and PERK represents the modification of two distinct pathways involved in regulation of protein synthesis in CTR1 KO cells. Indeed, CTR1-null cells had increased protein synthesis as measured by puromycin incorporation. Similarly, copper-deficient *Atp7a*$^{flx/Y}$ *:: Vil1*$^{Cre/+}$ mice upregulate protein synthesis machinery transcripts and increase expression of insulin and phosphorylation of the insulin-like growth factor receptor 1 (IGF1R). Based on our pharmacogenomics in cells and *Drosophila* genetics, which demonstrate a partial rescue of dendritic phenotypes by S6k overexpression or Thor RNAi, we conclude that mTOR activation and upregulation of protein synthesis is an adaptive mechanism engaged in response to copper depletion. Our results show a novel convergence of two mechanisms modulating protein synthesis machinery that increase cellular resilience to genetic defects causing neurodevelopmental and neurodegenerative phenotypes.

Results

Metabolic phenotypes in a cell-autonomous model of copper deficiency

To establish a cell-autonomous model of copper deficiency, we generated *SLC31A1* null (hereafter referred to as CTR1 KO) SH-SY5Y clonal cells by CRISPR genome editing (Fig. S1). *SLC31A1* encodes the copper importer CTR1, for which expression was abolished after CRISPR genome editing (Fig. 1A, Fig. S1A). CTR1 KO clones were characterized by their increased resistance to copper (Fig. S1B) and reduced expression of the copper-dependent Golgi enzyme dopamine-β-hydroxylase (DBH, Fig. 1A). We confirmed that relative to wild type cells, whole CTR1 KO cells were selectively depleted of copper but not zinc as measured by inductively-coupled mass spectrometry (ICP-MS) (43, 44) (Fig. 1B, Fig. S1D). Mitochondrial-enriched fractions were also selectively depleted of copper in CTR1 KO cells (Fig. 1B, Fig. S1D). These whole cell and mitochondrial copper phenotypes were rescued by a non-toxic dose of elesclomol (Fig. 1B, Fig. S1C), a small molecule that delivers copper preferentially to the mitochondria (45-49). As copper is essential for the assembly and function of the electron transport chain, particularly Complex IV, we chose to examine the expression of subunits of respiratory chain complexes as well as assembly of supercomplexes. The expression of the copper-dependent mitochondrial Complex IV in CTR1 KO cells was 55% of wild-type levels, while there was no decrease in levels of the other respiratory complexes (Fig. 1C). Using blue native gel electrophoresis with digitonin to preserve supercomplexes, we demonstrated Complex I, III, and IV organization into complexes was compromised in CTR1 KO cells, with more pronounced changes in Complex III and IV. We did not detect modifications of Complex II (Fig. 1D).

To examine the function of the electron transport chain in CTR1 KO cells, we performed Seahorse oximetry using the Mito Stress Test. Consistent with their reduced expression and impaired assembly of Complex IV, CTR1 KO cells exhibited decreased basal and ATP-dependent respiration (0.53x and 0.54x wild-type levels, respectively; Fig. 1E, F, compare columns 1 and 2). These differences attributable to copper deficiency in CTR1 KO cells since they were magnified by treatment with the cell-impermeant copper chelator BCS (Fig. 1F, compare columns 2 and 8), while BCS had no effect on wild-type cells under these conditions (Fig. 1F, compare columns 1 and 7). Copper delivery via elesclomol treatment at a low, non-toxic concentration rescued the respiration defects and increased media acidification (suggesting increased glycolysis) in CTR1 KO cells back to wild type levels (Fig. 1F, compare columns 1, 2, and 4, Fig. S1C, S1E). BCS suppressed the elesclomol-mediated rescue of respiration and acidification phenotypes in CTR1 KO cells (Fig. 1F, compare columns 4 and 6, Fig. S1E), confirming the requirement for copper in this rescue (Fig. S1E). There was no difference in maximal respiration in untreated cells or in response to BCS or elesclomol (Fig. 1F). The increased media acidification by CTR1 KO cells suggests increased glycolysis as compared to wild type cells (Fig. S1E). To characterize the glycolytic parameters of

CTR1 KO cells, we used the Glycolysis Stress Test. CTR1 KO cells exhibited elevated extracellular acidification rate, with increased glycolysis (2.03x wild-type levels), increased glycolytic capacity (1.18x wild-type levels), and reduced glycolytic reserve (0.20x wild-type levels) as compared to wild-type cells (Fig. 1G). CTR1 KO respiration and glycolysis phenotypes correlated with modifications in energy charge (Fig. S1F) (50) and lactate levels (Fig. S1G), which were fully or partially restored by elesclomol (Fig. S1). Together, these findings demonstrate that CTR1 KO cells have compromised copper-dependent Golgi and mitochondrial enzymes. The impairment of the function and organization of the respiratory chain in CTR1 KO cells induces a metabolic shift favoring glycolysis over oxidative phosphorylation.

Unbiased discovery of copper deficiency mechanisms using proteomics and NanoString transcriptomics

Next, we sought to comprehensively identify pathways and signal transduction mechanisms altered by CTR1 KO copper deficiency. We performed quantitative mass spectrometry of the whole cell and phosphorylated proteomes by Tandem Mass Tagging (Fig. 2, Supplementary File 1), focusing on the phosphoproteome as multiple kinases are known to have copper-binding domains which regulate their activity (51, 52). We quantified 8,986 proteins and 19,082 phosphopeptides across wild type cells and two CTR1 KO clones (Fig. 2A volcano plot). The proteome and phosphoproteome did not segregate by genotype in principal component analysis until after thresholding data ($p<0.01$, fold change ≥ 1.5; Fig. 2B, PCA). This indicates discrete modifications of the global proteome and phosphoproteome in CTR1 KO cells. We identified 153 proteins and 138 phosphopeptides with increased expression or phosphorylation in CTR1 KO cells as compared to wild type. Similarly, 57 proteins and 86 phosphopeptides were decreased in expression or phosphorylation in CTR1 KO cells, respectively. These phosphopeptides belong to 161 distinct proteins. Additionally, we identified 184 differentially expressed proteins in a replication TMT proteome in CTR1 KO cells (Fig. 2C, Venn diagram). These two proteome datasets overlapped 9.1 times above what is expected by chance ($p=6.7E-12$, hypergeometric probability) and are enriched 11-fold in a protein interaction network annotated to the GO term generation of precursor metabolites and energy (GO:0006091, $p=1E-31$, hypergeometric probability; Fig. 2C, Venn diagram and interactome). This network of proteins included 9 proteins belonging to Complex IV, such as MT-CO1, MT-CO2, and MT-CO3, all of which were decreased in CTR1 KO cells $\geq$ 1.5-fold ($p<0.01$; Fig. 2D, Complex IV subunits, upper heat map). This finding is consistent with the reduction of Complex IV subunits and supercomplexes by immunoblot and reduced respiration in CTR1 KO cells (Fig. 1C-F). This protein network also included seven Complex IV assembly factor and copper chaperones, such as COX17, whose levels were increased in CTR1 KO cells $\geq$ 1.5-fold ($p<0.01$; Fig. 2D Complex IV assembly factors, bottom heat map). Overall, this suggests copper deficient cells upregulate assembly factors and chaperones for Complex IV in response to impaired assembly of this respiratory complex.

To identify ontological terms represented in the integrated CTR1 KO proteome and phosphoproteome, we queried the NCAST Bioplanet discovery resource with the ENRICHR tool and multiple databases with the Metascape tool (53). Both bioinformatic approaches identified the mTOR signaling pathway (ENRICHR $q=1.4E-3$ and Metascape $q=5.01E-10$) and RHO GTPase cycle as two of the top enriched terms (Fig. 2E, gene ontology). Metascape analysis merged the CTR1 proteome and phosphoproteome into a network of 16 protein-protein interactions, which include these proteins annotated to mTORC1-mediated signaling: EIF4G1, mTOR, RPTOR (Raptor), AKT1S1, DEPTOR, RPS6, and RPS6KA6 (R-HSA-166208 and KEGG hsa04150, $q=1.25E-9$, z-score 22; Fig. 2F, mTORC1 and Fig. 2G, pathway diagram). The most pronounced changes in the steady state mTOR proteome encompassed decreased levels of DEPTOR and increased levels of Ribosomal Protein S6 Kinase A6 (RPS6KA6 or RSK4) (Fig. 2H). DEPTOR is an mTOR inhibitor (42), and RPS6KA6 is a member of the ribosomal S6K (RSK) family. RSK proteins (RSK1-RSK4) are activated downstream of MEK/ERK signaling, while the S6K family (S6K1 and S6K2) is phosphorylated by mTOR, but both families regulate translation through

phosphorylation of ribosomal protein S6 (RPS6) and other related proteins (54, 55). These changes in expression of DEPTOR and RPS6KA6 suggest heightened mTOR activity and RPS6 activation in copper-deficiency. In support of this idea, CTR1 KO cells have increased phosphorylation of mTOR, RPS6, EIF4G1 (eukaryotic translation initiation factor 4 gamma 1), ACLY (ATP-citrate synthase), and UVRAG (UV radiation resistance associated) without changes in their steady state levels (Fig. 2H). The increased phosphorylation of these proteins was in phosphoresidues known to be responsive to mTOR activity, which include: mTOR S1261 and S2448, both correlated with increased mTOR activity and targets for the insulin/phosphatidylinositol 3–kinase (PI3K) pathway and the latter a target of RPS6KB1 (Ribosomal Protein S6 Kinase B1 or S6K1) (56-61); EIF4G1 S984 (62); RPS6 S235, S236, and S240, which are targets of S6K1 and RSK4 (55, 60, 63, 64); and ACLY and UVRAG at S445 and S458, respectively (65-67). We also observed increased protein expression and phosphorylation of AKT1S1 (PRAS40) at T246, a residue that is a target of AKT1 and whose phosphorylation correlates with active mTOR (Fig. 2H, 68). Importantly, we identified increased phosphorylation of RPTOR (Raptor, regulatory-associated protein of mTOR) at the RSK4 target residue S722 (55) but observed no changes in RICTOR (RPTOR-independent companion of MTOR complex 2), suggesting that mTORC1 but not mTORC2 signaling is impacted (69). Beyond the mTOR-S6K pathway, the proteome also revealed decreased protein levels of EIF2AK3 (PERK, eukaryotic translation initiation factor 2 alpha kinase 3), an ER stress response kinase and negative regulator of protein synthesis, which paralleled reduced content of two of its phosphopeptides (Fig. 2H, S551 and S555). While not known to be a direct target of mTOR, EIF2AK3 activity decreases by an AKT1-dependent mechanism (70). We conclude that genetic defects in CTR1 KO cells modify the proteome and signaling pathways converging on mTOR and PERK-dependent signaling mechanisms upstream of protein synthesis pathways (71, 72).

We used NanoString nCounter transcriptomics as an orthogonal approach to proteomics to identify molecular mechanisms downstream of CTR1 KO-dependent copper depletion. We examined steady-state mRNA levels using NanoString panels enriched in genes annotated to metabolic pathways and neuropathology processes, which collectively measure levels of over 1400 transcripts (Fig. S2, Supplementary File 1). We identified 131 metabolic and 37 neuropathology annotated transcripts whose levels were altered in CTR1 KO cells ($q<0.05$ and fold of change ≥ 2, Fig. S2A-C). Metabolic transcripts were enriched in genes annotated to lysosome and mTOR signaling (KEGG, $p<5.8E-6$ and z-score >18, Fig. S2D). Similar ontology analysis but with the combined 171 transcripts whose levels were altered in CTR1 KO cells was enriched in genes annotated to central carbon metabolism in cancer and the PI3K-Akt signaling pathway ($p=2.3E-11$ z-score 8.8. and $p=1.78E-6$ and z-score 9.6, Fig. S2, Supplementary File 1). With the exception of DEPTOR, a negative regulator of mTOR, 14 of the 15 transcripts annotated to mTOR and PI3K-Akt signaling were increased in CTR1 KO cells (Fig. S2C). These transcripts include RRAGC, FNIP1, FNIP2, and MAPK1 (Fig. S2C,E). The copper dependency of these transcripts level changes was demonstrated using the copper chelator BCS. Differences in gene expression between wild type and CTR1 KO cells at baseline were magnified by BCS (Fig. S2A,B). A subset of these genes was sensitive to copper chelation in both wild-type and CTR1 KO cells, including PIK3R1, SLC7A5, and SLC3A2 (Fig. S2B). Collectively, the transcriptome and proteome of CTR1 KO cells provide independent evidence of increased activation of PI3K-Akt and mTORC1-S6K signaling pathways.

Increased steady-state activity of the mTOR-S6K pathway in CTR1 KO cells

To confirm the findings of our proteomic and transcriptomic datasets, we examined steady-state levels of several proteins identified in the CTR1 KO proteome by immunoblot and compared them to the housekeeping protein beta-actin (Fig. 3A). CTR1 KO cells exhibit increased levels of the copper chaperone COX17, as well as reduced levels of DEPTOR and EIF2AK3 (Fig. 3A). However, despite the severe copper depletion in CTR1 KO cells (Fig. 1B), we did not observe changes in the levels of ATP7A or CCS (Fig. 3A), two proteins frequently altered in copper depletion

(73, 74). In agreement with the proteomic profiling of these cells, there was no change in RPTOR or RICTOR expression, both components of mTOR complexes (Fig. 3A).

We tested the hypothesis of heightened mTOR signaling in CTR1 KO cells by measuring the phosphorylation status of mTOR and p70/p85 S6K1. We used serum depletion and serum addition paradigms to inhibit or stimulate, respectively, mTOR-S6K and PI3K-Akt signaling pathway activity (75). We focused on mTOR S2448 and S6K1 T389 phosphorylation as sensors of mTOR signal transduction. mTOR S2448, which we identified in the CTR1 KO phosphoproteome (Fig. 2H), is present in the mTOR catalytic domain, is sensitive to nutrient availability and insulin, and is an S6K target (59, 76-78). The phosphoresidue T389 in S6K1 is phosphorylated by an insulin- and mTOR-dependent mechanism and indicates increased S6K activity (75, 79, 80). Relative to wild type cells, CTR1 KO cells had an increased mTOR and S6K1 phosphorylation at time 0 after an overnight serum depletion paradigm, revealing elevated mTOR activity even in the absence of an mTOR activating stimulus (Fig. 3B, compare lanes 1 and 5). Exposing these cells to serum progressively increased mTOR and S6K1 phosphorylation to a higher degree when comparing CTR1 KO to wild type cells (Fig. 3B, compare lanes 2-4 to 6-8). Additionally, CTR1 KO cells displayed increased phosphorylation of mTOR and S6K1 at baseline (0h in complete media) and over time after removal of serum (Fig. 3C), indicating that the mTOR signaling is resistant to serum deprivation in CTR1 KO cells. These results demonstrate that CTR1 KO cells have heightened activity of the mTOR-S6K signaling pathway.

Activation of the mTOR-S6K signaling pathway is necessary for CTR1 KO cell survival

mTOR signaling is necessary for cell division, growth, and differentiation (75). We asked whether increased mTOR-S6K activation contributes to cell division and growth in CTR1 KO cells by measuring cell survival after pharmacological manipulation of mTOR activity. We reasoned that the increased mTOR signaling in CTR1 KO cells (Figs. 2, 3, S2) would render mutant cells more sensitive to mTOR inhibition as compared to wild type cells. We quantitively assessed whether mTOR inhibition and cellular copper-modifying drugs interacted synergistically or antagonistically in cell survival assays (81). We used the zero-interaction potency (ZIP) model, which assumes there is no interaction between drugs, an outcome represented by a ZIP score of 0 (82). ZIP scores above 10 indicate the interaction between two agents is likely to be synergistic, whereas a value less than -10 is likely to describe an antagonistic interaction (82).

We first tested the individual effect of two activators of the mTOR-S6K signaling pathway, serum or insulin, on cell survival. CTR1 KO cells are more resistant to serum depletion and exhibit a reduced growth response when treated with insulin, which activates Akt and stimulates mTOR activity (75) (Fig. 4A). This is consistent with increased mTOR activation in these cells. We next asked whether serum and the mTOR inhibitors rapamycin and Torin-2 (Fig. S4-1) would interact in a genotype-dependent manner to affect cell survival. Rapamycin is the canonical mTORC1 inhibitor, while Torin-2 inhibits both mTORC1 and mTORC2 with increased specificity and potency (83, 84). Based on our model, a synergistic response between serum and mTOR inhibitors (increased survival beyond the pro-survival effects of serum alone) would indicate that mTOR activity is deleterious for cell survival. Alternatively, an antagonistic response (negation of the pro-survival effect of serum by mTOR inhibition) would suggest cells are dependent on mTOR signaling for survival. Our results supported the latter, as the interaction between serum and either rapamycin or Torin-2 was antagonistic in both control and CTR1 KO cells (Fig. 4B-D, Fig. S4-2A). The antagonism between serum and both rapamycin and Torin-2 was more pronounced in CTR1 KO as compared to wild type cells (ZIP score between -22.1 to -27.7 for wild type and -30.9 to -34.6 for CTR1 mutant cells, Fig. 4C), signifying that inhibiting mTOR is more detrimental to the pro-survival effects of serum in CTR1-null cells.

Importantly, genotype-dependent differences in cell survival after mTOR inhibition were sensitive to pharmacological manipulation of copper levels. mTOR inhibitors in combination with

the copper chelator BCS abrogated ZIP score differences between genotypes (-35.6 to -38.3 for wild-type and -33.8 to -37.9 for CTR1 KO, Fig. 4C, Fig. S4-B,C). Conversely, low doses of elesclomol, which are sufficient to rescue copper content phenotypes and mitochondrial respiration in CTR1-null cells (Fig. 1B,E,F, Suppl Fig. S1D,E), rendered CTR1 KO cells more resistant to increasing concentrations of Torin-2 (Fig. 4E-G, Fig. S4-2D). These pharmacogenetic epistasis studies indicate that CTR1-null cells are more dependent on mTOR activity for their survival in a copper-dependent manner. These findings support a model where the activation of mTOR is an adaptive response in CTR1 mutant and copper-deficient cells.

Interaction between mitochondrial respiration and increased protein synthesis in CTR1 KO cells

CTR1-null cells have increased activity of the mTOR-S6K pathway and decreased content of PERK (EIF2AK3), predicting increased protein synthesis in CTR1 KO cells as compared to wild type. We measured protein synthesis using puromycin pulse labeling of the proteome (85). Indeed, CTR1 KO cells display a 1.5-fold higher content of peptidyl-puromycin species as compared to wild type cells (Fig. 5A, S5A-B). Puromycin incorporation was sensitive to the cytoplasmic protein synthesis inhibitor emetine in both genotypes (Fig. 5A). These results demonstrate increased protein synthesis in CTR1 mutant cells (Fig. 5A, S5A-B). To further explore the mechanism by which mTOR-S6K activation and upregulation of protein synthesis may be an adaptive response by CTR1 KO cells, we tested whether cell survival and mitochondrial respiration were susceptible to protein synthesis inhibition in a genotype-dependent manner. We indirectly inhibited protein synthesis using serum depletion or directly with emetine (Fig. 5A, (86, 87)). While CTR1 KO cell survival was resistant to serum depletion (Fig. 4A), we found a discrete yet significant decrease in cell survival in CTR1 KO cells after emetine addition (Fig. S5C,D).

To measure whole-cell mitochondrial respiration (as defined by its abrogation with a mix of rotenone plus antimycin) over extended periods of time, we employed the Resipher system, which utilizes platinum organo-metallic oxygen sensors (88, 89). In contrast with Seahorse, which requires serum-free media and measures oxygen consumption over a few hours, Resipher allows oximetry over prolonged periods while maintaining cells in their own milieu. We first measured respiration continuously over 48 h in standard media with 10% fetal bovine serum. Respiration increased over time in both genotypes, a reflection of cell number expansion (Fig. 5B1). CTR1 KO cell respiration was 35% of wild type levels (Fig. 5B1), a phenotype that cannot be explained by differences in cell numbers between genotypes (Fig. S5E) and reproducing the respiratory phenotypes observed in Seahorse (Fig. 2E, compare columns 1 and 2, 53% of wild type basal respiration). However, a switch to low serum media decreased mitochondrial respiration in both genotypes (Fig. 5B1). To compare the relative effect of serum depletion on each genotype, we normalized the OCR values to the last time point before serum switch and revealed that CTR1-null cells respire 1.5 times more efficiently than wild type cells during serum depletion (Fig. 5B2). This effect cannot be explained by changes in cell number after switching to low serum (Fig. S5E). These results show that mitochondrial respiration is resistant to serum depletion in CTR1-null cells.

Next, we compared respiration in CTR1 KO and wild type cells treated with fresh complete media containing either vehicle or emetine to directly inhibit cytoplasmic protein synthesis (Fig. 5C-D). First, we observed genotype-dependent effects of vehicle treatment. After the addition of new media, wild-type cells respire at the same rate as before the media switch (Fig. 5C), but CTR1 KO cells rapidly increase respiration, with a brief period where their raw OCR values are even greater than wild-type cells (Fig. 5C1). Relative to the last timepoint before media switch, CTR1 KO cells respire 1.7-fold more efficiently than wild-type cells (Fig. 5C2). Surprisingly, an increase in raw OCR was also observed in CTR1 KO cells after emetine treatment even above what was observed in vehicle-treated KO cells (Fig. 5D1, compare to 3,4 in C1). Normalized wild type cell respiration was inhibited by 40% after emetine treatment (Fig. 5D2). In contrast, the normalized respiration was resistant to emetine in CTR1-null cells (Fig. 5D2). These effects cannot be attributed to differences

in cell number (Fig. S5F). We conclude that CTR1-deficient cell respiration is resistant to direct inhibition of protein synthesis.

Upregulation of protein synthesis machinery in a mouse model of copper deficiency

Next, we wanted to determine whether animal models of copper deficiency would corroborate our observations in CTR1 KO cells that copper depletion increases mTOR-S6K pathway activity and upregulates multiple pathways promoting protein synthesis. To address this question, we performed spatial transcriptomics of the cerebellum of *Atp7a*$^{flx/Y}$ *::* *Vil1*$^{Cre/+}$ mice, a conditional mouse model of Menkes disease. These mice, which lack the copper efflux transporter ATP7A in intestinal enterocytes, are unable to absorb dietary copper, depleting the brain of this metal and inducing subsequent pathology that phenocopies Menkes disease (90). We selected the cerebellum as it is known to be one of the earliest brain regions affected in Menkes disease, with Purkinje cells being particularly affected (1, 91, 92). To focus on mechanisms that could serve as an adaptive response to brain copper deficiency, we chose to study the transcriptome of the cerebellum at postnatal day 10, a presymptomatic timepoint before Purkinje cell death and the rapid onset of high mortality in this model and other Menkes mouse models (31, 32, 90). As Menkes is a sex-linked disease, we focused our analysis on male mice.

We first confirmed that *Atp7a*$^{flx/Y}$ *::* *Vil1*$^{Cre/+}$ mice exhibit systemic copper depletion by ICP-MS as previously reported (Fig. S6-2A, (90)). Next, we used the NanoString GeoMx Digital Spatial Profiler to generate anatomically resolved, quantitative, and PCR amplification-free transcriptomes (93-95) for two regions of interest (ROIs): the Purkinje cell and granular layers of the cerebellum (Fig. 6A). Within these ROIs, we segmented our analyses by GFAP expression to enrich for areas of illumination (AOIs) containing Purkinje cells (GFAP-) or astrocytes in the granular layer (GFAP+) (Fig. 6B, Fig. S6-1A). Using the GeoMx Mouse Whole Transcriptome Atlas (mWTA) and a mouse cerebellar cortex atlas (96), we quantified the transcriptome in these ROIs with a sequencing saturation above 80% (Fig. S6-1B). After data normalization, we analyzed 19,963 genes across 58 AOIs from 4 animals of each genotype selected across different cerebellar folia. 17,453 genes were expressed in 10% of AOIs, and 10,290 genes were expressed in 50% of AOIs (Fig. S6-1C,D). Segmentation by GFAP produced expected patterns of gene expression in Purkinje cell or granular layer AOIs, such that genes associated with Purkinje cells like *Calb1* and *Pcp2* were highly expressed in corresponding AOIs and minimally expressed in AOIs within the granular layer (66-fold enrichment of *Calb1* in Purkinje cell AOIs, Fig. 6C, Fig. S6-1E, Fig. S6-2B,C). Genes associated with granule cells and astrocytes were enriched in AOIs within the granular layer but had little expression in Purkinje cell AOIs (Fig. S6-2B,C). Furthermore, the transcriptome of wild type Purkinje cells was enriched in genes annotated to MitoCarta3.0 knowledgebase ((97), Fig. S6-2F), metabolic ontologies including oxidative phosphorylation (MSigDB p6.5E-43, Fisher exact test followed by Benjamini-Hochberg correction) and the mTOR pathway (MSigDB p2.4E-12) as compared to the granular layer (Fig. S6-2E-GH).

In Purkinje cells from mutant mice, we revealed increased expression of several genes annotated to the Human MSigDB mTOR pathway (98). These include the most upstream mTOR activator, insulin (*Ins*, 1.75 fold); S6-related kinase (*Rskr*, 1.75 fold); Nerve Growth Factor Receptor (*Ngfr*, 1.48 fold); *Mertk*, a tyrosine kinase (1.42 fold); interferon-induced transmembrane protein 1 (*Ifitm1*, 1.5 fold); and leukotriene C4 synthase (*Ltc4s*, 1.66 fold) (Fig. 6D). At the protein level, we observed increased phosphorylation of the insulin-like growth factor 1 receptor Igf1r at Tyr1135/Tyr1136 with no change in expression of the receptor, as measured by Luminex or label-free mass spectrometry of the cerebellum, respectively (Fig. 6E). Notably, IGF1-R stimulation has been reported to activate the p70 S6K1 pathway (99). Together, this shows that brain copper deficiency increases the expression of components of the mTOR-S6K pathway activity in Purkinje cells. There were no genotype-dependent changes in expression of components of the electron transport chain in either the Purkinje or granular layer ROIs (Fig. S6-3). We analyzed the spatial transcriptomic data by Gene Set Enrichment Analysis (GSEA) (100, 101) to unbiasedly identify

pathways disrupted by brain copper depletion in cerebellar cortex. We observed a global upregulation of the protein synthesis machinery, including 82 ribosomal subunits and protein synthesis elongation factors, in Purkinje cells but not in the granular layer (Fig. 6G, FGSEA estimated p value Benjamini-Hochberg-correction). Expression levels of cytoplasmic ribosome transcripts were similar in wild type Purkinje cells and granular layer cells (Fig. S6-2D). Our data support a model of mTOR-dependent upregulation of protein synthesis machinery in Purkinje neurons in presymptomatic copper-deficient mice.

Genetic modulation of mTOR pathway-dependent protein synthesis activity modifies copper deficiency phenotypes in **Drosophila**

We genetically tested whether increased activity of mTOR pathway-dependent protein synthesis was an adaptive or maladaptive mechanism in copper deficiency. We studied the effect of mTOR-S6K pathway gain- and loss-of-function on copper-deficiency phenotypes in *Drosophila.* In animals overexpressing ATP7, which induces copper depletion by metal efflux (ATP7-OE, Figs. 7 and S7; 102, 103-106), we also over-expressed and/or knocked down members of the mTOR pathway in either the epidermal epithelium (pnr-GAL4) or class IV sensory neurons (ppk-GAL4) (Fig. 7, Fig. S7, Table 3, 104, 105, 106). ATP7 overexpression in the dorsal midline caused depigmentation and bristle alterations in both males and female (Fig. S7; 104, 105, 106). Loss of function of either S6k, raptor, or Akt by RNAi intensified epidermal ATP7-OE copper deficiency phenotypes (Fig. S7), including the induction of additional dorsal thoracic caving (RAPTOR-IR and AKT-IR), necrotic tissue (RAPTOR-IR and AKT-IR), thoracic “dimples’ (S6K-IR in males, see arrowheads), and ultimately with increased lethality in response to Akt RNAi, with the few surviving animals showing caving and necrosis of the thoracic dorsal midline and/or scutellum (Fig. S7). We did not detect overt ATP7-OE phenotype modifications by mTOR pathway transgene overexpression (Akt or S6k) or the two RNAi lines for rictor (Fig. S7). These results suggest an adaptive role of mTOR-Raptor-S6K-dependent protein synthesis machinery in copper deficiency.

To test whether gain-of-function of mTOR-dependent protein synthesis machinery would rescue ATP7-OE phenotypes, we measured the complexity of class IV sensory neuron dendritic arbors and mitochondrial distribution in the third instar *Drosophila* larva. Dendrites in this cell type are a sensitive and quantitative reporter to measure cell-autonomous mechanisms in neuronal copper homeostasis (Fig. 7, 105, 106). Copper deficiency due to overexpression of ATP7 in these neurons decreased the complexity of the dendritic arbor (as quantified by average branch length and total dendritic length; Fig. 7A-B) and depleted mitochondria from dendrites (Fig. 7C), as previously reported (105, 106). The sole overexpression of Akt was not sufficient to modify ATP7-OE phenotypes (Fig. 7A-B). However, dendritic branch phenotypes were partially rescued by overexpression of either a constitutively active phosphomimetic mutant of S6k (S6k-STDETE, Fig. 7A-B, 107) or RNAi against Thor, the *Drosophila* orthologue of 4-EBP1, an inhibitor of protein synthesis downstream of mTOR necessary for mitochondrial biogenesis (Fig. 7A-B, 108, 109). 4E-BP1-dependent inhibition of protein synthesis is inhibited by mTOR-dependent phosphorylation; thus, 4-EBP1/Thor removal increases protein synthesis (110, 111). S6k-STDETE-OE or THOR-IR increased the length of dendritic branches, a phenotype specific to the distal dendritic branches without changes in total dendritic length (Fig. 7A-B). This increase in the average branch length resulted in an expansion of the dendritic field coverage by class IV neurons (Fig. 7A-B). Simultaneously, mitochondria distribution was rescued in ATP7-OE neurons expressing S6k-STDETE-OE, with the redistribution of mitochondria to dendrites (Fig. 7C, not quantified). These results demonstrate that activation of mTOR-dependent protein synthesis mechanisms partially revert copper-depletion neuronal phenotypes. We conclude that mTOR-dependent protein synthesis is an adaptive mechanism in neuronal copper deficiency.

Discussion

Here, we report that concomitant to changes in bioenergetics, copper-depleted cells undergo mTOR and PERK signaling modifications which converge on an adaptive response of increased protein synthesis in cellular and animal models of copper depletion.

We first established a cellular model of copper depletion by CRISPR editing to knockout CTR1 in SH-SY5Y cells (Fig. 1, Fig. S1). This cellular system recapitulates cardinal phenotypes of copper depletion such as compromises in copper-dependent enzymes including Complex IV of the respiratory chain, which drives cells into glycolysis with increased cellular lactate content (Fig. 1, Fig. S1). Importantly, respiration and metabolic phenotypes observed in CTR1 KO cells can be reverted by elesclomol (Fig. 1, Fig. S1), a drug that rescues neurodegeneration and organismal survival in animal models of copper depletion (31, 32).

We used the CTR1 KO cell model to unbiasedly identify cellular processes sensitive to copper depletion. The proteome, phosphoproteome, and transcriptome of CTR1-null cells identified the mTOR signaling pathway as one of the most enriched terms (Fig. 2, Fig. S2). Patterns of differential gene, protein, and phosphoresidues levels are indicative of increased mTORC1-S6K activation and downstream activation of protein synthesis through increased levels and phosphorylation of RPS6 (Fig. 2, Fig. 3). At least one of the mechanisms of this mTOR activation is through decreased expression of the mTOR inhibitor DEPTOR (Fig. 2, Fig. S2, Fig. 3). We suspect additional mechanisms, such as increased receptor tyrosine activity, also contribute to increased mTOR activation, as evidenced by increased insulin-dependent activity observed in Purkinje neurons of copper-deficient *Atp7a*$^{flx/Y}$ :: *Vil1*$^{Cre/+}$ mice (Fig. 6) and by the effect of Akt, raptor, and S6k RNAi enhancing *Drosophila* copper depletion epidermal phenotypes (Fig. S7). The effects mTOR activation in CTR1 KO cells span the RPTOR/Raptor (mTORC1) branch of the pathway, including increased expression of 14 transcripts annotated to mTOR and/or PI3K-Akt signaling (Fig. S2). Moreover, numerous proteins annotated to mTORC1-mediated signaling pathway exhibited increases in phosphorylation at residues responsive to mTOR and/or S6K activity, including mTOR, RPS6, EIF4G1, ACLY, UVRAG, and AKT1S1 (Fig. 2). In support of the idea that CTR1-null cells increase mTORC1 signaling and downstream S6K activation, these cells exhibit increased phosphorylation at mTOR S2448 and S6K1 T389 at baseline as well as under conditions of serum depletion or addition as compared to wild-type cells (Fig. 3). A notable finding is the discovery that concomitant to an upregulation of mTOR signaling and activation of S6K, we observed decreased protein expression and phosphorylation of EIF2AK3 (PERK) (Fig. 2, Fig. 3). As is expected by these changes in PERK and mTORC1 signaling, CTR1-null cells upregulate protein synthesis over wild-type cells (Fig. 5, Fig. S5). Similarly, *Atp7a*$^{flx/Y}$ :: *Vil1*$^{Cre/+}$ mice upregulate the protein synthesis machinery and expression of several genes in the mTOR pathway in Purkinje neurons at an early timepoint before the onset of cell death and mortality (Fig. 6, (31, 32, 90)).

Increased mTOR signaling and protein synthesis in response to copper depletion appears to be a cell-type specific response that is observed in human SH-SY5Y neuroblastoma cells (Fig. 2-5) and Purkinje cells but not granular layer cells in *Atp7a*$^{flx/Y}$ :: *Vil1*$^{Cre/+}$ mice (Fig. 6), suggesting that Purkinje cells are especially sensitive to copper depletion. CTR1 KO mouse embryonic fibroblasts were previously reported to show no changes in phosphorylation of either mTOR- or PI3K-Akt-specific substrates (51). In Menkes disease, Purkinje cells experience rapid and specific pathology relative to other cell types and regions of the brain, including enlarged and distended mitochondria, increased dendritic arborization, and cell death, which have been reported in both humans (10, 11, 112-115) and various mouse models (30, 31, 116, 117). Importantly, some of these phenotypes are recapitulated by cell-autonomous hyperactivation of mTOR; however, in contrast with Menkes disease, mTOR activation in copper-sufficient Purkinje cells *increases* the size and respiratory activity of their mitochondria (118). Dramatic differences in the mitochondrial proteome between Purkinje cells and other cell types in the cerebellum have been reported (119). Thus, Purkinje neurons and their mitochondria may be uniquely susceptible to copper depletion due to cell-type specific mitochondrial properties and/or abundance, as well

as their dependency on mTOR signaling (Fig. 6S2). This is consistent with the enrichment of nuclear-encoded mitochondrial transcripts and mitochondrial activity in GABAergic neurons, particularly those expressing parvalbumin (120, 121).

Previous reports have connected mitochondrial dysfunction with mTOR or PERK signaling. Mouse models of Leigh syndrome (caused by a deficiency in the Complex I subunit Ndufs4) and mitochondrial myopathy exhibit increased mTORC1 activity (122, 123), and downregulation of the mitochondrial respiratory complexes I, III, or IV stimulates TOR activity in the *Drosophila* wing disc (124). Multiple diseases with impairments in mitochondrial respiration have been reported to benefit from mTOR inhibition, which is proposed to help alleviate metabolic stress. For example, rapamycin promotes survival and ameliorates pathology in a mouse model of Leigh syndrome (122), and death due to energy stress in cells that are Coenzyme-Q-deficient is rescued by several mTORC1/2 inhibitors as well as protein synthesis inhibition by cycloheximide (125). These studies stand in contrast with our results. Our pharmacogenetic epistasis studies in CTR1 KO cells demonstrate that mTOR activation and increased protein synthesis is adaptive (Fig. 4, S4-2) and that these cells are more sensitive to protein synthesis inhibition (Fig. 5, S5). Additionally, stimulating protein synthesis in copper depleted *Drosophila* by either S6k overexpression or Thor RNAi partially rescues dendritic branching and mitochondrial phenotypes in class IV sensory neurons (Fig. 7), while downregulation of S6k, Akt, or raptor increases the severity of copper deficiency phenotypes in the epidermis (Fig. S7). This suggests that mTOR-Raptor-S6K-dependent protein synthesis is adaptive in copper-deficient neurons and is necessary and sufficient to partially revert the effects of copper depletion in *Drosophila* (Fig. 7 and S7). Based on these data and the fact that two distinct pathways favoring increased protein synthesis are activated in response to copper deficiency, we conclude that increased protein synthesis downstream of increased mTORC1 activity and/or decreased PERK represents a pro-survival response to copper depletion.

It is perhaps counterintuitive for cells to upregulate a nutrient sensing pathway like mTOR when deficient in an important micronutrient and enzyme cofactor like copper, which might be expected to decrease mTOR activity (126). It is particularly surprising given that metabolic and mitochondrial diseases benefit from mTOR inhibition (see above). We speculate this could be a way to rectify an imbalance in proteostasis and metabolism due to copper depletion. Impaired autophagic flux has been reported in hyperglycolytic neurons (25), and as copper is required for ULK1 activity and autophagy (51), copper deficiency may inhibit autophagy, limiting the availability of a recycled pool of amino acids for *de novo* protein synthesis or as fuel for mitochondrial respiration. Thus, mTOR activation could lead to an increase in the efficiency of protein synthesis and cell cycle progression by increasing amino acid uptake from the media, as suggested by our findings of increased mRNA for the amino acid transporters SLC7A5 and SLC3A2 in CTR1 KO cells and wild-type cells treated with the copper chelator BCS (Fig. S2), and/or by increased translation efficiency of particular RNA splice variants (69, 127). Increased levels of amino acid transporters at the cell surface may relate to the perplexing result that CTR1-null cells increase normalized respiration more than wild-type cells after the addition of fresh media (Fig. 5). While CTR1 KO cells exhibit increased glycolysis and lactate levels and decreased basal and ATP-dependent respiration under baseline condition (Figs. 1, S1), mTOR activation and the upregulation of COX17 and other chaperones for Complex IV may prime these cells to utilize nutrients such that fresh media enables increased respiration even under low serum conditions (Fig. 5C2, compare the blue groups) or when treated with emetine to inhibit protein synthesis (Fig. 5D2).

To our knowledge, our cellular and animal models of copper depletion provide the first evidence that 1) genetic defects that impair cellular copper homeostasis simultaneously modify two signaling pathways regulating protein synthesis and 2) in which the upregulation of protein synthesis is adaptive for cell-autonomous disease phenotypes. We propose that neuronal cell

pathology occurs when resilience mechanisms engaged in response to copper deficiency are outpaced by the increasing bioenergetic demands of the cell during neurodevelopment.

Materials and Methods

Cell lines, gene editing, and culture conditions

Human neuroblastoma SH-SY5Y cells (ATCC, CRL-2266; RRID:CVCL_0019) were grown in DMEM media (Corning, 10-013) containing 10% FBS (VWR, 97068-085) at 37°C in 10% CO_2, unless otherwise indicated. SH-SY5Y cells deficient in SLC31A1 were generated by genome editing using gRNA and Cas9 preassembled complexes by Synthego with a knock-out efficiency of 97%. The gRNAs used were UUGGUGAUCAAUACAGCUGG, which targeted transcript ENST00000374212.5 exon 3. Wild-type and mutant cells were cloned by limited dilution and mutagenesis was confirmed by Sanger sequencing with the primer: 5'GGTGGGGGCCTAGTAGAATA. All controls represent either a single wild-type clone or a combination of two wild-type clones. All experiments used two separate mutant clones of cells (KO3 and KO20, see Fig. S1A,B) were used to exclude clonal or off-target effects unless otherwise indicated.

Mouse husbandry

Animal husbandry and euthanasia was carried out as approved by the Emory University Institutional Animal Care and Use Committees. Genotyping was performed by Transnetyx using real-time PCR with the Vil1-Cre-1 Tg, Atp7a-2 WT, and Atp7a-2 FL probes.

Antibodies

The antibodies used are listed at the indicated concentrations for western blots and immunofluorescence in Table 1.

Drugs

The drugs used are listed in Table 2. All drugs were used at the indicated concentrations or concentration ranges as described in Table 2 and their corresponding figure legends.

Immunoblotting and puromycin pulse

Cells were grown in 12 or 24 well plates up to required confluency. Treatments are described in each figure. For puromycin pulse experiments, puromycin was added to the media 30 minutes before lysis to a final concentration of 1 mg/mL. The plates were placed on ice, and the cells were washed with cold phosphate-buffered saline (PBS) (Corning, 21-040-CV). Lysis buffer containing 150 mM NaCl, 10 mM HEPES, 1 mM ethylene glycol-bis(β-aminoethylether)-*N*,*N*,*N*′,*N*′-tetraacetic acid (EGTA), and 0.1 mM MgCl2, pH 7.4 (Buffer A), with 0.5% Triton X-100 (Sigma, T9284) and Complete anti-protease (Roche, 11245200) was added to each plate. For samples of interest for phosphorylated proteins, PhosSTOP phosphatase inhibitor (Roche, 04906837001) was also added to the lysis buffer. Cells were then scraped and placed in Eppendorf tubes on ice for 20 min and centrifuged at 16,100 × *g* for 10 min. The insoluble pellet was discarded, and the clarified supernatant was recovered. The Bradford Assay (Bio-Rad, 5000006) was used to determine protein concentration, and all lysates were flash frozen on dry ice and stored at -80C.

Cell lysates were reduced and denatured with Laemmli buffer (SDS and 2-mercaptoethanol) and heated for 5 min at 75C. Equivalent amounts of samples were loaded onto 4-20% Criterion gels (Bio-Rad, 5671094) for SDS-PAGE in running buffer (25 mM TRIS, 130 mM glycine, and 0.1% SDS) and transferred using the semidry transfer method with transfer buffer (48 mM TRIS, 39 mM glycine, 0.037% SDS, 20% methanol) to polyvinylidene difluoride (PVDF) membranes (Millipore, IPFL00010) unless otherwise specified in the figure legend that a nitrocellulose membrane was used (Sigma, 10600009). The membranes were incubated in TRIS-Buffered Saline (TBS: 1.36 M NaCl, 26.8 mM KCl, 247 mM TRIS) containing 5% nonfat milk and 0.05% Triton X-100 (TBST; blocking solution) for 30 min at room temperature (RT). The membrane was then rinsed thoroughly and incubated overnight with optimally diluted primary antibody in a buffer containing PBS with 3% bovine serum albumin (BSA) and 0.2% sodium azide. The next day, membranes were rinsed in TBST and treated with horseradish peroxidase-conjugated secondary antibodies against mouse or rabbit (see Table 1) diluted 1:5000 in the blocking solution for at least 30 min at RT. The membranes were washed in TBST at least three times and probed with Western Lightning Plus ECL reagent (PerkinElmer, NEL105001EA) and exposed to GE Healthcare Hyperfilm ECL (28906839). Additional staining was repeated as described above follows stripping of blots (200 mM glycine, 13.8 mM SDS, pH 2.5).

Mitochondrial isolation and blue native gel electrophoresis

Starting material was two 150 mm dishes with cells at 80-90% confluency for each condition. The cells were released with trypsin and the pellet washed with PBS. Crude mitochondria were enriched according to (128). Briefly, cells were homogenized in isolation buffer (225 mM mannitol, 75 mM sucrose, 0.1 mM EGTA, and 30 mM Tris-HCl, pH 7.4) with 20 strokes in a Potter-Elvehjem homogenizer at 6000 rpm, 4°C. Unbroken cells and nuclei were collected by centrifugation at 600 × g for 5 min and mitochondria recovered from this supernatant by centrifugation at 7000 × g for 10 min. After one wash of this pellet, membranes were solubilized in 1.5 M aminocaproic acid, 50 mM Bis-Tris, pH 7.0, buffer with antiproteases and 4 g/g (detergent/protein) digitonin or DDM (n-dodecyl β-D-maltoside) to preserve or dissolve supercomplexes, respectively (129, 130). Proteins were separated by blue native electrophoresis in 3-12% gradient gels (Novex, BN2011BX10; 130, 131) using 10 mg/ml ferritin (404 and 880 kDa, Sigma F4503) and BSA (66 and 132 kDa) as molecular weight standards.

Cell survival and Synergy analysis

For all cell survival assays with a single drug, cells were counted using an automated Bio-Rad cell counter (Bio-Rad, TC20, 1450102) and plated in 96 well plates at 5,000-10,000 cells/well and allowed to sit overnight before drugs were added. Cells were treated with the drug concentrations indicated in each figure and summarized in Table 2 for 72 hours with the exception of emetine, for which double the number of cells were plated and cells were treated for 24 hours. Fresh media with 10% Alamar blue (Resazurin, R&D Systems #AR002) was added to each well and after 2 hours in the incubator absorbance was measured using a microplate reader (BioTek, Synergy HT; excitation at 530–570 nm and emission maximum at 580–590 nm) using a BioTek Synergy HT microplate reader with Gen5 software 3.11. For each experiment, percent survival was calculated by subtracting the background value of an empty well with only Alamar blue and normalizing to the untreated condition for each genotype. Individual data points represent the average survival of duplicate or triplicate treatments for each concentration.

For Synergy survival assays with two drugs, cells were plated in 96 well plates, treated with drugs, and incubated with Alamar blue as described above. Concentrations used are depicted in the corresponding figures and summarized in Table 2. For each experiment, percent survival was calculated by normalizing to the untreated condition for each genotype. For experiments with fetal bovine serum, values were normalized to the 10% serum condition, equivalent to the normal growth media. Individual data points represent the average survival of

single replicates for each concentration. Synergy calculations were performed using the ZIP score with the SynergyFinder engine (https://synergyfinder.org/, 82, 132). For Torin 2-elesclomol experiments, the weighted ZIP score was used, a calculation which identifies synergy at lower drug doses with less toxicity by weighting the synergy distribution at each dose level using the proportion of responses from each drug in isolation (81).

Seahorse metabolic oximetry

Extracellular flux analysis of the Mito Stress Test was performed on the Seahorse XFe96 Analyzer (Seahorse Bioscience) following manufacturer recommendations. SH-SY5Y cells were seeded at a density of 30,000 cells/well on Seahorse XF96 V3-PS Microplates (Agilent Technologies, 101085-004) after being trypsinized and counted (Bio-Rad TC20 automated Cell Counter) the day before the experiment. When appropriate, cells were treated with drugs in 10 cm plates before seeding in Seahorse XF96 microplates and treated overnight (see indicated times and concentrations in figure legends). XFe96 extracellular flux assay kit probes (Agilent Technologies, 102416-100) incubated with the included manufacturer calibration solution overnight at 37°C without CO_2 injection. The following day, wells were washed twice in Seahorse Mito Stress Test Media. The Mito Stress Test Media consisted of Seahorse XF base media (Agilent Technologies, 102353-100) with the addition of 2 mM L-glutamine (HyClone, SH30034.01), 1 mM sodium pyruvate (Sigma, S8636), and 10 mM D-glucose (Sigma, G8769). After the washes, cells were incubated at 37°C without CO_2 injection for 1 hour prior to the stress test. During this time, flux plate probes were loaded and calibrated. After calibration, the flux plate containing calibrant solution was exchanged for the Seahorse cell culture plate and equilibrated. Seahorse injection ports were filled with 10-fold concentrated solution of oligomycin A, FCCP, and rotenone mixed with antimycin A (see Table 2 for final testing conditions and catalog numbers). All Seahorse drugs were dissolved in DMSO and diluted in Seahorse Mito Stress Test Media for the Seahorse protocol. The flux analyzer protocol included three basal read cycles and three reads following injection of oligomycin A, FCCP, and rotenone plus antimycin A. Each read cycle included a 3-minute mix cycle followed by a 3-minute read cycle where oxygen consumption rate (OCR) and extracellular acidification rate (ECAR) were determined over time. In all experiments, OCR and ECAR readings in each well were normalized by protein concentration in the well. Cells were washed twice with phosphate buffered saline (Corning 21-040-CV) supplemented with 1 mM $MgCl_2$ and 100 µM $CaCl_2$ and lysed in Buffer A. Protein concentration was measured using the Pierce BCA Protein Assay Kit (Thermo Fisher Scientific, 23227) according to manufacturer protocol. The BCA assay absorbance was read by a BioTek Synergy HT microplate reader using Gen5 software. For data analysis of OCR and ECAR, the Seahorse Wave Software version 2.2.0.276 was used. Individual data points represent the average values of a minimum of three replicates. Non-mitochondrial respiration was determined as the lowest OCR following injection of rotenone plus antimycin A. Basal respiration was calculated from the OCR just before oligomycin injection minus the non-mitochondrial respiration. Non-mitochondrial respiration was determined as the lowest OCR following injection of rotenone plus antimycin A. ATP-dependent respiration was calculated as the difference in OCR just before oligomycin injection to the minimum OCR following oligomycin injection but before FCCP injection. Maximal respiration was calculated as the maximum OCR of the three readings following FCCP injection minus non-mitochondrial respiration.

Extracellular flux analysis of the Glycolysis Stress Test was performed as above with the following changes. The Glycolysis Stress Test Media contained only 2 mM L-glutamine. Seahorse injection ports were filled with 10-fold concentrated solution of D-glucose, oligomycin, and 2-Deoxy-D-glucose (2-DG) (see Table 2 for final testing conditions and catalog numbers). All drugs were diluted in Seahorse Glycolysis Stress Test Media for the Seahorse protocol. Glycolysis is calculated as the difference in ECAR between the maximum rate measurements before oligomycin injection and the last rate measurement before glucose injection. Glycolytic capacity was calculated as the difference in ECAE between the maximum rate measurement after

oligomycin injection and the last rate measurement before glucose injection. Glycolytic reserve was calculated as the glycolytic capacity minus glycolysis. Non-glycolytic acidification was defined as the last rate measurement prior to glucose injection.

Resipher

Poly-L-lysine coated Nunc 96 well (Thermo, 269787) or Falcon 96 well (Falcon, 353072) plates were seeded with 40,000 cells per well with 200 µL culture media (DMEM/10% FBS media). The following day, 150 µL of culture media was replaced with fresh, prewarmed, DMEM/10% FBS media. The Resipher sensing probe lid (Nunc Plates, NS32-N; Falcon Plates, NS32-101A) and Resipher system (Lucid Scientific, Atlanta, GA) were placed on one of the replicate plates and incubated in a humidified, 37C, 5% CO2 incubator while data was collected. For serum switch assays, at 48 hours after starting Resipher surveillance, 150 µL of warmed, un-supplemented DMEM media was replaced 3 times in 200 µL total volume to serially dilute assay to DMEM/0.16% FBS. For emetine assays, at approximately 48 hours after beginning Resipher surveillance, 150 µL of media was replaced with warmed DMEM/10% FBS media containing DMSO vehicle (VWR, WN182) or emetine (Sigma, E2375) to bring the final concentration in the wells to 3.2e-4% DMSO and 60 nM, 120 nM, or 240 nM emetine. After approximately 24 hours of DMEM/0.16%FBS or DMEM/10% FBS with vehicle/emetine treatment, rotenone (Sigma, R8875) and antimycin A (Sigma, A8674) were diluted to 10x in un-supplemented media and added to bring the well concentration to 1 mM rotenone and 1 mM Antimycin A. After about 24 hours of rotenone/antimycin treatment, the Resipher system assay was stopped. Cell counts were performed in parallel plates by measuring protein content at 24h, 48h (at the addition of emetine/DMSO/vehicle media), and 72h (at the addition of rotenone/antimycin A) and on the final Resipher plate after respiration was stably down following the addition of rotenone and antimycin A. To determine protein concentrations, wells were washed three times with phosphate buffered saline (Corning 21-040-CV) supplemented with 1 mM MgCl2 and 100 µM CaCl2, and cells were lysed in Buffer A with Complete antiprotease. Protein concentration was measured using the Pierce BCA Protein Assay Kit (Thermo Fisher Scientific, 23227) according to manufacturer protocol. Experiments were repeated in quadruplicate. Doubling time (T_d) was estimated using the equation $N(t)=N(0)2^{t/Td}$ where N(0) is the protein at either 24 or 48h and N(t) is the protein 24h later. Accumulated cell counts were estimated by determining areas under the curve using Prism Version 10.2.2 (341).

Total RNA extraction and NanoString mRNA Quantification

Cells were grown on 10 cm plates, and total RNA was extracted using the TRIzol reagent (Invitrogen, 15596026). When applicable, cells were treated with 200 µM BCS for 3 days. For preparation of samples, all cells were washed twice in ice-cold PBS containing 0.1 mM CaCl2 and 1.0 mM MgCl2. 1 ml of TRIzol (Invitrogen, 15596026) was added to the samples and the TRIzol mixture was flash frozen and stored at -80C for a few weeks until RNA Extraction and NanoString processing was completed by the Emory Integrated Genomics Core. The Core assessed RNA quality before proceeding with the NanoString protocol. The NanoString Neuropathology gene panel kit (XT-CSO-HNROP1-12) or Metabolic Pathways Panel (XT-CSO-HMP1-12) was used for mRNA quantification. mRNA counts were normalized to either the housekeeping genes AARS or TBP, respectively, using NanoString nSolver software. Normalized data were further processed and visualized by Qlucore.

ICP mass spectrometry

Procedures were performed as described previously (43). Briefly, cells were plated on 10 or 15 cm dishes. After reaching desired confluency, cells were treated with 1 nM elesclomol for 24 hours. On the day of sample collection, the plates were washed three times with PBS, detached with trypsin, and neutralized with media and pelleted at 800 × g for 5 min at 4C. The

cell pellet was resuspended with ice-cold PBS, aliquoted into 3-5 tubes, centrifuged at 16,100 × g for 10 min. The supernatant was aspirated, and the residual pellet was immediately frozen on dry ice and stored at -80C. Mitochondria were isolated as described above. Tissue samples were collected following euthanasia, weighed, and immediately flash frozen on dry ice. Cell or mitochondrial pellets were digested by adding 50 µL of 70% trace metal basis grade nitric acid (Millipore Sigma, 225711) followed by heating at 95C for 10 min. Tissue was digested by adding 70% nitric acid (50-75% w/v, i.e. 50 mg of tissue was digested in 100 µL of acid) and heated at 95C for 20 min, followed by the addition of an equal volume of 32% trace metal basis grade hydrogen peroxide (Millipore Sigma, 95321) and heated at 65C for 15 minutes. After cooling, 20 µL of each sample was diluted to 800 µL to a final concentration of 2% nitric acid using either 2% nitric acid or 2% nitric acid with 0.5% hydrochloric acid (VWR, RC3720-16) (vol/vol). Metal levels were quantified using a triple quad ICP-MS instrument (Thermo Fisher, iCAP-TQ) operating in oxygen mode under standard conditions (RF power 1550 W, sample depth 5.0 mm, nebulizer flow 1.12L/min, spray chamber 3C, extraction lens 1,2 -195, –-15 V). Oxygen was used as a reaction gas (0.3 mL/min) to remove polyatomic interferences or mass shift target elements (analytes measured; 32S.16O, 63Cu, 66Zn). External calibration curves were generated using a multielemental standard (ICP-MSCAL2-1, AccuStandard, USA) and ranged from 0.5 to 1000 µg/L for each element. Scandium (10 µg/L) was used as internal standards and diluted into the sample in-line. Samples were introduced into the ICP-MS using the 2DX PrepFAST M5 autosampler (Elemental Scientific) equipped with a 250 µL loop and using the 0.25 mL precision method provided by the manufacturer. Serumnorm (Sero, Norway) was used as a standard reference material, and values for elements of interest were within 20% of the accepted value. Quantitative data analysis was conducted with Qtegra software, and values were exported to Excel for further statistical analysis.

Preparation of brain tissue for proteomics, immunoblots, or Luminex analysis

Brain samples were collected after euthanasia and immediately flash frozen in liquid nitrogen and stored at -80C. Brains were lysed in 8M urea in 100 µM potassium phosphate buffer (pH 8.0; 47.6 mL 1M K_2HPO_4 + 4.8 mL 1M KH_2PO_4, bring to 525 mL total volume) with Complete anti-protease and PhosSTOP phosphatase inhibitor and homogenized by sonication (Fisher Scientific, Sonic Dismembrator Model 100). After incubation on ice for 30 minutes, samples were spun at 7000 × g for 10 minutes at 4C, and the supernatant was transferred to a new tube. Protein concentration was measured in triplicate using the Pierce BCA Protein Assay Kit (Thermo Fisher Scientific, 23227) according to manufacturer protocol. Samples were stored at -80C until use.

TMT mass spectrometry for proteomics

Cells were grown in standard media as described above (Fig. 2C, TMT1; DMEM (Corning, 10-013), 10% FBS, 25 mM D-glucose, 4 mM L-glutamine, 1 mM sodium pyruvate) or media with dialyzed FBS supplemented with D-glucose, sodium pyruvate, and L-glutamine (Fig. 2C, TMT2; DMEM (Thermo Fisher, A14430-01), 10% dialyzed FBS (Thermo Fisher, 26400-044), 10 mM D-glucose, 2 mM L-glutamine, 1 mM pyruvate). There was no difference in total cellular copper as measured by ICP-MS (not shown; manuscript in preparation containing the complete TMT2 dataset). Cells were detached with PBS-EDTA (ethylenediaminetetraacetic acid, 10 mM) and pelleted as described above for ICP-MS. The supernatant was aspirated, and the pellet was immediately frozen on dry ice and stored at -80C.

TMT labeling was performed according to the manufacturer's protocol and as described previously (133, 134). Briefly, samples were lysed in urea buffer (8 M urea, 100 mM NaH_2PO_4, pH 8.5; 1X HALT protease and phosphatase inhibitor cocktail, Pierce) and underwent probe sonication. Protein concentration was measured by BCA assay, and aliquots were prepared with 100 µg lysate in the same total volume of lysis buffer. Aliquots were diluted with 50 mM HEPES

(pH 8.5) and sequentially treated with 1 mM DTT (1,4-dithiothreitol) and 5 mM IAA (iodoacetamide) for alkylation at room temperature, followed by overnight digestion with lysyl endopeptidase (Wako) at a 1:50 (w/w) enzyme to protein ratio, dilution to a urea concentration of 1 M with 50 mM triethylammonium bicarbonate (TEAB), and overnight digestion with trypsin (Promega) at a 1:50 (w/w) enzyme to protein ratio. Peptides were desalted with a Sep-Pak C18 column (Waters) and aliquots of each sample (equivalent to 20 µg protein per sample) were combined to obtain a global internal standard (GIS) for TMT labeling. All 20 samples were then dried under vacuum (16 individual and 4 GIS), resuspended in 100 mm TEAB buffer followed by the addition of anhydrous acetonitrile, and solutions were transferred to their respective channel tubes. After 1 hr, the reaction was quenched with 5% hydroxylamine and all samples were combined and dried. Samples were resuspended in 90% acetonitrile and 0.01% acetic acid and loaded onto an offline electrostatic repulsion–hydrophilic interaction chromatography fractionation HPLC system. 96 fractions were collected, combined into 24 fractions, dried down, and resuspended in peptide loading buffer (0.1% formic acid, 0.03% trifluoroacetic acid, 1% acetonitrile). Peptide mixtures (2 µL) were separated on a self-packed C18 fused silica column by an Easy-nLC 1200 and monitored on a Fusion Lumos mass spectrometer (Thermo Fisher Scientific). MS/MS spectra were searched against the Uniprot human database (downloaded on 04/2015) with Proteome Discoverer 2.1.1.21 (Thermo Fisher Scientific). Variable and static modifications included methionine oxidation, asparagine, glutamine deamidation, protein N-terminal acetylation, cysteine carbamidomethyl, peptide N-terminus TMT, and lysine TMT. Percolator was used to filter MS/MS spectra matches false discovery rate of <1%. Abundance calculations used only razor and unique peptides, and the ratios of sample over the GIS of normalized channel abundances were used for comparison across all samples. Data files will be uploaded to ProteomeExchange.

Metabolite quantification by LC mass spectrometry

Cells were seeded in duplicate 6 wells per replicate at 100,000 or 190,000 cells per well for wild-type and CTR1 KO cells, respectively, and treated with 1 nM elesclomol for 2 days. Media was replaced with pyruvate-free media (Thermo Fisher 11966-025, supplemented with 25 mM glucose) with dialyzed FBS (Thermo Fisher 26400044) and 1 nM elesclomol and 5 µM $CuCl_2$ for 24 hours. (Media prepared with dialyzed FBS must be supplemented with copper as dialysis removes copper from the serum.) After a total of 72h elesclomol treatment, cells were washed with ice-cold PBS supplemented with 1 mM $MgCl_2$ and 100 µM $CaCl_2$ and extracted with 400 µL of lysis buffer (0.1M formic acid at 4:4:2 dilution (MeOH: ACN: Water) containing 25 µM $^{13}C_3$ alanine as an internal standard. After 2 min on ice, 35 µL of 15% NH_4HCO_3 was added, mixed well by gently swirling the plate, and incubated for another 20 min on ice. Cell lysates were then transferred into pre-chilled 1.5 ml centrifuge tubes, vortexed briefly, and spun at 21,300xg for 30 min at 4°C. 360 µL of supernatant was then transferred into pre-chilled 1.5 ml centrifuge tubes and dried down using a Savant Speedvac Plus vacuum concentrator. Samples were resuspended in 120 µL of 60:40 (ACN: Water), sonicated for 5 minutes at 4°C, and centrifuged at 21,300xg for 20 min at 4°C. 100 µL of supernatant was transferred into a pre-chilled LC-MS vial. 5 µL of this sample was injected into a HILIC-Z column (Agilent Technologies) on an Agilent 6546 QTOF mass spectrometer coupled with an Agilent 1290 Infinity II UHPLC system (Agilent Technologies). The column temperature was maintained at 15 °C and the autosampler was at 4 °C. Mobile phase A: 20 mM Ammonium Acetate, pH = 9.3 with 5 µM Medronic acid, and mobile phase B: acetonitrile. The gradient run at a flow rate of 0.4 ml/min was: 0min: 90% B, 1min 90% B, 8 min: 78% B, 12 min: 60% B, 15 min: 10% B, 18 min: 10 %B, 19-23 min: 90% B. The MS data were collected in the negative mode within an m/z = 20-1100 at 1 spectrum/sec, Gas temperature: 225 ºC, Drying Gas: 9 l/min, Nebulizer: 10 psi, Sheath gas temp: 375 ºC, Sheath Gas flow: 12 l/min, VCap: 3000V, Nozzle voltage 500 V, Fragmentor: 100V, and Skimmer: 45V. Data were analyzed using Masshunter Qualitative Analysis 10 and Masshunter Quantitative Analysis 11 (Agilent Technologies). Metabolite levels from different treatments were normalized to cell numbers.

Insulin receptor phosphorylation quantification

The cerebellum was isolated from mice at postnatal day 10 and flash frozen in liquid nitrogen and stored at -80C. Tissue was dissolved in 300 µL 8M urea in 100 mM PO_4 containing protease and phosphatase inhibitors, sonicated 5-10 times in 1 second bursts, and incubated on ice for 30 minutes with periodic vortexing. Samples were spun at 13,500 RCF for 10 min at 4C and the supernatant was transferred to a new tube. Protein concentration was measured in triplicate by BCA as described above. Mouse brain lysates were stored at -80°C, then thawed on ice and normalized to 1µg of total protein in Milliplex Assay buffer prior to the start of the assay protocol. We measured Tyr1135/Tyr1136 phosphosites in IGF1R with the Milliplex® MAP kit (48-611MAG) read out on a MAGPIX Luminex instrument (Luminex, Austin, TX, USA).

Digital spatial profiling of mouse brain tissue

Formalin-fixed paraffin-embedded mouse brain tissue was profiled using GeoMx® DSP (95). Brains were isolated at P10 after euthanasia and immediately fixed overnight at room temperature in 10% neutral buffered formalin (Thermo Fisher 28906, diluted to 10% NBF with 0.9% sterile saline solution) at a ratio of 20:1 fixative to sample. Thin (5 µm) sagittal tissue sections were prepared on positively charged slides by the Emory University Cancer Tissue and Pathology shared resource according to manufacturer's recommendations for Semi-Automated RNA Slide Preparation Protocol (FFPE) (manual no. MAN-10151-04). Sections were air-dried at room temperature overnight and shipped to NanoString at room temperature.

Following an overnight bake at 65°C, slides underwent deparaffinization, rehydration, heat-induced epitope retrieval (for 20 minutes at 100°C with Bond Epitope Retrieval 2 Solution), and enzymatic digestion (0.1 µg/mL proteinase K for 15 minutes at 37°C). Tissues were then incubated with 10% neutral buffered formalin for 5 minutes and 5 minutes with NBF Stop buffer. All steps following overnight baking were carried out on a Leica BOND-RX. Slides were then removed from the Leica BOND-RX and *in situ* hybridization with GeoMx® Mouse Whole Transcriptome Atlas (mWTA) probes was carried out overnight in a humidified hybridization chamber kept at 37°C. Following rounds of stringent washing with a 1:1 volumetric mixture of 4X SSC and 100% formamide to remove off-target probes, the tissue was blocked with Buffer W blocking solution (NanoString Technologies) then incubated with a mouse anti-GFAP antibody (see Table 2) and a stain for the nuclear marker Syto83.

Tissue morphology was visualized using fluorescent antibodies and Syto83 on the GeoMx® DSP instrument. Regions of interest (ROIs) were selected from the cerebellum of the samples using the polygon tool. Either a GFAP+ or GFAP- mask was generated within each ROI using the fluorescence signal associated with the GFAP antibody, and UV light was utilized to release and collect oligonucleotides from each ROI. Areas of UV light irradiation within an ROI are referred to as areas of illumination (AOI). During PCR, Illumina i5 and i7 dual-indexing primers were added to each photocleaved oligonucleotide allowing for unique indexing of each AOI. Library concentration was measured using a Qubit fluorometer (Thermo Fisher Scientific), and quality was assessed using a Bioanalyzer (Agilent). The Illumina Novaseq 6000 was used for sequencing, and the resulting FASTQ files were then processed by the NanoString DND pipeline to generate count data for each target probe in every AOI.

Quality control and preprocessing of GeoMx transcript data

The GeoMx DSP Analysis Suite was utilized for conducting both quality control (QC) and data exploration. First, each AOI was QC checked to ensure contamination was avoided during PCR and library preparation and that sequencing was sufficient. All AOIs passed QC so none were removed from downstream analysis. Next, any global outliers in the target list were

identified and removed from the panel. Finally, the dataset was normalized using third quantile (Q3) normalization. The QC checked, Q3 normalized dataset was used for downstream analysis.

Drosophila *husbandry and genotypes*

All fly strains were reared at 25C on standard molasses media (Genessee Scientific) on a 12hr:12hr light:dark cycle. All fly strains were isogenized and bred into the same genetic background (Table 3). For epidermis experiments (Fig. S7), flies were aged 4-7 days and imaged using an Olympus SZ-61 stereomicroscope and an Olympus DP23 color camera. Images were then stacked using Zyrene stacker. Dendritic characterization experiments were performed as described previously (105). Briefly, virgin females from mCD8-GFP were outcrossed to male flies from individual transgenic fly lines (AKT-OE, S6K-STDETE-OE, THOR-IR, and THOR-IR2) to first determine their effects on dendritic morphology. Of the two Thor RNAi lines tested, THOR-IR was the most phenotypic and all further experiments were performed using this line. The effect of ATP7-OE was determined using the ATP7-OE;mCD8-GFP transgenic fly line. Rescue analyses were performed by outcrossing ATP7-OE;mCD8-GFP virgin female flies to male flies from the fly lines previously mentioned. For both mCD8-GFP and ATP7-OE;mCD8-GFP, CD4-tdGFP was used as control. For super-resolution imaging, UAS-mito-HA-GFP;GAL4ppk1.9,UAS-mCD8::RFP virgin female flies were outcrossed to male flies from UAS-ATP7, UAS-ATP7;UAS-S6k.STDETE, or UAS-CD4-tdTOM (control).

Drosophila dendritic imaging and analysis

Live confocal imaging was done as previously described (105). Neurons were imaged from wandering third-instar larvae on a Zeiss LSM780 microscope. Individual animals were placed on a microscopic slide and anesthetized by immersion in 1:5 (v/v) diethyl ether to halocarbon oil solution and covered with 22 x 50 mm coverslip. Images were acquired as z-stacks using a 20x dry objective (NA 0.8) and step size 2µm. Maximum intensity projections of the images were acquired, and the images were exported as .jpeg files using the Zen Blue software. Images were then stitched using Adobe Photoshop and manually curated using the Flyboys software to remove background noise (136). The images were skeletonized and processed on ImageJ (137, 138) using a custom macro (https://github.com/CoxLabGSU/Drosophila_Sensory_Neuron_Quantification) to get quantitative metrics such as total dendritic length, branches, maximum intersection (Sholl), radius of maximum intersection (Sholl), and dendritic field coverage (convex hull). For proximal-distal analysis, a circular region of 400 pixels diameter from the soma was selected and considered as proximal to the soma. The region beyond 400 pixels was considered as distal. These regions were then analyzed separately. Average branch length was calculated by dividing the total dendritic length by the branches. The data obtained were then compiled using R6 (139) and exported to Excel (Microsoft).

Super-resolution imaging was performed on a Zeiss LSM980 Airyscan 2 confocal microscope on live animals. Animals were prepared as described above, and images were acquired as z-stacks using a 63x oil objective on Airyscan mode (SuperResolution:9.0 (3d, Auto)). Maximum intensity projections of the images were created using the Zen Blue software and exported as .TIFF files.

Data availability

The mass spectrometry proteomics data will be deposited to the ProteomeXchange Consortium via the PRIDE (140) partner repository.

Bioinformatic analyses and statistical analyses

Transcriptomics and proteomics data were processed with Qlucore Omics Explorer Version 3.6(33). Data were normalized to a variance of 1 and an average of 0 for statistical analysis and thresholding. Permutation statistical analyses were performed with the engine https://www.estimationstats.com/#/ with a two-sided permutation t-test using 5000 reshuffles (141). ANOVA and paired analyses were conducted with Prism Version 10.2.2 (341). Gene ontology studies were performed with Metascape and ENRICHR (142).

Acknowledgments

This work was supported by NIH grants 1RF1AG060285 to VF, 1F31NS127419 to ARL, 4K00NS108539 to KSS, T34GM131939 to TT, R01NS086082 to DNC, 1R01NS133344-01A1 to AP, and R01ES034796 to EW and a Burroughs Wellcome 2021 Postdoctoral Grant to KSS. ARL is supported by an ARCS Foundation Award, Robert W. Woodruff Fellowship, John B. Lyon Memorial Scholarship Award, and NanoString Young Investigator Brain Tank award. This study was supported in part by the Emory Integrated Genomics and Proteomics Cores, which are subsidized by the Emory University School of Medicine, and the Cancer Tissue and Pathology shared resource of Winship Cancer Institute of Emory University and NIH/NCI under award number P30CA138292. ARL is grateful for personal support from LTR and D. VF is grateful for mitochondria provided by Maria Olga Gonzalez.

References

Paste your main manuscript references here. They should be listed in order of citation.

Example References:

1. S. Zlatic, H. S. Comstra, A. Gokhale, M. J. Petris, V. Faundez, Molecular basis of neurodegeneration and neurodevelopmental defects in Menkes disease. *Neurobiol Dis* 81, 154-161 (2015).
2. S. Lutsenko, S. Roy, P. Tsvetkov, Mammalian Copper Homeostasis: Physiologic Roles and Molecular Mechanisms. *Physiol Rev* 10.1152/physrev.00011.2024 (2024).
3. R. El Meskini *et al.*, ATP7A (Menkes protein) functions in axonal targeting and synaptogenesis. *Mol Cell Neurosci* 34, 409-421 (2007).
4. M. J. Niciu *et al.*, Developmental changes in the expression of ATP7A during a critical period in postnatal neurodevelopment. *Neuroscience* 139, 947-964 (2006).
5. R. El Meskini, L. B. Cline, B. A. Eipper, G. V. Ronnett, The Developmentally Regulated Expression of Menkes Protein ATP7A Suggests a Role in Axon Extension and Synaptogenesis. *Developmental Neuroscience* 27, 333-348 (2005).
6. C. M. Opazo, M. A. Greenough, A. I. Bush, Copper: from neurotransmission to neuroproteostasis. *Frontiers in aging neuroscience* 6, 143-143 (2014).
7. D. J. Waggoner, T. B. Bartnikas, J. D. Gitlin, The role of copper in neurodegenerative disease. *Neurobiol Dis* 6, 221-230 (1999).
8. P. Büchler *et al.*, Hypoxia-inducible factor 1 regulates vascular endothelial growth factor expression in human pancreatic cancer. *Pancreas* 26, 56-64 (2003).
9. I. F. Scheiber, J. F. B. Mercer, R. Dringen, Metabolism and functions of copper in brain. *Progress in Neurobiology* 116, 33-57 (2014).
10. A. Hirano, J. F. Llena, J. H. French, N. R. Ghatak, Fine structure of the cerebellar cortex in Menkes Kinky-hair disease. X-chromosome-linked copper malabsorption. *Arch Neurol* 34, 52-56 (1977).

11. D. P. Purpura, A. Hirano, J. H. French, Polydendritic Purkinje cells in X-chromosome linked copper malabsorption: a Golgi study. *Brain Res* 117, 125-129 (1976).
12. N. M. Garza, A. B. Swaminathan, K. P. Maremanda, M. Zulkifli, V. M. Gohil, Mitochondrial copper in human genetic disorders. *Trends Endocrinol Metab* 34, 21-33 (2022).
13. P. Bülow, A. Patgiri, V. Faundez, Mitochondrial Protein Synthesis and the Bioenergetic Cost of Neurodevelopment. *iScience* 45, 283-296 (2022).
14. Manu S. Goyal, M. Hawrylycz, Jeremy A. Miller, Abraham Z. Snyder, Marcus E. Raichle, Aerobic Glycolysis in the Human Brain Is Associated with Development and Neotenous Gene Expression. *Cell Metabolism* 19, 49-57 (2014).
15. C. W. Kuzawa *et al.*, Metabolic costs and evolutionary implications of human brain development. *Proceedings of the National Academy of Sciences* 111, 13010-13015 (2014).
16. A. Oyarzábal, U. Musokhranova, L. Barros, A. García-Cazorla, Energy metabolism in childhood neurodevelopmental disorders. *EBioMedicine* 69 (2021).
17. P. Steiner, Brain fuel utilization in the developing brain. *Annals of Nutrition and Metabolism* 75, 8-18 (2020).
18. A. Rajan, R. M. Fame, Brain development and bioenergetic changes. *Neurobiol Dis* 199, 106550 (2024).
19. P. Casimir, R. Iwata, P. Vanderhaeghen, Linking mitochondria metabolism, developmental timing, and human brain evolution. *Curr Opin Genet Dev* 86, 102182 (2024).
20. R. Iwata *et al.*, Mitochondria metabolism sets the species-specific tempo of neuronal development. *Science* 0, eabn4705 (2023).
21. K. E. Vest, A. L. Paskavitz, J. B. Lee, T. Padilla-Benavides, Dynamic changes in copper homeostasis and post-transcriptional regulation of Atp7a during myogenic differentiation. *Metallomics* 10, 309-322 (2018).
22. X. Zheng *et al.*, Metabolic reprogramming during neuronal differentiation from aerobic glycolysis to neuronal oxidative phosphorylation. *Elife* 5 (2016).
23. D. Sakai *et al.*, Glycolytic activity is required for the onset of neural plate folding during neural tube closure in mouse embryos. *Front Cell Dev Biol* 11, 1212375 (2023).
24. R. Iwata, P. Vanderhaeghen, Metabolic mechanisms of species-specific developmental tempo. *Dev Cell* 59, 1628-1639 (2024).
25. D. Jimenez-Blasco *et al.*, Weak neuronal glycolysis sustains cognition and organismal fitness. *Nat Metab* 6, 1253-1267 (2024).
26. S. G. Kaler, ATP7A-related copper transport diseases-emerging concepts and future trends. *Nat Rev Neurol* 7, 15-29 (2011).
27. Z. Tümer, L. B. Møller, Menkes disease. *Eur J Hum Genet* 18, 511-518 (2010).
28. J. H. Menkes, M. Alter, G. K. Steigleder, D. R. Weakley, J. H. Sung, A sex-linked recessive disorder with retardation of growth, peculiar hair, and focal cerebral and cerebellar degeneration. *Pediatrics* 29, 764-779 (1962).
29. T. Skjørringe *et al.*, Characterization of ATP7A missense mutants suggests a correlation between intracellular trafficking and severity of Menkes disease. *Scientific reports* 7, 757-757 (2017).
30. M. Lenartowicz *et al.*, Mottled Mice and Non-Mammalian Models of Menkes Disease. *Frontiers in Molecular Neuroscience* 8 (2015).
31. L. M. Guthrie *et al.*, Elesclomol alleviates Menkes pathology and mortality by escorting Cu to cuproenzymes in mice. *Science* 368, 620 (2020).
32. S. Yuan, T. Korolnek, B. E. Kim, Oral Elesclomol Treatment Alleviates Copper Deficiency in Animal Models. *Front Cell Dev Biol* 10, 856300 (2022).
33. A. Donsante *et al.*, ATP7A gene addition to the choroid plexus results in long-term rescue of the lethal copper transport defect in a Menkes disease mouse model. *Mol Ther* 19, 2114-2123 (2011).

34. K. Yajima, K. Suzuki, Neuronal Degeneration in the Brain of the Brindled Mouse—A Light Microscope Study. *Journal of Neuropathology & Experimental Neurology* 38, 35-46 (1979).
35. T. Iwase *et al.*, Localization of Menkes gene expression in the mouse brain; its association with neurological manifestations in Menkes model mice. *Acta Neuropathol* 91, 482-488 (1996).
36. B. Sarkar, K. Lingertat-Walsh, J. T. Clarke, Copper-histidine therapy for Menkes disease. *J Pediatr* 123, 828-830 (1993).
37. S. G. Kaler *et al.*, Neonatal diagnosis and treatment of Menkes disease. *The New England journal of medicine* 358, 605-614 (2008).
38. T. Fujii, M. Ito, H. Tsuda, H. Mikawa, Biochemical study on the critical period for treatment of the mottled brindled mouse. *J Neurochem* 55, 885-889 (1990).
39. C. Fujisawa *et al.*, Early clinical signs and treatment of Menkes disease. *Mol Genet Metab Rep* 31, 100849 (2022).
40. S. Batzios *et al.*, Newly identified disorder of copper metabolism caused by variants in CTR1, a high-affinity copper transporter. *Hum Mol Genet* 31, 4121-4130 (2022).
41. C. Dame *et al.*, Fatal congenital copper transport defect caused by a homozygous likely pathogenic variant of SLC31A1. *Clin Genet* 103, 585-589 (2022).
42. T. R. Peterson *et al.*, DEPTOR is an mTOR inhibitor frequently overexpressed in multiple myeloma cells and required for their survival. *Cell* 137, 873-886 (2009).
43. A. Lane *et al.*, Sulfur- and phosphorus-standardized metal quantification of biological specimens using inductively coupled plasma mass spectrometry. *STAR Protocols* 3, 101334 (2022).
44. S. C. Wilschefski, M. R. Baxter, Inductively Coupled Plasma Mass Spectrometry: Introduction to Analytical Aspects. *Clin Biochem Rev* 40, 115-133 (2019).
45. J. R. Kirshner *et al.*, Elesclomol induces cancer cell apoptosis through oxidative stress. *Mol Cancer Ther* 7, 2319-2327 (2008).
46. L. Wu, L. Zhou, D. Q. Liu, F. G. Vogt, A. S. Kord, LC-MS/MS and density functional theory study of copper(II) and nickel(II) chelating complexes of elesclomol (a novel anticancer agent). *J Pharm Biomed Anal* 54, 331-336 (2011).
47. R. K. Blackman *et al.*, Mitochondrial electron transport is the cellular target of the oncology drug elesclomol. *PLoS One* 7, e29798 (2012).
48. S. Soma *et al.*, Elesclomol restores mitochondrial function in genetic models of copper deficiency. *Proc Natl Acad Sci U S A* 115, 8161-8166 (2018).
49. N. M. Garza, M. Zulkifli, V. M. Gohil, Elesclomol elevates cellular and mitochondrial iron levels by delivering copper to the iron import machinery. *J Biol Chem* 298, 102139 (2022).
50. D. E. Atkinson, G. M. Walton, Adenosine triphosphate conservation in metabolic regulation. Rat liver citrate cleavage enzyme. *J Biol Chem* 242, 3239-3241 (1967).
51. T. Tsang *et al.*, Copper is an essential regulator of the autophagic kinases ULK1/2 to drive lung adenocarcinoma. *Nat Cell Biol* 22, 412-424 (2020).
52. D. C. Brady *et al.*, Copper is required for oncogenic BRAF signalling and tumorigenesis. *Nature* 509, 492-496 (2014).
53. R. Huang *et al.*, The NCATS BioPlanet - An Integrated Platform for Exploring the Universe of Cellular Signaling Pathways for Toxicology, Systems Biology, and Chemical Genomics. *Front Pharmacol* 10, 445 (2019).
54. E. B. Wright, D. A. Lannigan, Therapeutic targeting of p90 ribosomal S6 kinase. *Front Cell Dev Biol* 11, 1297292 (2023).
55. O. Meyuhas, Ribosomal Protein S6 Phosphorylation: Four Decades of Research. *Int Rev Cell Mol Biol* 320, 41-73 (2015).
56. H. A. Acosta-Jaquez *et al.*, Site-specific mTOR phosphorylation promotes mTORC1-mediated signaling and cell growth. *Mol Cell Biol* 29, 4308-4324 (2009).
57. M. Rosner, N. Siegel, A. Valli, C. Fuchs, M. Hengstschläger, mTOR phosphorylated at S2448 binds to raptor and rictor. *Amino Acids* 38, 223-228 (2010).

58. J. Copp, G. Manning, T. Hunter, TORC-specific phosphorylation of mammalian target of rapamycin (mTOR): phospho-Ser2481 is a marker for intact mTOR signaling complex 2. *Cancer Res* 69, 1821-1827 (2009).
59. G. G. Chiang, R. T. Abraham, Phosphorylation of mammalian target of rapamycin (mTOR) at Ser-2448 is mediated by p70S6 kinase. *J Biol Chem* 280, 25485-25490 (2005).
60. M. K. Holz, J. Blenis, Identification of S6 kinase 1 as a novel mammalian target of rapamycin (mTOR)-phosphorylating kinase. *J Biol Chem* 280, 26089-26093 (2005).
61. K. A. Smolen *et al.*, Quantitative proteomics and phosphoproteomics of PP2A-PPP2R5D variants reveal deregulation of RPS6 phosphorylation via converging signaling cascades. *Journal of Biological Chemistry* 299, 105154 (2023).
62. B. Raught *et al.*, Serum-stimulated, rapamycin-sensitive phosphorylation sites in the eukaryotic translation initiation factor 4GI. *Embo j* 19, 434-444 (2000).
63. P. P. Roux *et al.*, RAS/ERK signaling promotes site-specific ribosomal protein S6 phosphorylation via RSK and stimulates cap-dependent translation. *J Biol Chem* 282, 14056-14064 (2007).
64. B. Magnuson, B. Ekim, D. C. Fingar, Regulation and function of ribosomal protein S6 kinase (S6K) within mTOR signalling networks. *Biochem J* 441, 1-21 (2012).
65. Y. M. Kim *et al.*, mTORC1 phosphorylates UVRAG to negatively regulate autophagosome and endosome maturation. *Mol Cell* 57, 207-218 (2015).
66. A. J. Covarrubias *et al.*, Akt-mTORC1 signaling regulates Acly to integrate metabolic input to control of macrophage activation. *Elife* 5 (2016).
67. C. Martinez Calejman *et al.*, mTORC2-AKT signaling to ATP-citrate lyase drives brown adipogenesis and de novo lipogenesis. *Nat Commun* 11, 575 (2020).
68. Y. Sancak *et al.*, PRAS40 is an insulin-regulated inhibitor of the mTORC1 protein kinase. *Mol Cell* 25, 903-915 (2007).
69. X. M. Ma, J. Blenis, Molecular mechanisms of mTOR-mediated translational control. *Nat Rev Mol Cell Biol* 10, 307-318 (2009).
70. Z. Peng *et al.*, AKT1 Regulates Endoplasmic Reticulum Stress and Mediates the Adaptive Response of Pancreatic β Cells. *Mol Cell Biol* 40 (2020).
71. Z. Mounir *et al.*, Akt Determines Cell Fate Through Inhibition of the PERK-eIF2α Phosphorylation Pathway. *Science Signaling* 4, ra62-ra62 (2011).
72. D. T. Hughes *et al.*, Targeting the kinase insert loop of PERK selectively modulates PERK signaling without systemic toxicity in mice. *Sci Signal* 13 (2020).
73. J. Bertinato, M. Iskandar, M. R. L'Abbé, Copper deficiency induces the upregulation of the copper chaperone for Cu/Zn superoxide dismutase in weanling male rats. *J Nutr* 133, 28-31 (2003).
74. B. E. Kim *et al.*, Cardiac copper deficiency activates a systemic signaling mechanism that communicates with the copper acquisition and storage organs. *Cell Metab* 11, 353-363 (2010).
75. G. Y. Liu, D. M. Sabatini, mTOR at the nexus of nutrition, growth, ageing and disease. *Nat Rev Mol Cell Biol* 21, 183-203 (2020).
76. S. W. Cheng, L. G. Fryer, D. Carling, P. R. Shepherd, Thr2446 is a novel mammalian target of rapamycin (mTOR) phosphorylation site regulated by nutrient status. *J Biol Chem* 279, 15719-15722 (2004).
77. T. H. t. Reynolds, S. C. Bodine, J. C. Lawrence, Jr., Control of Ser2448 phosphorylation in the mammalian target of rapamycin by insulin and skeletal muscle load. *J Biol Chem* 277, 17657-17662 (2002).
78. B. T. Navé, M. Ouwens, D. J. Withers, D. R. Alessi, P. R. Shepherd, Mammalian target of rapamycin is a direct target for protein kinase B: identification of a convergence point for opposing effects of insulin and amino-acid deficiency on protein translation. *Biochem J* 344 Pt 2, 427-431 (1999).
79. N. Pullen *et al.*, Phosphorylation and activation of p70s6k by PDK1. *Science* 279, 707-710 (1998).

80. P. E. Burnett, R. K. Barrow, N. A. Cohen, S. H. Snyder, D. M. Sabatini, RAFT1 phosphorylation of the translational regulators p70 S6 kinase and 4E-BP1. *Proc Natl Acad Sci U S A* 95, 1432-1437 (1998).
81. A. Ianevski, A. K. Giri, T. Aittokallio, SynergyFinder 3.0: an interactive analysis and consensus interpretation of multi-drug synergies across multiple samples. *Nucleic Acids Research* 50, W739-W743 (2022).
82. B. Yadav, K. Wennerberg, T. Aittokallio, J. Tang, Searching for Drug Synergy in Complex Dose-Response Landscapes Using an Interaction Potency Model. *Comput Struct Biotechnol J* 13, 504-513 (2015).
83. L. M. Ballou, R. Z. Lin, Rapamycin and mTOR kinase inhibitors. *J Chem Biol* 1, 27-36 (2008).
84. Y. Zheng, Y. Jiang, mTOR Inhibitors at a Glance. *Mol Cell Pharmacol* 7, 15-20 (2015).
85. E. K. Schmidt, G. Clavarino, M. Ceppi, P. Pierre, SUnSET, a nonradioactive method to monitor protein synthesis. *Nat Methods* 6, 275-277 (2009).
86. A. P. Grollman, Structural basis for inhibition of protein synthesis by emetine and cycloheximide based on an analogy between ipecac alkaloids and glutarimide antibiotics. *Proc Natl Acad Sci U S A* 56, 1867-1874 (1966).
87. R. Mukhopadhyay *et al.*, Efficacy and Mechanism of Action of Low Dose Emetine against Human Cytomegalovirus. *PLoS Pathog* 12, e1005717 (2016).
88. S. M. Grist, L. Chrostowski, K. C. Cheung, Optical oxygen sensors for applications in microfluidic cell culture. *Sensors (Basel)* 10, 9286-9316 (2010).
89. N. Wit *et al.*, A histone deacetylase 3 and mitochondrial complex I axis regulates toxic formaldehyde production. *Sci Adv* 9, eadg2235 (2023).
90. Y. Wang *et al.*, Maternofetal and neonatal copper requirements revealed by enterocyte-specific deletion of the Menkes disease protein. *Am J Physiol Gastrointest Liver Physiol* 303, G1236-1244 (2012).
91. N. Barnes, R. Tsivkovskii, N. Tsivkovskaia, S. Lutsenko, The copper-transporting ATPases, Menkes and Wilson disease proteins, have distinct roles in adult and developing cerebellum. *J Biol Chem* 280, 9640-9645 (2005).
92. E. D. Gaier *et al.*, Peptidylglycine α-amidating monooxygenase heterozygosity alters brain copper handling with region specificity. *J Neurochem* 127, 605-619 (2013).
93. D. R. Zollinger, S. E. Lingle, K. Sorg, J. M. Beechem, C. R. Merritt, GeoMx™ RNA Assay: High Multiplex, Digital, Spatial Analysis of RNA in FFPE Tissue. *Methods Mol Biol* 2148, 331-345 (2020).
94. J. Decalf, M. L. Albert, J. Ziai, New tools for pathology: a user's review of a highly multiplexed method for in situ analysis of protein and RNA expression in tissue. *J Pathol* 247, 650-661 (2019).
95. C. R. Merritt *et al.*, Multiplex digital spatial profiling of proteins and RNA in fixed tissue. *Nat Biotechnol* 38, 586-599 (2020).
96. V. Kozareva *et al.*, A transcriptomic atlas of mouse cerebellar cortex comprehensively defines cell types. *Nature* 598, 214-219 (2021).
97. S. Rath *et al.*, MitoCarta3.0: an updated mitochondrial proteome now with sub-organelle localization and pathway annotations. *Nucleic Acids Res* 49, D1541-d1547 (2021).
98. A. Liberzon *et al.*, Molecular signatures database (MSigDB) 3.0. *Bioinformatics* 27, 1739-1740 (2011).
99. W. Cai *et al.*, Domain-dependent effects of insulin and IGF-1 receptors on signalling and gene expression. *Nat Commun* 8, 14892 (2017).
100. A. Subramanian *et al.*, Gene set enrichment analysis: a knowledge-based approach for interpreting genome-wide expression profiles. *Proc Natl Acad Sci U S A* 102, 15545-15550 (2005).
101. G. Korotkevich, V. Sukhov, A. Sergushichev, Fast gene set enrichment analysis. *bioRxiv* 10.1101/060012, 060012 (2019).
102. M. Norgate *et al.*, Essential roles in development and pigmentation for the Drosophila copper transporter DmATP7. *Mol Biol Cell* 17, 475-484 (2006).

103. J. E. Hwang, M. de Bruyne, C. G. Warr, R. Burke, Copper overload and deficiency both adversely affect the central nervous system of Drosophila. *Metallomics* 6, 2223-2229 (2014).
104. T. Binks, J. C. Lye, J. Camakaris, R. Burke, Tissue-specific interplay between copper uptake and efflux in Drosophila. *J Biol Inorg Chem* 15, 621-628 (2010).
105. C. Hartwig *et al.*, Golgi-Dependent Copper Homeostasis Sustains Synaptic Development and Mitochondrial Content. *J Neurosci* 41, 215-233 (2020).
106. A. Gokhale *et al.*, The Proteome of BLOC-1 Genetic Defects Identifies the Arp2/3 Actin Polymerization Complex to Function Downstream of the Schizophrenia Susceptibility Factor Dysbindin at the Synapse. *J Neurosci* 36, 12393-12411 (2016).
107. H. Barcelo, M. J. Stewart, Altering Drosophila S6 kinase activity is consistent with a role for S6 kinase in growth. *Genesis* 34, 83-85 (2002).
108. M. Miron *et al.*, The translational inhibitor 4E-BP is an effector of PI(3)K/Akt signalling and cell growth in Drosophila. *Nat Cell Biol* 3, 596-601 (2001).
109. X. Qin, B. Jiang, Y. Zhang, 4E-BP1, a multifactor regulated multifunctional protein. *Cell Cycle* 15, 781-786 (2016).
110. M. Morita *et al.*, mTOR coordinates protein synthesis, mitochondrial activity and proliferation. *Cell Cycle* 14, 473-480 (2015).
111. M. Morita *et al.*, mTORC1 controls mitochondrial activity and biogenesis through 4E-BP-dependent translational regulation. *Cell Metab* 18, 698-711 (2013).
112. N. R. Ghatak, A. Hirano, T. P. Poon, J. H. French, Trichopoliodystrophy. II. Pathological changes in skeletal muscle and nervous system. *Arch Neurol* 26, 60-72 (1972).
113. L. Vagn-Hansen, E. Reske-Nielsen, H. C. Lou, Menkes' disease--a new leucodystrophy (?). A clinical and neuropathological review together with a new case. *Acta Neuropathol* 25, 103-119 (1973).
114. D. Troost, A. van Rossum, W. Straks, J. Willemse, Menkes' kinky hair disease. II. A clinicopathological report of three cases. *Brain Dev* 4, 115-126 (1982).
115. H. Kodama, C. Fujisawa, W. Bhadhprasit, Inherited copper transport disorders: biochemical mechanisms, diagnosis, and treatment. *Curr Drug Metab* 13, 237-250 (2012).
116. T. Yamano, K. Suzuki, Abnormalities of Purkinje cell arborization in brindled mouse cerebellum. A Golgi study. *J Neuropathol Exp Neurol* 44, 85-96 (1985).
117. M. J. Niciu *et al.*, Altered ATP7A expression and other compensatory responses in a murine model of Menkes disease. *Neurobiol Dis* 27, 278-291 (2007).
118. Y. Sakai *et al.*, Hyperactivation of mTORC1 disrupts cellular homeostasis in cerebellar Purkinje cells. *Sci Rep* 9, 2799 (2019).
119. C. Fecher *et al.*, Cell-type-specific profiling of brain mitochondria reveals functional and molecular diversity. *Nature Neuroscience* 22, 1731-1742 (2019).
120. M. E. Wynne *et al.*, Heterogeneous Expression of Nuclear Encoded Mitochondrial Genes Distinguishes Inhibitory and Excitatory Neurons. *eNeuro* 8, ENEURO.0232-0221.2021 (2021).
121. K. Bredvik, T. A. Ryan, Differential Control of Inhibitory and Excitatory Nerve Terminal Function by Mitochondria. *bioRxiv* 10.1101/2024.05.19.594864, 2024.2005.2019.594864 (2024).
122. S. C. Johnson *et al.*, mTOR inhibition alleviates mitochondrial disease in a mouse model of Leigh syndrome. *Science* 342, 1524-1528 (2013).
123. N. A. Khan *et al.*, mTORC1 Regulates Mitochondrial Integrated Stress Response and Mitochondrial Myopathy Progression. *Cell Metabolism* 26, 419-428.e415 (2017).
124. R. Perez-Gomez, V. Magnin, Z. Mihajlovic, V. Slaninova, A. Krejci, Downregulation of respiratory complex I mediates major signalling changes triggered by TOR activation. *Sci Rep* 10, 4401 (2020).

125. Y. Wang, S. Hekimi, Minimal mitochondrial respiration is required to prevent cell death by inhibition of mTOR signaling in CoQ-deficient cells. *Cell Death Discov* 7, 201 (2021).
126. P. B. Dennis *et al.*, Mammalian TOR: a homeostatic ATP sensor. *Science* 294, 1102-1105 (2001).
127. X. M. Ma, S. O. Yoon, C. J. Richardson, K. Jülich, J. Blenis, SKAR links pre-mRNA splicing to mTOR/S6K1-mediated enhanced translation efficiency of spliced mRNAs. *Cell* 133, 303-313 (2008).
128. M. R. Wieckowski, C. Giorgi, M. Lebiedzinska, J. Duszynski, P. Pinton, Isolation of mitochondria-associated membranes and mitochondria from animal tissues and cells. *Nat Protoc* 4, 1582-1590 (2009).
129. I. Wittig, H. P. Braun, H. Schägger, Blue native PAGE. *Nat Protoc* 1, 418-428 (2006).
130. A. Timón-Gómez *et al.*, Protocol for the Analysis of Yeast and Human Mitochondrial Respiratory Chain Complexes and Supercomplexes by Blue Native Electrophoresis. *STAR Protoc* 1 (2020).
131. F. Díaz, A. Barrientos, F. Fontanesi, Evaluation of the mitochondrial respiratory chain and oxidative phosphorylation system using blue native gel electrophoresis. *Curr Protoc Hum Genet* Chapter 19, Unit19.14 (2009).
132. S. Zheng *et al.*, SynergyFinder Plus: Toward Better Interpretation and Annotation of Drug Combination Screening Datasets. *Genomics Proteomics Bioinformatics* 20, 587-596 (2022).
133. L. Ping *et al.*, Global quantitative analysis of the human brain proteome in Alzheimer's and Parkinson's Disease. *Scientific Data* 5, 180036 (2018).
134. M. E. Wynne *et al.*, APOE expression and secretion are modulated by mitochondrial dysfunction. *Elife* 12 (2023).
135. W. B. Grueber *et al.*, Projections of Drosophila multidendritic neurons in the central nervous system: links with peripheral dendrite morphology. *Development* 134, 55-64 (2007).
136. R. Das *et al.*, Dendritic Cytoskeletal Architecture Is Modulated by Combinatorial Transcriptional Regulation in Drosophila melanogaster. *Genetics* 207, 1401-1421 (2017).
137. C. A. Schneider, W. S. Rasband, K. W. Eliceiri, NIH Image to ImageJ: 25 years of image analysis. *Nat Methods* 9, 671-675 (2012).
138. C. Arshadi, U. Günther, M. Eddison, K. I. S. Harrington, T. A. Ferreira, SNT: a unifying toolbox for quantification of neuronal anatomy. *Nat Methods* 18, 374-377 (2021).
139. R Core Team (2021) R: A Language and Environment for Statistical Computing. (R Foundation for Statistical Computing, Vienna).
140. E. W. Deutsch *et al.*, The ProteomeXchange consortium in 2020: enabling 'big data' approaches in proteomics. *Nucleic Acids Research* 48, D1145-D1152 (2020).
141. J. Ho, T. Tumkaya, S. Aryal, H. Choi, A. Claridge-Chang, Moving beyond P values: data analysis with estimation graphics. *Nature Methods* 16, 565-566 (2019).
142. Y. Zhou *et al.*, Metascape provides a biologist-oriented resource for the analysis of systems-level datasets. *Nat Commun* 10, 1523 (2019).
143. T. M. Iverson, P. K. Singh, G. Cecchini, An evolving view of complex II-noncanonical complexes, megacomplexes, respiration, signaling, and beyond. *J Biol Chem* 299, 104761 (2023).

Figures and Tables

Figure 1. CTR1 (*SLC31A1*) null mutation disrupts electron transport chain assembly and function and increases glycolysis. A. Immunoblot of cellular extracts from wild-type (lane 1) and two independent *SLC31A1Δ/Δ* mutant (CTR1 KO, lanes 2-3) SH-SY5Y cell clones probed for CTR1 and DBH with beta-actin as a loading control. **B.** 63Cu quantification in whole cells or mitochondria in CTR1 KO cells treated with vehicle or 1 nM elesclomol, normalized to 32S. Italicized numbers represent q values (One-Way ANOVA, followed by Benjamini, Krieger, and Yekutieli multiple comparisons correction). **C.** Immunoblot with OxPhos antibody mix in mitochondrial fractions from wild-type and CTR1 KO cells. Complex II was used as a loading control as it does not form respiratory supercomplexes (143). (Each dot is an independent biological replicate. Italicized numbers represent p values analyzed by two-sided permutation t-test.) **D.** Blue native electrophoresis of mitochondrial fractions from wild-type and CTR1 KO cells (Clone KO3) solubilized in either DDM or digitonin to preserve or dissolve supercomplexes, respectively (129, 130). Shown are native gel immunoblots probed with antibodies against Complex, I, II, III, and IV. Italicized numbers represent p values. Complex II was used as a loading control. Immunoblots were also prepared with CTR1 clone KO20 (not shown). **E-G.** Seahorse stress tests in wild-type and CTR1 KO cells. Arrows indicate the sequential addition of oligomycin (a), FCCP (b), and rotenone-antimycin (c) in the Mito Stress Test (**E**) to cells treated with vehicle, 1 nM elesclomol, or 200 μM BCS for 72 hours (**E, F**, BCS n =3, all other treatments n=6-7) or the addition of glucose (a), oligomycin (b), and 2-Deoxy-D-glucose (c) in the Glycolysis Stress Test (**G**, n=3). Basal cellular respiration and glycolysis were measured for 90 min after additions using Seahorse. **E**,**F**. Mito Stress Test data are presented normalized to basal respiration of wild-type cells in the absence of drug, analyzed by a One-Way ANOVA followed by Benjamini, Krieger, and Yekutieli multiple comparisons correction (italics show q values). CTR1 clone KO20 was used. **G**. Glycolysis Stress Test data are presented normalized to protein, analyzed by two-sided permutation t-test (italicized numbers represent p values). All data are presented as average ± SEM.

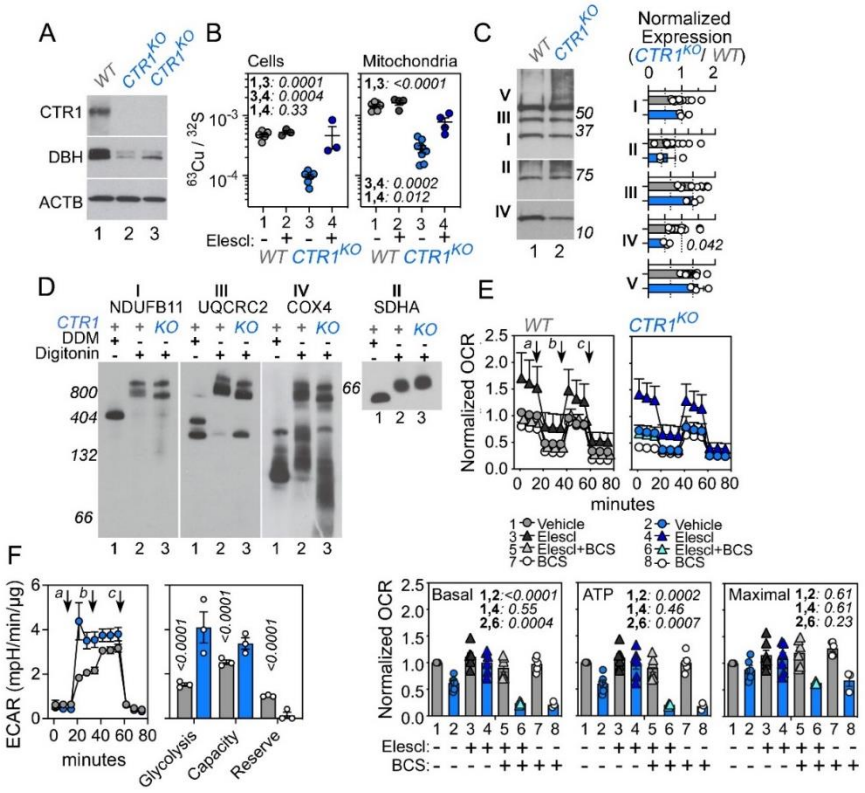

Figure S1. Generation and Characterization of CTR1 (*SLC31A1*) Null Mutant Neuroblastoma Cells. A. DNA sequence chromatograms of one wild type and three *SLC31A1* CRISPR-edited SH-SY5Y clonal lines. Blue boxes mark the mutated sequence. **B.** Cell survival analysis of *SLC31A1* mutants with increasing concentrations of copper. Blue shaded symbols represent three different clones (n=3 replicates for 1 or 3 clones for wild type or *SLC31A1* mutants respectively). **C.** Cell survival analysis of wild type and CTR1 mutants with increasing concentrations of elesclomol (n = 11 and 14, p value Sum-of-squares F test analysis). **D.** 64Zn quantification in whole cells or mitochondria in CTR1 KO cells treated with vehicle or 1 nM elesclomol, normalized to 32S. There are no significant differences by treatment or genotype as assessed by One-Way ANOVA, followed by Benjamini, Krieger, and Yekutieli multiple comparisons correction. **E.** Metabolic map of basal OCR and ECAR from the Mito Stress Test of wild-type and CTR1 KO cells (clone KO20) normalized to untreated wild-type cells treated with vehicle, elesclomol, or BCS as described in Fig. 1. **F-G**. Mass spectrometry quantification of metabolites, analyzed by One-Way ANOVA followed by Benjamini, Krieger, and Yekutieli multiple comparisons correction. CTR1 clone KO20 was used. **G**. Quantification of energy charge, calculated by dividing the amount of [ATP] + 0.5[ADP] by the total levels of [ATP]+[ADP]+[AMP] (50). Heat maps show the levels of the adenylate nucleotides used for the calculation and GTP for comparison. **G.** Quantification of lactate levels. All data are presented as average ± SEM.

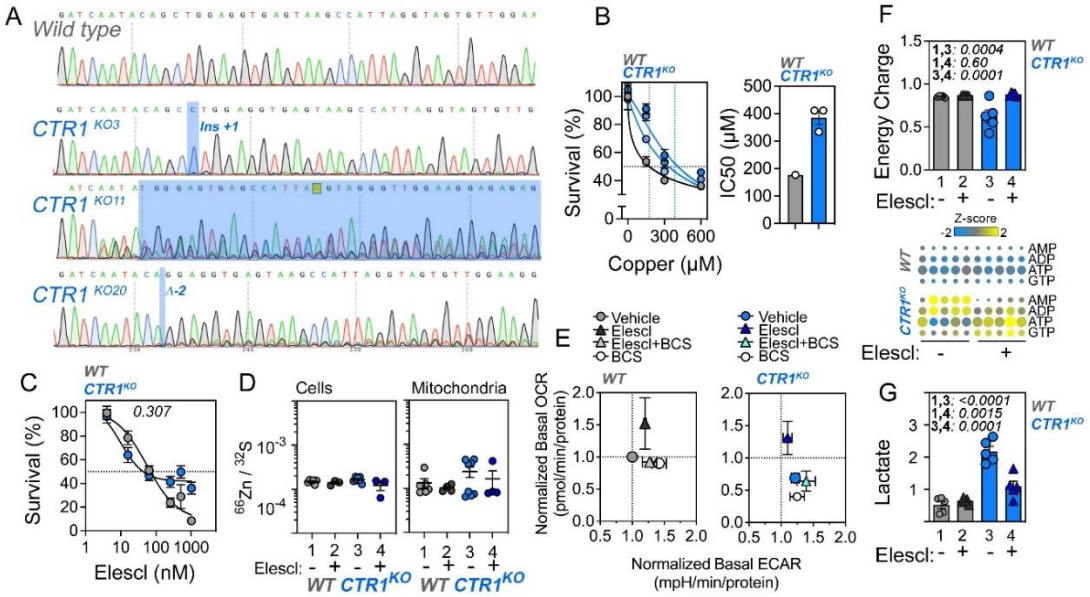

Figure 2. CTR1 mutant proteome and phosphoproteome have increased activation of mTOR-Raptor-S6K signaling and protein synthesis pathways. A. Volcano plots of the CTR1 KO cell proteome and phosphoproteome, where yellow dots represent proteins or phosphoproteins whose expression is increased in KO cells and blue dots represent decreased expression in KO cells. n=4 for wild type cells and n=4 for KO cells in two independent clones (KO3 and KO11). **B.** Principle component analysis (PCA) of the whole proteome and phosphoproteome from wild type (gray) and two CTR1 KO clonal lines (blue symbols). Hierarchical clustering and PCA of all proteome or phosphoproteome hits where differential expression is significant with q<0.05 and a fold of change of 1.5 (t-test followed by Benjamini-Hochberg FDR correction). **C.** Replication TMT Proteome in independent CTR1 KO clone experiment (KO3 and KO20), Venn diagram overlap p value calculated with a hypergeometric test. Merged protein-protein interaction network of both TMT experiments is enriched in the GO term GO:0006091 generation of precursor metabolites and energy. **D.** TMT proteome levels of Complex IV subunits and assembly factors expressed as Z-score. All these proteins changed more than 1.5-fold as compared to wild type cells with a q<0.05. **E.** Gene ontology analysis differentially expressed proteins or phosphopeptides in CTR1 mutant proteome and phosphoproteome. Bioplanet and KEGG databases were queried with the ENRICHR engine. Fisher exact test followed by Benjamini-Hochberg correction. **F.** Metascape analysis of the proteome and phosphoproteome. Ontology enrichment analysis was applied to a protein-protein interaction network of all components to select molecular complexes with MCODE based on significant ontologies. **G.** mTOR signaling pathway diagram modified from KEGG map04150. **H.** Mass spectrometry quantification of ontologically selected proteins and phosphopeptides. Proteins are shown with blue circles and phosphopeptides are shown with red squares. Vertical numbers represent q values. See Supplementary File 1 for raw data.

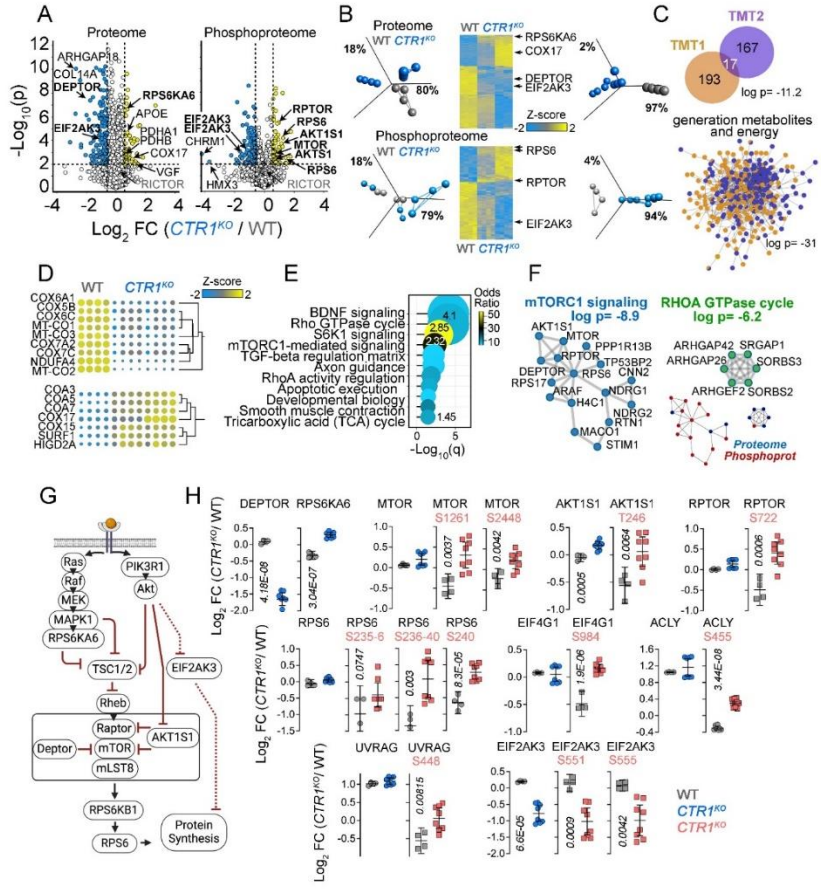

Figure S2. Transcript changes in CTR1 mutants reflect increased activation of the mTOR and PI3K-Akt signaling pathways. A. Principal component analysis of the Metabolic and Neuropathology annotated transcriptomes from wild type (gray) or CTR1 KO (blue symbols; KO20) clonal lines in the absence or presence of BCS (200 μM, 72 hours). **B.** Hierarchical clustering of the metabolism annotated transcriptome differentially expressed at a significancy of q<0.05 (analyzed by one-way ANOVA followed by Benjamini-Hochberg FDR correction). **C.** mTOR pathway annotated transcript levels, expressed as relative level. Each of these transcripts changed >1.5-fold as compared to wild type cells (q<0.05). **D.** Gene ontology analysis of metabolism annotated transcripts with increased or decreased expression in CTR1 mutants. KEGG database was queried with the ENRICHR engine. Fisher exact test followed by Benjamini-Hochberg correction. **E.** mTOR signaling pathway diagram modified from KEGG map04150. See Supplementary File 1 for raw data.

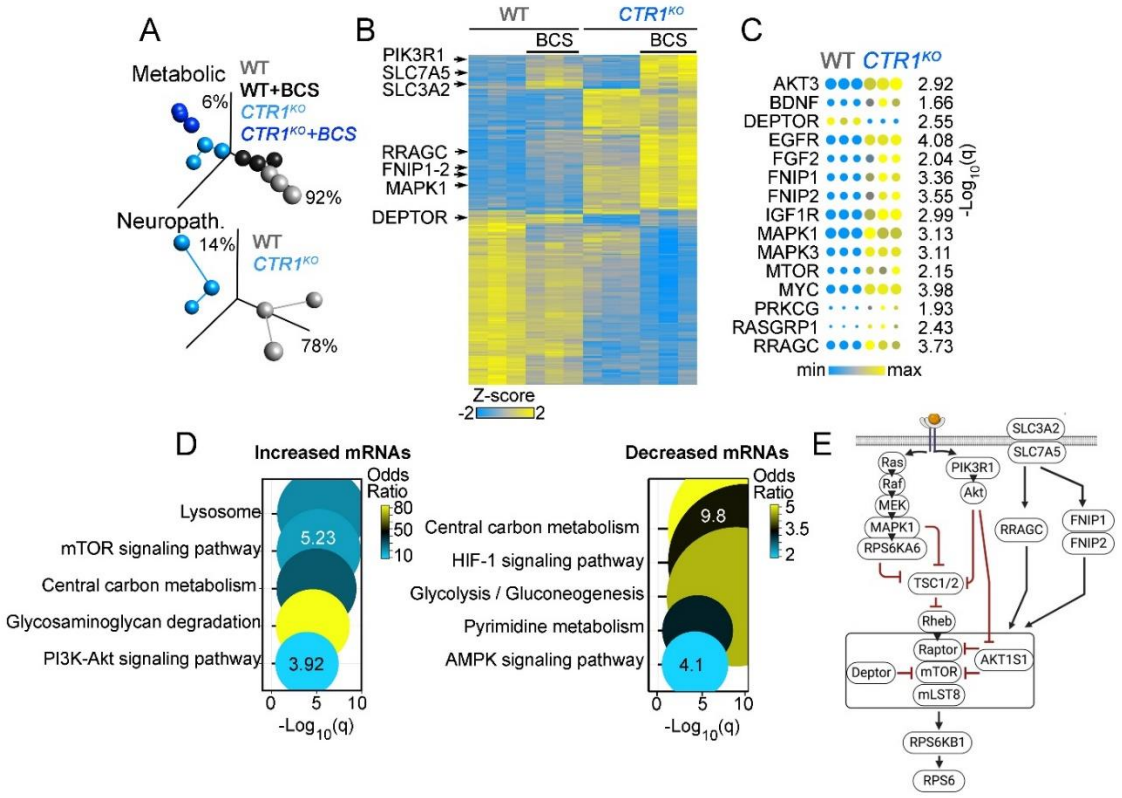

Figure 3. Increased activity of the mTOR-S6K pathway in CTR1 KO cells. A. Immunoblots of whole-cell extracts from wild-type and CTR1 mutant cells probed for ATP7A, COX17, CCS, DEPTOR, RAPTOR, RICTOR, and EIF2AK3 with actin as a loading control. Immunoblots were quantified by normalizing expression to wild-type cells. Italicized numbers represent p values analyzed by two-sided permutation t-test. **B,C.** Immunoblots with antibodies detecting either phosphorylated or total mTOR or S6K as loading controls after overnight depletion of fetal bovine serum followed by serum addition for 0.5-2 hours (**B**, top) or at time 0 followed removal of fetal bovine serum for 2-6 hours (**C**, bottom). Graphs depict quantitation of blots on the left in 3-6 independent replicates as the ratio of the phosphorylated to total protein content, normalized to control at time 0 (**C**) or time at 2 hours (**B**) (Two-Way ANOVA followed by Benjamini, Krieger, and Yekutiel corrections).

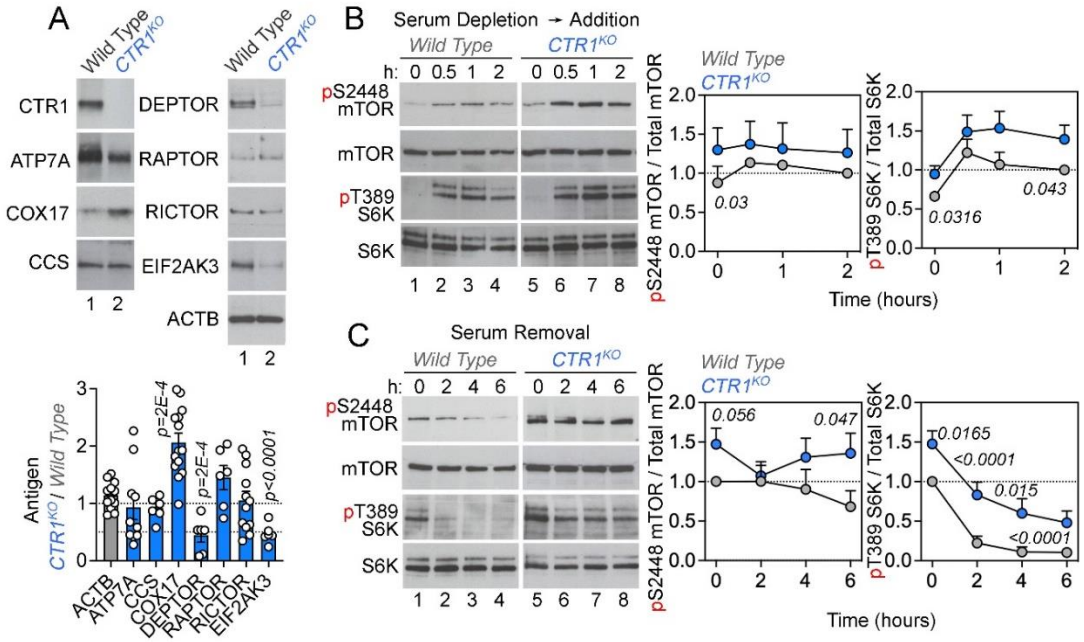

Figure 4. CTR1 knockout increases susceptibility to mTOR inhibition. A. Cell survival analysis of CTR1 mutants with increasing concentrations of serum or insulin (average ± SEM, n = 7 for serum and 5 for insulin, two-way ANOVA followed by Benjamini, Krieger, and Yekutieli corrections). **B-G.** Synergy analysis of cell survival of CTR1 mutants treated with increasing concentrations of combinations of the compounds serum, rapamycin, Torin-2, BCS, and elesclomol. **B.** Cell survival map for cells treated with serum and rapamycin, with the corresponding interaction synergy map calculated using the Zero Interaction Potency (ZIP) score for cell survival (82) (**D**). **C-G.** Scores below -10 indicate an antagonistic interaction between the compounds. Maps were generated with at least six independent experiments per pair that generated percent cell survival maps presented in Fig. S4-1 and average ZIP score for drug interactions in **C** or weighted ZIP score in **E** (see Methods). Average ± SEM, two-sided permutation t-test. **E-G.** Synergy analysis of CTR1 mutants with increasing concentrations of Torin-2 and elesclomol, with different colors and symbols indicating increasing concentrations of elesclomol (**F**) with average weighted ZIP score (**E**, two-sided permutation t-test) and elesclomol ZIP interaction synergy map (**G**).

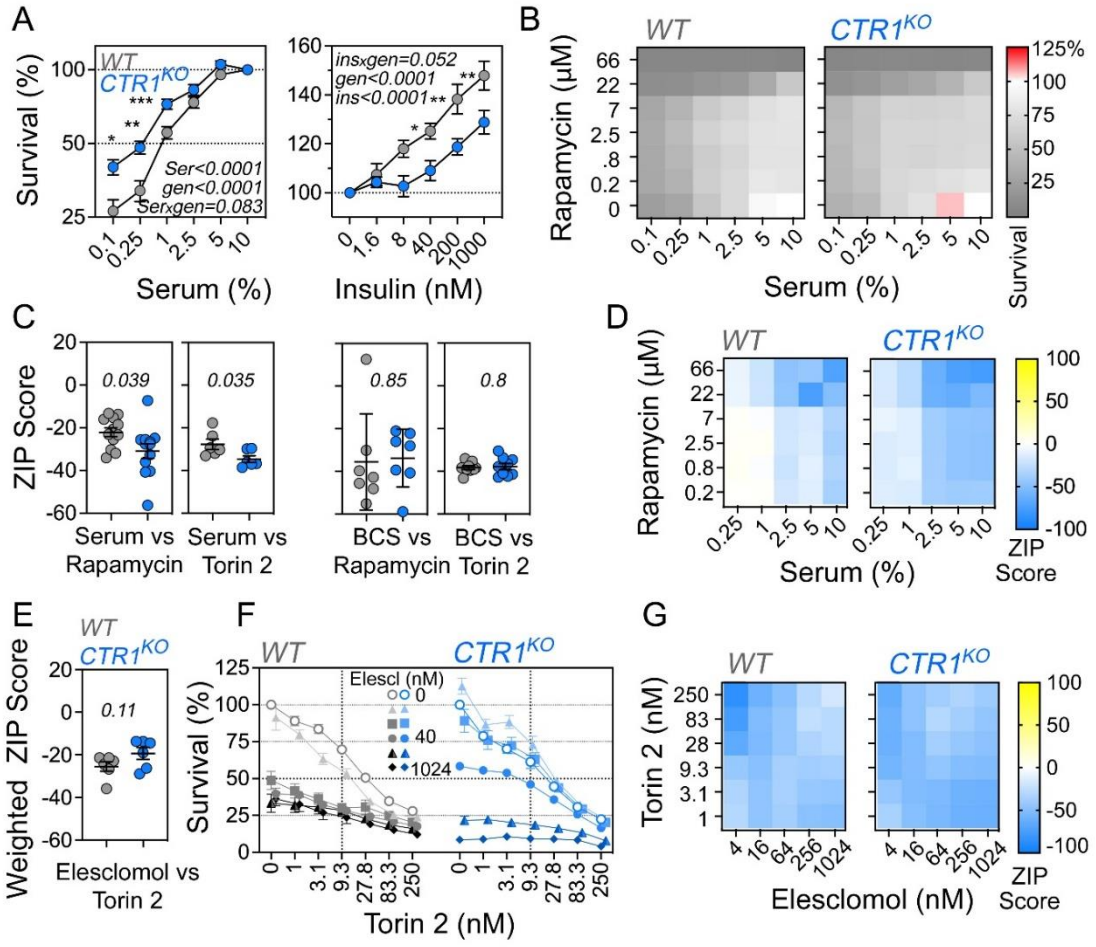

Figure S4-1. mTOR inhibitors reduce phosphorylation of mTOR and S6K. Immunoblot of total and phosphorylated mTOR and S6K after overnight serum depletion in 0.2% serum, 30-minute pretreatment with rapamycin (270 nM) or Torin-2 (1 nM) in existing 0.2% serum media, followed by a switch to fresh media with 0.2% or 20% serum, rapamycin, and/or Torin-2 for 30 minutes.

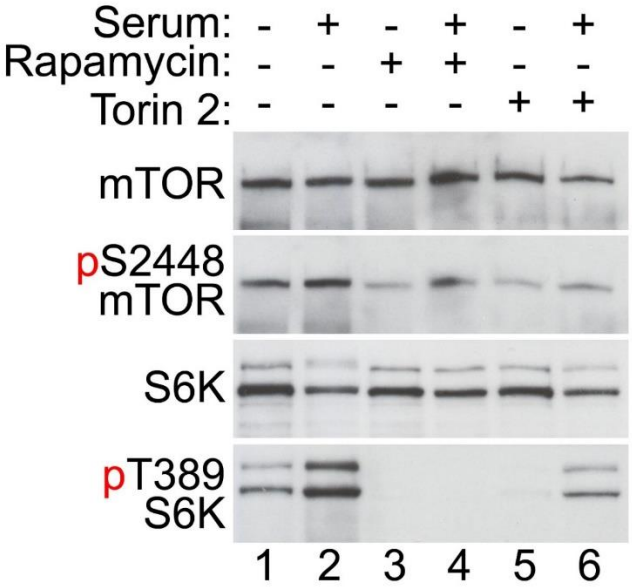

Figure S4-2. Synergy analysis of CTR1 mutant cells. A-D. Quantification of survival and drug synergy in wild-type and CTR1 mutant cells treated with Torin-2 and serum (**A**), Torin-2 and BCS (**B**), rapamycin and BCS (**C**), or Torin-2 and elesclomol (**D**). Gray panels represent cell survival normalized to untreated cells, as described in Figure 4. Blue panels represent the corresponding interaction synergy map calculated using the Zero Interaction Potency (ZIP) score for cell survival (82) (refer to Figure 4).

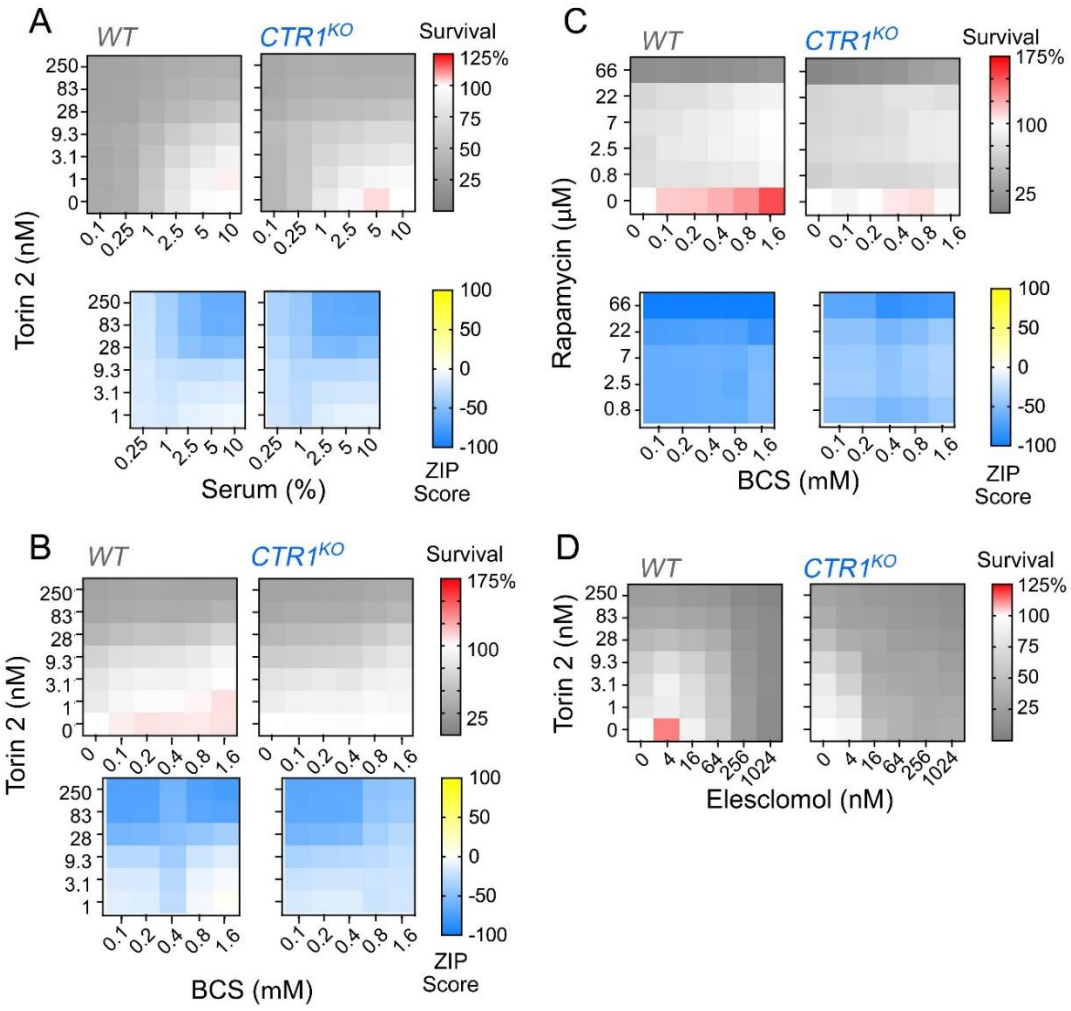

Figure 5. CTR1 mutant cells are resistant to protein synthesis inhibition. A. Immunoblot for puromycin in wild-type (lanes 1 and 2) and CTR1 mutant cells (lanes 3 and 4) treated with either vehicle (lanes 1 and 3) or 240 nM emetine (lanes 2 and 4) for 24 hours, followed by a 30 min pulse of puromycin. Quantification of the puromycin signal between 250 and 15 kDa normalized to HSP90. One-Way ANOVA, followed by Holm-Šídák's multiple comparisons test. CTR1 clone KO20 was used for all experiments. **B-D.** Resipher respiration rates in wild type and CTR1 KO cells. Cells were grown in complete 10% serum media unless otherwise specified. Cells were incubated for 48h, followed by serum depletion (**B**, serum 0.16%), vehicle (**C**, DMSO), or emetine (**D**, 60 or 240 nM) for 24h. **B-D.** Assay was terminated at 72 h by the addition of rotenone plus antimycin (R+A). Columns 1 and 2 represent raw or normalized OCR, respectively, presented as OCR over time or the integrated area under the curve (AUC) for the indicated time periods. Each dot depicts a batch of concurrent experiments (n=4-7 per genotype for each experiment, average ± SEM, two-sided permutation t-test).

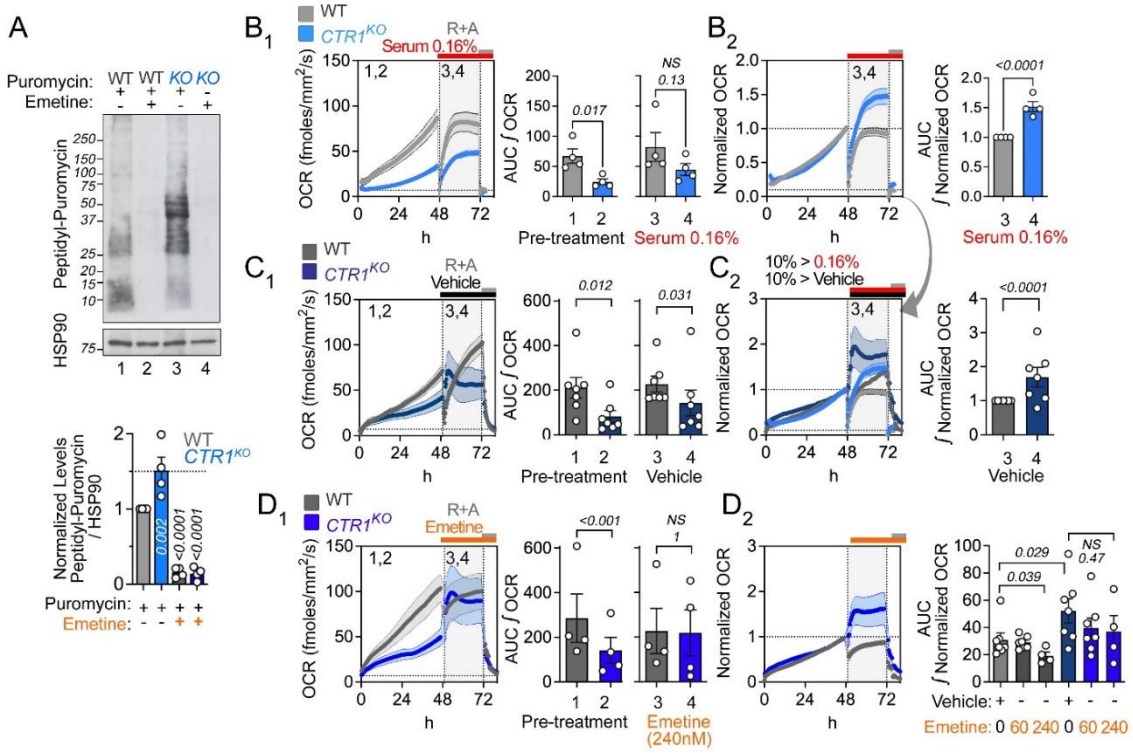

Figure S5. Cell survival under conditions inhibiting protein synthesis. A-B. Immunoblot for puromycin using a nitrocellulose membrane in wild-type and CTR1 mutant cells treated with vehicle (lanes 1 and 2) or puromycin for 30 min (lanes 3 and 4). Line trace represents the corresponding quantification of signal intensity. **B.** Quantification of the puromycin signal between 250 and 15 kDa normalized to HSP90. Paired two-tailed t test (pairing r=0.86, p=0.0007). **C-D.** Cell growth analysis of wild type and CTR1 mutants with increasing concentrations of emetine for 24 hours (**D**, Average ± SEM, n = 6, p value calculated with Sum-of-squares F test analysis) and corresponding IC50 (**B**, two-sided permutation t-test), as measured by Alamar blue. **E.** Cell growth of wild type and CTR1 KO cells in complete media and serum depletion after 48h as measured by total protein, normalized to the seeding cell number at time zero. Insert shows the percent difference in cell counts after the initial 48h. n=4 Average ± SEM. **F.** Normalized cell counts in wild type and CTR1 KO cells either in the absence or presence of 240 nM emetine for the indicated times. CTR1 clone KO20 was used for all experiments in **C-F**.

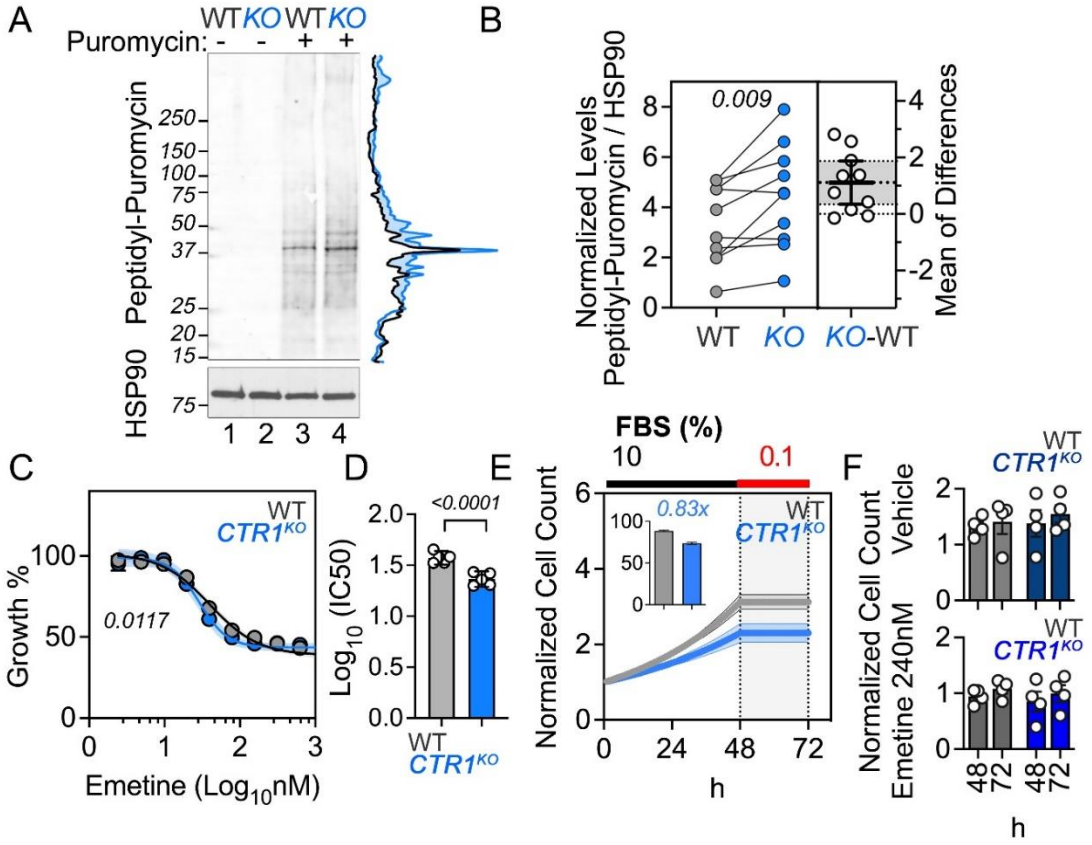

Figure 6. Transcriptome of cerebellar cortex layers in a presymptomatic Menkes mouse model. A. Sagittal sections of control and *Atp7a*$^{flx/Y}$ :: *Vil1*$^{Cre/+}$ mutants at day 10 stained with Syto83 and GFAP to distinguish cerebellar layers. **B.** ROIs corresponding to the two AOIs analyzed: the GFAP-negative Purkinje cell layer AOI and the GFAP-positive granular layer AOI. **C.** Normalized mRNA counts for the Purkinje cell markers *Calb1* and *Pcp2* in the Purkinje and granular layer AOIs. **D.** Normalized mRNA counts for insulin and mTOR-S6 kinase related genes. Blue denotes mutant. n = 16 control AOIs and 13 mutant *Atp7a*$^{flx/Y}$ :: *Vil1*$^{Cre/+}$ AOIs, 4 animals of each genotype. **E.** Expression of Igf1r and p-Igf1r (Tyr1135/Tyr1136) as measured by LFQ-MS or Luminex, respectively. Box plots are all two-sided permutation t-tests. **F.** Volcano plot of mRNAs differentially expressed in mutant *Atp7a*$^{flx/Y}$ :: *Vil1*$^{Cre/+}$ Purkinje neurons vs control. Yellow symbols mark genes with increased expression in mutant *Atp7a*$^{flx/Y}$ :: *Vil1*$^{Cre/+}$ Purkinje cells. **G.** Gene Set Enrichment Analysis and normalized enrichment score (NES) of genes differentially expressed by comparing controls to mutant *Atp7a*$^{flx/Y}$ :: *Vil1*$^{Cre/+}$ Purkinje cells. Gene sets enriched in mutants correspond to negative NES. p values are corrected. See Supplementary File 2 for raw data.

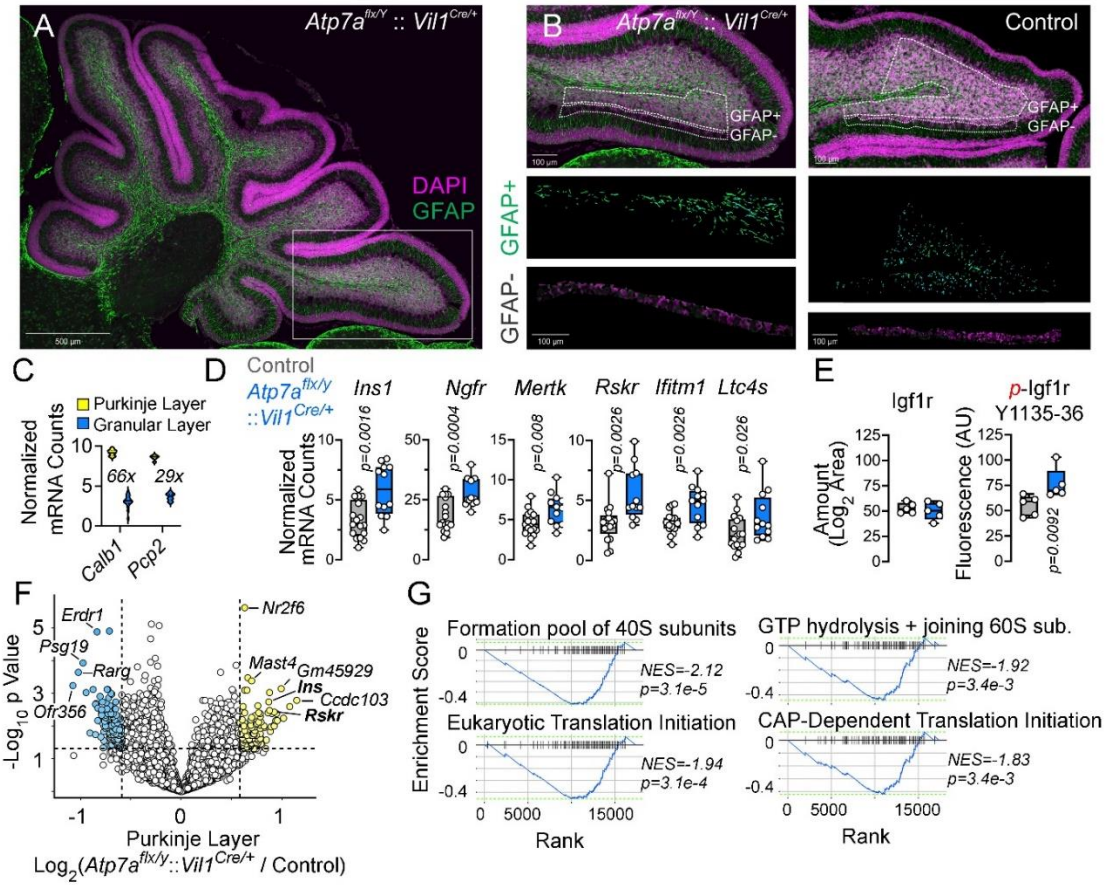

Figure S6-1. Spatial Transcriptomics Quality Controls and Descriptors. A. Sankey diagram depicts an overview of samples (n=58) showing their annotations. **B**. Sequencing quality as measured by saturation to ensure sensitivity of low expressor genes. Sequencing saturation measures sequencing depth for a sample defined as (1 – % Unique reads). Threshold above 50% is considered a reliable determination. 0 samples below the 50% threshold. **C**. Sequencing reads raw and normalized to the third quartile (Q3) to account for differences in cellularity, area of interest (AOI) size, or other variables. **D.** number of genes in different percentages of tissues expressed above LOQ2 (Limit of Quantitation), defined as the Geometric Mean of the negative probes, multiplied by the geometric standard deviation to the second power (^2). We assayed 19,963 genes across 58 AOIs. Of these 17,453 genes were expressed in 10% of AOIs and 10,290 genes expressed were expressed in 50% of AOIs. **E**. t-Distributed Stochastic Neighbor Embedding (t-SNE) of gene expression values per annotation. See Supplementary File 2 for raw data.

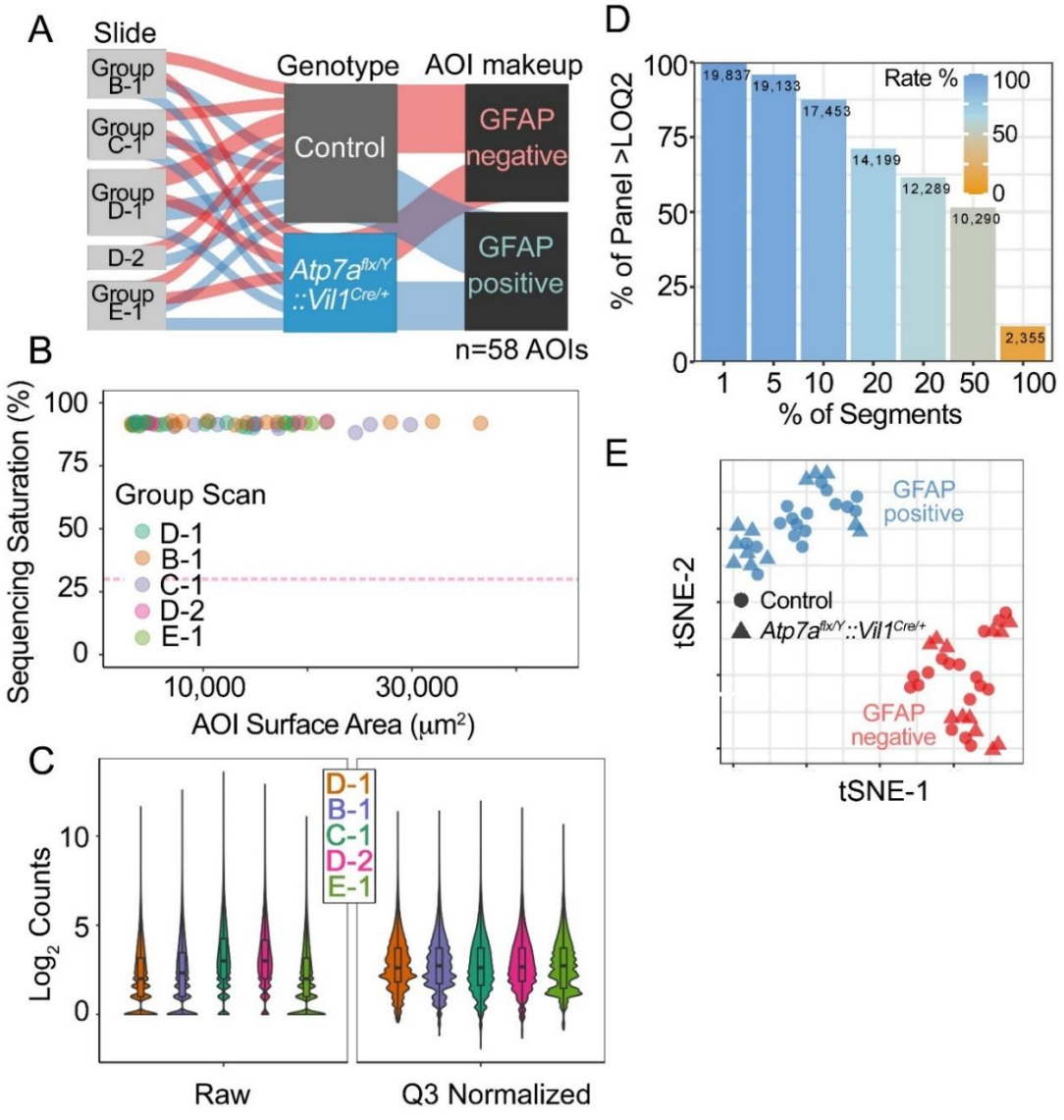

Figure S6-2. Cell type-specific gene expression in the cerebellar cortex in a presymptomatic Menkes mouse model. A. 63Cu and 64Zn quantification in the brains of *Atp7a*$^{flx/Y}$ :: *Vil1*$^{Cre/+}$ mice at P10, normalized to 32S and analyzed by two-sided permutation t-test (italicized numbers represent p values). **B.** Volcano plot of mRNAs differentially expressed between the Purkinje and granular layer of control mice. **C.** Expression of selected cell type-specific markers (96). **D.** Differential expression of all transcripts compared to cytoplasmic ribosome subunits mRNAs. Whiskers correspond to 5-95 percentile, box represents 25 and 75 percentile, horizontal line marks the mean. Shaded area demotes ±1.5 fold difference. **E.** Gene ontology analysis of transcripts more highly expressed in Purkinje cells than granular layer cells. MSigDB was queried with the ENRICHR engine. Fisher exact test followed by Benjamini-Hochberg correction. **F.** 294 of the 1881 transcripts more highly expressed in wild-type Purkinje cells are annotated to the MitoCarta3.0 knowledgebase. **G.** GSEA and NES enrichment score of genes differentially expressed in wild-type Purkinje cells and granular layer cells reveal enrichment in metabolic ontologies. **H.** Volcano plot of mRNAs differentially expressed in the granular layer in mutant *Atp7a*$^{flx/Y}$ :: *Vil1*$^{Cre/+}$ mice vs control. Yellow symbols mark genes with increased expression in the granular layer in mutant *Atp7a*$^{flx/Y}$ :: *Vil1*$^{Cre/+}$ mice. See Supplementary File 2 for raw data.

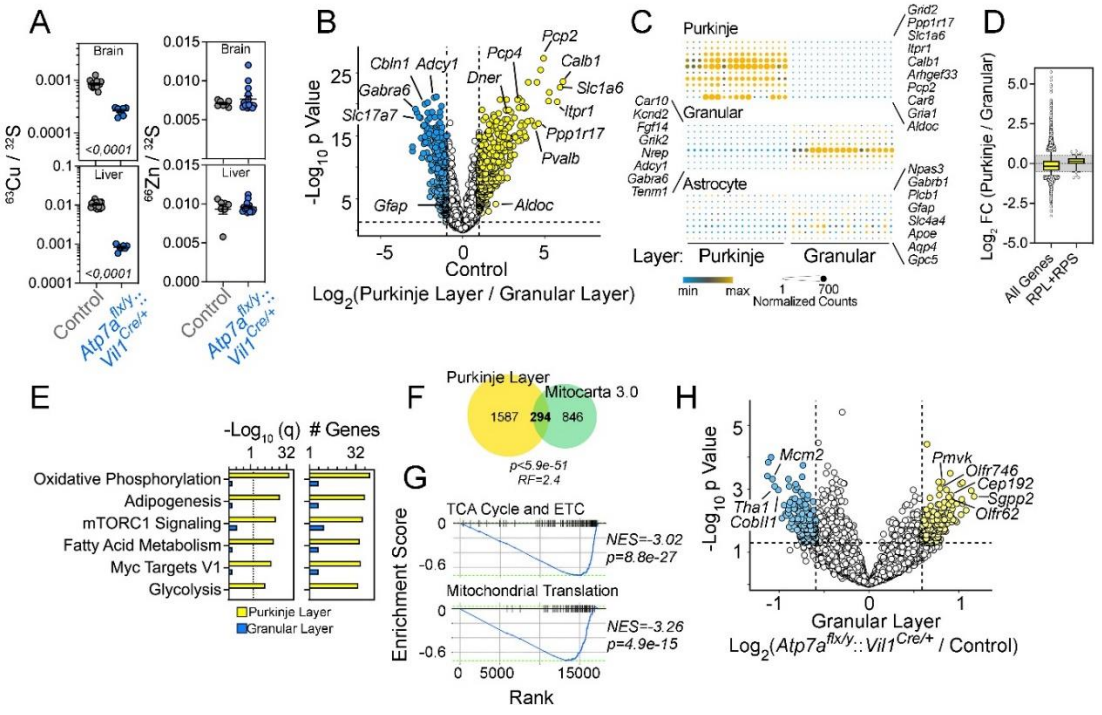

Figure S6-3. Respiratory complex subunit gene expression in a presymptomatic Menkes mouse model. A. Hierarchical clustering of all transcripts annotated to electron transport chain subunits according to MitoCarta 3.0 across genotypes and AOIs quantified. **B.** Principal component 1 of data presented in A for the Purkinje layer. Permutation t test. See Supplementary File 2 for raw data.

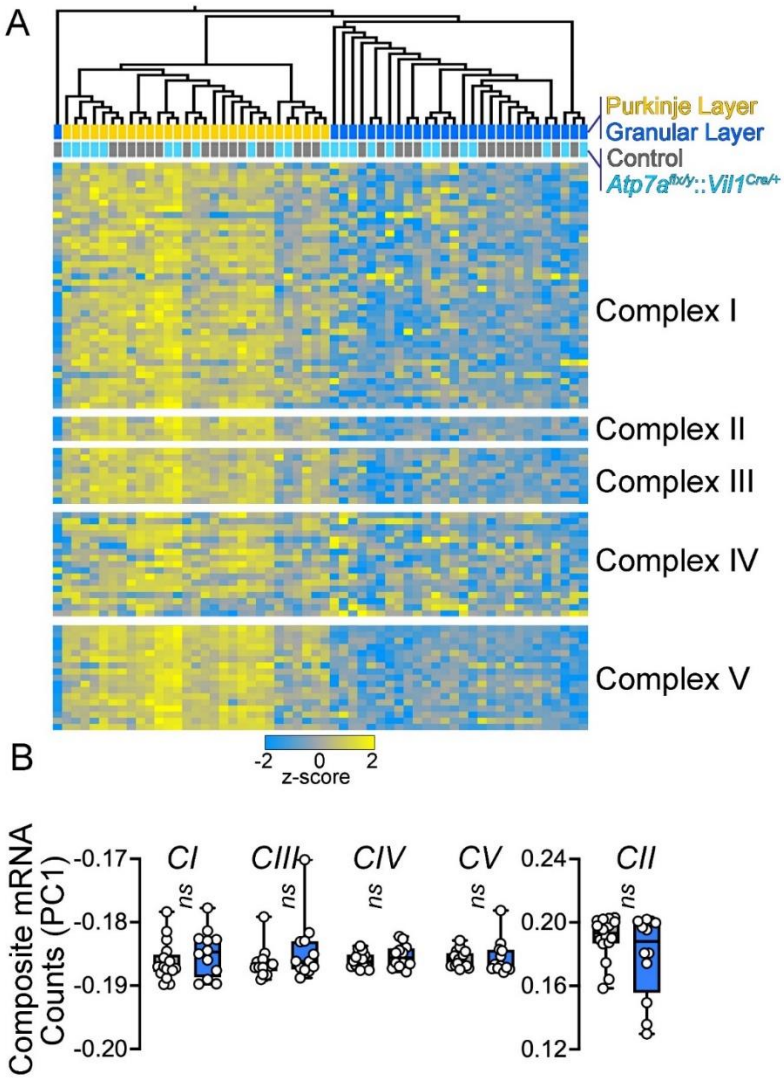

Figure 7. mTOR-dependent protein synthesis pathways ameliorate copper-depletion phenotypes in sensory neurons. A. Representative reconstructed dendritic arbors from live confocal images of C-IV da neurons of the specified genotypes labeled by GFP (see Table 3 and Methods.) Scale bar: 100 µm. Right panel depicts 400 µM circle used to distinguish proximal and distal dendrites (see Methods). **B.** Quantitative analysis of dendritic parameters in the specified genotypes: average branch length for the entire dendritic arbor or for the region distal to the soma (see Methods), dendritic field coverage, and total dendritic length. Each dot represents an independent animal. Average ± SEM. Italicized numbers represent q values (One-Way ANOVA, followed by Benjamini, Krieger, and Yekutieli multiple comparisons correction). **C.** Representative live confocal images of C-IV da neurons of the specified genotypes expressing a mitochondria-targeted GFP that were manually traced using a plasma membrane marker (CD4-tdTomato, not shown). Scale bar: 5 µm.

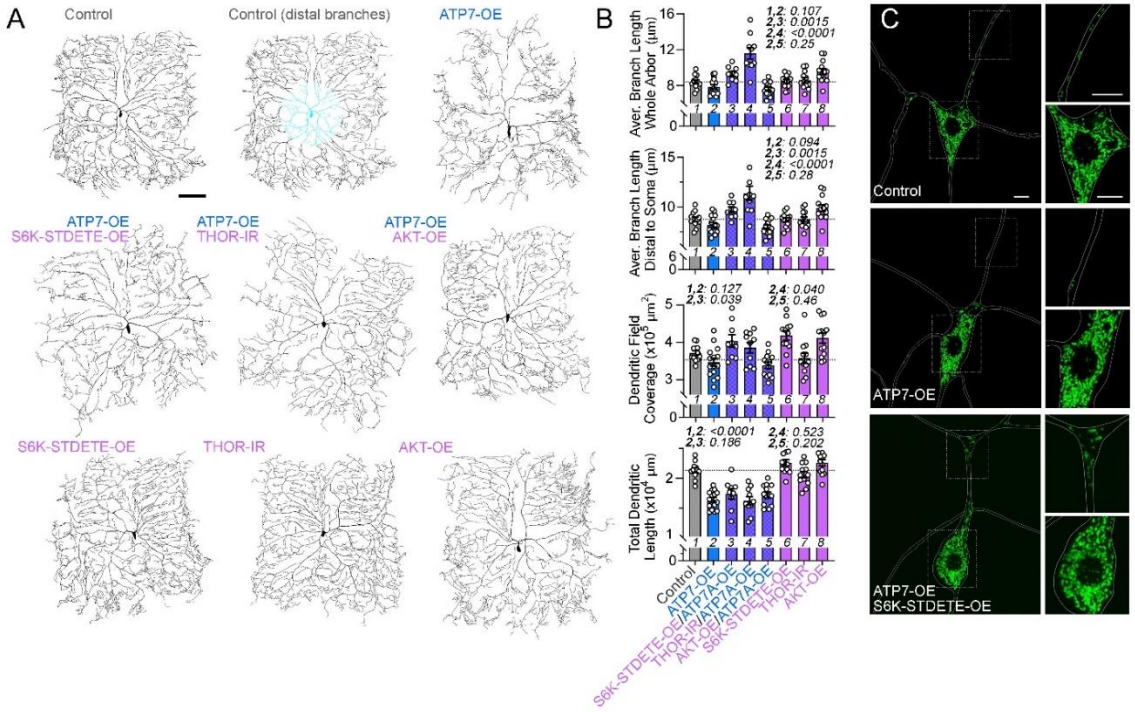

Figure S7. mTOR-Raptor-S6K pathway loss-of-function enhances copper-depletion phenotypes in *Drosophila* epidermis. Expression of wild type ATP7 and/or wild type or RNAi of different components of the mTOR pathway in the epidermis of the thoracic segment using the pnr-GAL4 driver in males and females (see Table 3 and Methods). Arrowheads point to 'dimples' in the dorsal aspect of ATP7-OE; S6K-IR males.

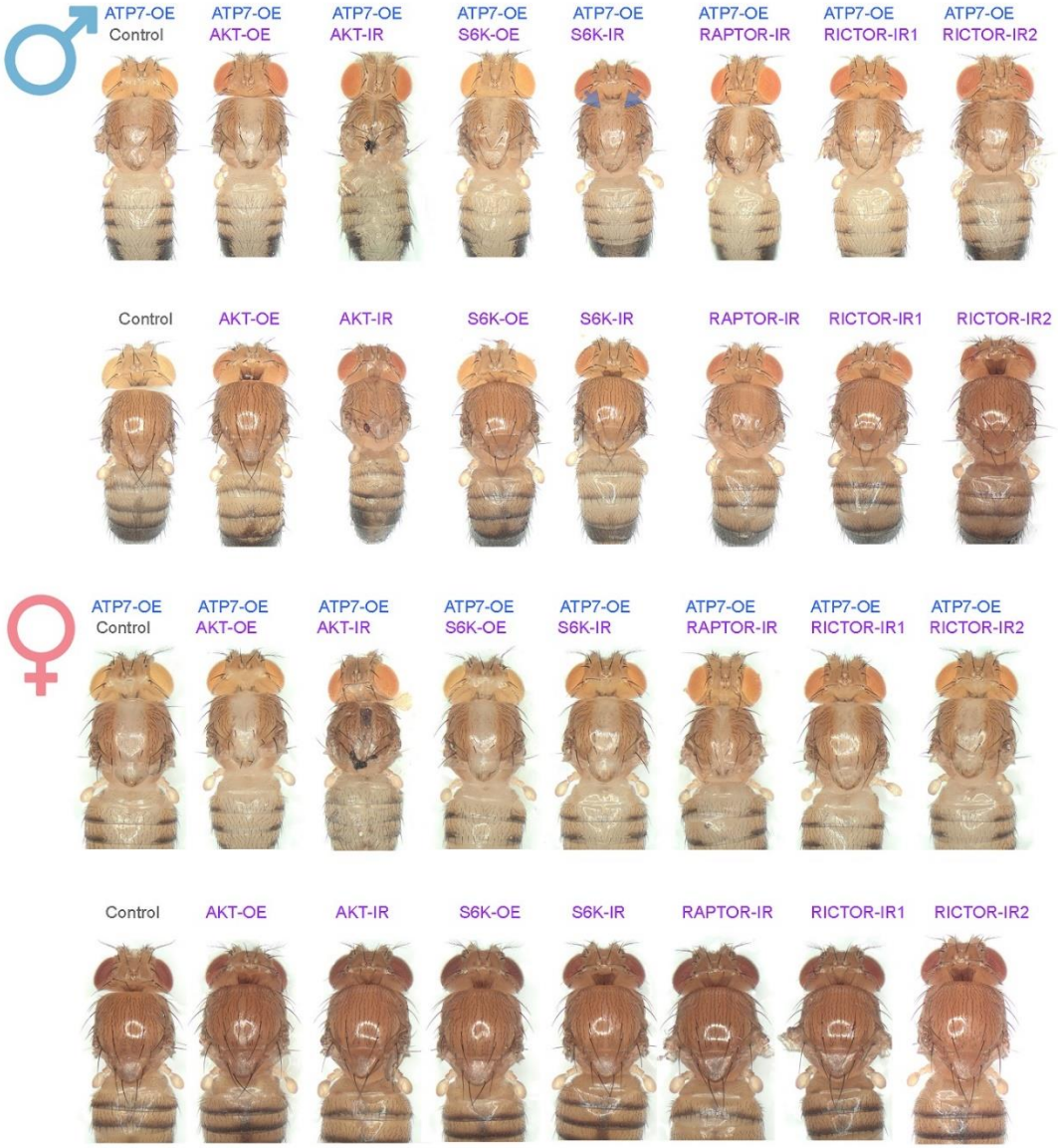

Table 1. Antibodies.

Antibody	Dilution	Catalog Number	RRID
Actin B	1:5000	Sigma-Aldrich A5441	AB_476744
ATP7A	1:500	NeuroMab 75-142	AB_10672736
CCS	1:500	ProteinTech 22802-1-AP	AB_2879172
COX17	1:500	ProteinTech 11464-1-AP	AB_2085109
COX4	1:1000	Cell Signaling 4850	AB_2085424
CTR1 (SLC31A1)	1:2000	ProteinTech 67221-1-IG	AB_2919440
DBH	1:500	Millipore AB1536	AB_2089474
DEPTOR	1:1000	Cell Signaling 11816	AB_2750575
GFAP-AF594	1:400	Cell Signaling 8152	AB_10998775
HSP90	1:1000	BD Biosciences 610418	AB_397798
mTOR	1:1000	Cell Signaling 2983	AB_2105622
mTOR pSer2448	1:1000	Cell Signaling 5536	AB_10691552
NDUFB11	1:500	Abcam ab183716	AB_2927481
OXPHOS mix	1:250	Abcam ab110412	AB_2847807
PERK (EIF2AK3)	1:1000	Cell Signaling 5683	AB_10841299
Puromycin	1:500	Sigma MABE342	AB_2737590
Raptor	1:1000	Cell Signaling 2280	AB_561245
Rictor	1:1000	Cell Signaling 2114	AB_2179963
S6K P70	1:1000	Cell Signaling 9202	AB_331676
S6K pThr389	1:1000	Cell Signaling 9234	AB_2269803
SDHA	1:1000	11998	AB_2750900
UQCRC2	1:500	Abcam ab14745	AB_2213640
Mouse IRDye 680RD	1:1000	LI-COR 926-68070	AB_10956588
mouse HRP	1:5000	A10668	AB_2534058
rabbit HRP	1:5000	G21234	AB_2536530

Table 2. Drugs.

Drug	Source/Cat. No	Storage/Stock	Concentration range
Elesclomol	VWR, 101758-608	1 mM, DMSO, -20C	1 nM - 1024 nM
Copper chloride	Sigma, 203149	120 mM, water, -20C	25 µM - 600 µM
BCS	Sigma, B1125	400 mM, DMSO, -20C	0.1 mM - 1.6 mM
Oligomycin	Sigma, 75351	10 mM, DMSO, -20C	1.0 µM
FCCP	Sigma, C2920	10 mM, DMSO, -20C	0.25 µM
Rotenone	Sigma, R8875	10 mM, DMSO, -20C	0.5 µM
Antimycin A	Sigma, A8674	10 mM, DMSO, -20C	0.5 µM
D-Glucose	Sigma, G8769	2.5M, 4C	10 mM
2-deoxyglucose	Sigma, D3179-1G	500 mM, Glycolysis Stress Test Media, -20C	50 mM
Emetine	Sigma, E2375	100 mM, DMSO, -20C	2 nM - 2500 nM
Puromycin	Sigma, P7255	10 mg/mL, DMSO, -20C	1 mg/mL
Insulin	Sigma, 91077C	1 mM, water, 4C	1.6 nM - 1000 nM
Torin-2	VWR, 103542-338	1 mM, DMSO, -20C	1 nM - 250 nM
Rapamycin	VWR, 101762-276	50 mM, DMSO, -20C	0.8 µM - 66 µM

Table 3. *Drosophila* strains.

Short name	Genotype	Source	Fig
ATP7-OE	UAS-ATP7-wt-FLAG	gift from RB	7,S7
mCD8-GFP	UAS-mCD8::GFP	Gift from YJ (135)	7
GAL4ppk1.9	$GAL4^{ppk1.9}$	Gift from YJ (135)	7
AKT-OE	y[1] w[1118]; P{w[+mC]=UAS-Akt.Exel}2	BDSC 8191	7
S6K-STDETE-OE	w[1118]; P{w[+mC]=UAS-S6k.STDETE}2	BDSC 6914	7
THOR-IR	y[1] sc[*] v[1] sev[21]; P{y[+t7.7] v[+t1.8]=TRiP.HMS01555}attP40	BDSC 36667	7
THOR-IR2	y[1] v[1]; P{y[+t7.7] v[+t1.8]=TRiP.HMS06007}attP40	BDSC 80427	-
MitoGFP	UAS-mito-HA-GFP	BDSC 8442	7
mCD8-RFP	UAS-mCD8::RFP	BDSC 32218	7
CD4-tdTOM	y[1] w[*]; Mi{y[+mDint2]=MIC}ND-15[MI10315]	BDSC 53837	7
CD4-tdGFP	y[1] w[*]; P{w[+mC]=UAS-CD4-tdGFP}8M2	BDSC 35839	7
Control	w^{1118}	BDSC 5905	S7
AKT-OE	y[1] w[1118]; P{w[+mC]=UAS-Akt.Exel}2	BDSC 8191	S7
AKT^{RNAi}	y[1] v[1]; P{y[+t7.7] v[+t1.8]=TRiP.HM04007}attP2	BDSC 31701	S7
S6K-OE	w[1118]; P{w[+mC]=UAS-S6k.M}2/CyO	BDSC 6910	S7
S6K-IR	y[1] v[1]; P{y[+t7.7] v[+t1.8]=TRiP.HMS02267}attP2	BDSC 41702	S7
RAPTOR-IR	y[1] v[1]; P{y[+t7.7] v[+t1.8]=TRiP.JF01088}attP2	BDSC 31529	S7
RICTOR-IR1	y[1] v[1]; P{y[+t7.7] v[+t1.8]=TRiP.JF01370}attP2	BDSC 31388	S7
RICTOR-IR2	y[1] sc[*] v[1] sev[21]; P{y[+t7.7] v[+t1.8]=TRiP.HMS01588}attP2	BDSC 36699	S7
pnr-GAL4	y[1] w[1118]; P{w[+mW.hs]=GawB}pnr[MD237]/TM3, P{w[+mC]=UAS-y.C}MC2, Ser[1]	BDSC 3039	S7

BDSC = Bloomington *Drosophila* Stock Center; VDRC = Vienna *Drosophila* Resource Center; RB = Richard Burke, Monash University, Australia

Supplementary File 1. Raw Data for CTR1 KO Cell Proteomics, Transcriptomics, and Gene Ontologies.

Supplementary File 2. Raw Data for Spatial Transcriptomics.

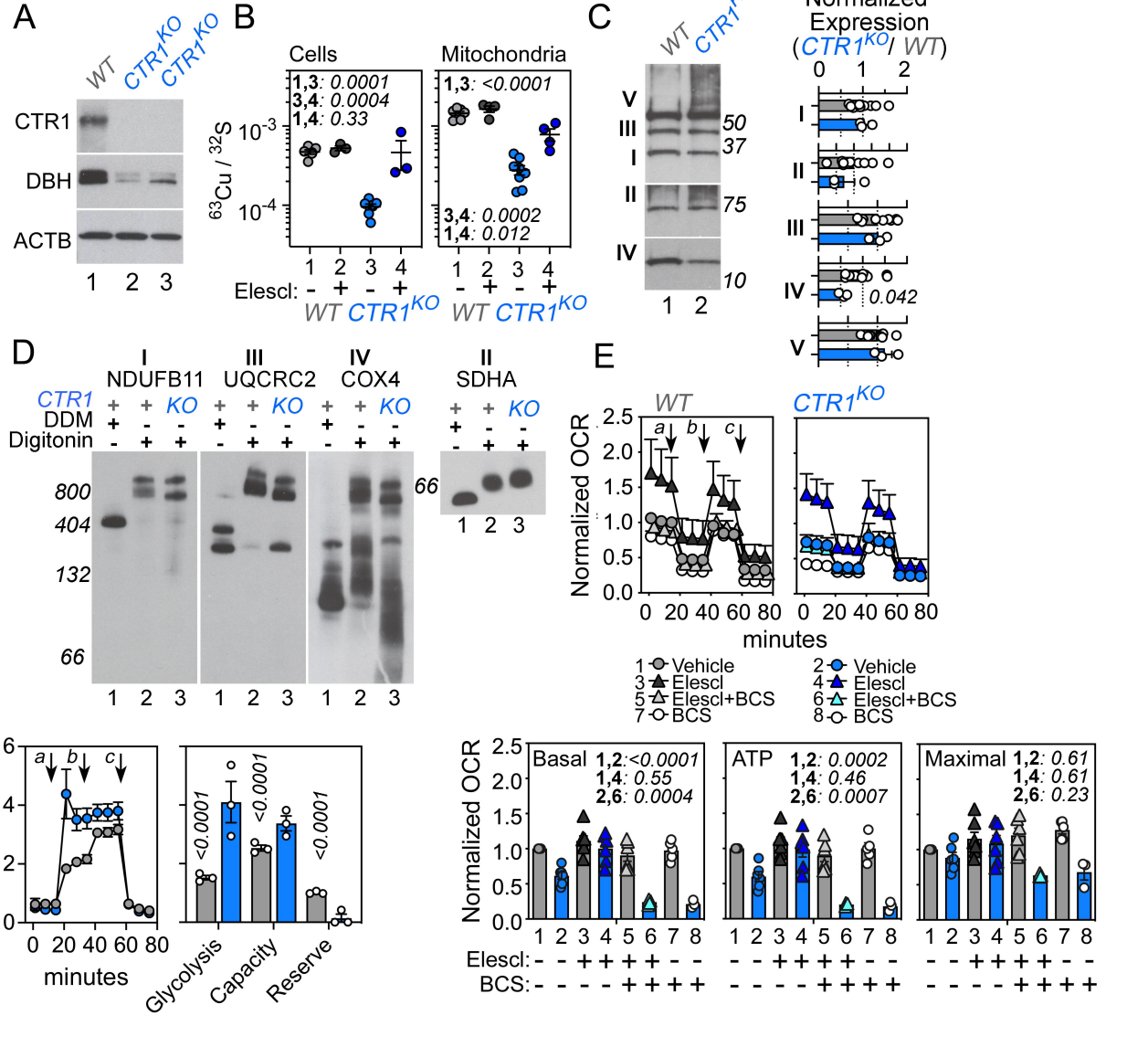
A
WT
CTR1KO
CTR1KO
CTR1
DBH
ACTB
1 2 3
B
Cells
Mitochondria
1,3: 0.0001
3,4: 0.0004
1,4: 0.33
1,3: <0.0001
3,4: 0.0002
1,4: 0.012
63Cu / 32S
10-3
10-4
1 2 3 4
Elescl: - + - +
WT CTR1KO
C
WT
CTR1KO
V
III
I
II
IV
50
37
75
10
1 2
Normalized Expression (CTR1KO / WT)
0 1 2
I
II
III
IV
0.042
V
D
I
NDUFB11
III
UQCRC2
IV
COX4
II
SDHA
CTR1 + + KO + + KO + + KO + + KO
DDM + - - + - - + - - + - -
Digitonin - + + - + + - + + - + +
800
404
132
66
66
1 2 3 1 2 3 1 2 3 1 2 3
E
WT
CTR1KO
Normalized OCR
a
b
c
0.0 0.5 1.0 1.5 2.0 2.5
0 20 40 60 80
minutes
1 Vehicle
3 Elescl
5 Elescl+BCS
7 BCS
2 Vehicle
4 Elescl
6 Elescl+BCS
8 BCS
F
ECAR (mpH/min/µg)
0 2 4 6
a
b
c
0 20 40 60 80
minutes
<0.0001
<0.0001
<0.0001
Glycolysis
Capacity
Reserve
Normalized OCR
Basal 1,2:<0.0001 1,4: 0.55 2,6: 0.0004
ATP 1,2: 0.0002 1,4: 0.46 2,6: 0.0007
Maximal 1,2: 0.61 1,4: 0.61 2,6: 0.23
0.0 0.5 1.0 1.5 2.0 2.5
1 2 3 4 5 6 7 8
Elescl: - - + + + + - -
BCS: - - - - + + + +

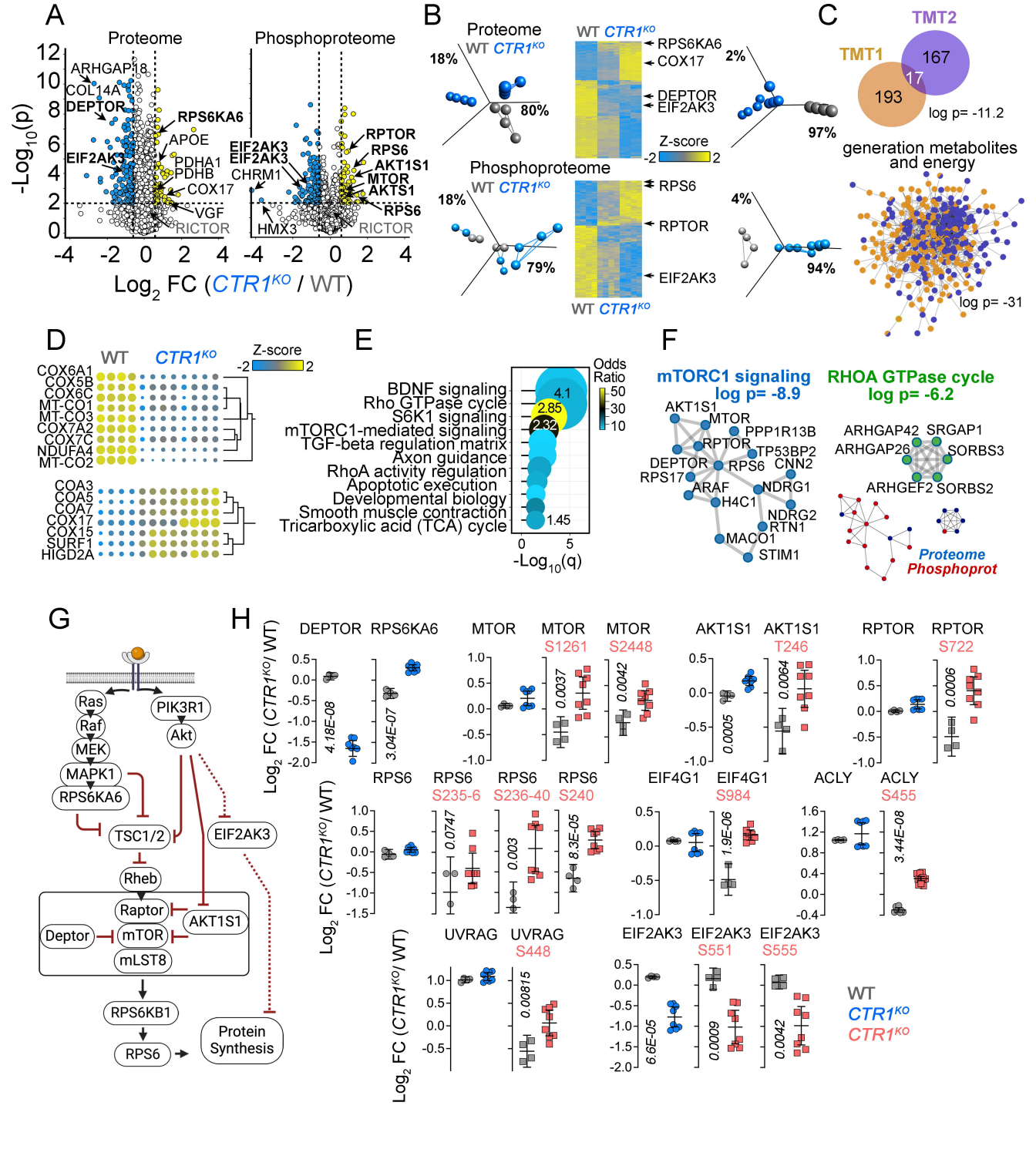
A
Proteome
Phosphoproteome
-Log10(p)
Log2 FC (CTR1KO / WT)
ARHGAP18
COL14A
DEPTOR
RPS6KA6
APOE
EIF2AK3
PDHA1
PDHB
COX17
VGF
RICTOR
EIF2AK3
EIF2AK3
CHRM1
RPTOR
RPS6
AKT1S1
MTOR
AKTS1
RPS6
HMX3
RICTOR
B
Proteome
WT CTR1KO
18%
80%
Phosphoproteome
WT CTR1KO
18%
79%
WT CTR1KO
RPS6KA6
COX17
DEPTOR
EIF2AK3
Z-score
-2
2
RPS6
RPTOR
EIF2AK3
WT CTR1KO
2%
97%
4%
94%
C
TMT2
TMT1
167
17
193
log p= -11.2
generation metabolites and energy
log p= -31
D
WT
CTR1KO
Z-score
-2
2
COX6A1
COX5B
COX6C
MT-CO1
MT-CO3
COX7A2
COX7C
NDUFA4
MT-CO2
COA3
COA5
COA7
COX17
COX15
SURF1
HIGD2A
E
BDNF signaling
Rho GTPase cycle
S6K1 signaling
mTORC1-mediated signaling
TGF-beta regulation matrix
Axon guidance
RhoA activity regulation
Apoptotic execution
Developmental biology
Smooth muscle contraction
Tricarboxylic acid (TCA) cycle
4.1
2.85
2.32
1.45
Odds Ratio
50
30
10
0
5
-Log10(q)
F
mTORC1 signaling
log p= -8.9
AKT1S1
MTOR
PPP1R13B
RPTOR
TP53BP2
DEPTOR
RPS6
CNN2
RPS17
ARAF
NDRG1
H4C1
NDRG2
RTN1
MACO1
STIM1
RHOA GTPase cycle
log p= -6.2
ARHGAP42
SRGAP1
ARHGAP26
SORBS3
ARHGEF2
SORBS2
Proteome
Phosphoprot
G
Ras
Raf
MEK
MAPK1
RPS6KA6
PIK3R1
Akt
TSC1/2
EIF2AK3
Rheb
Raptor
Deptor
mTOR
AKT1S1
mLST8
RPS6KB1
RPS6
Protein Synthesis
H
Log2 FC (CTR1KO/ WT)
DEPTOR
RPS6KA6
4.18E-08
3.04E-07
MTOR
MTOR S1261
MTOR S2448
0.0037
0.0042
AKT1S1
AKT1S1 T246
0.0005
0.0064
RPTOR
RPTOR S722
0.0006
RPS6
RPS6 S235-6
RPS6 S236-40
RPS6 S240
0.0747
0.003
8.3E-05
EIF4G1
EIF4G1 S984
1.9E-06
ACLY
ACLY S455
3.44E-08
UVRAG
UVRAG S448
0.00815
EIF2AK3
EIF2AK3 S551
EIF2AK3 S555
6.6E-05
0.0009
0.0042
WT
CTR1KO
CTR1KO

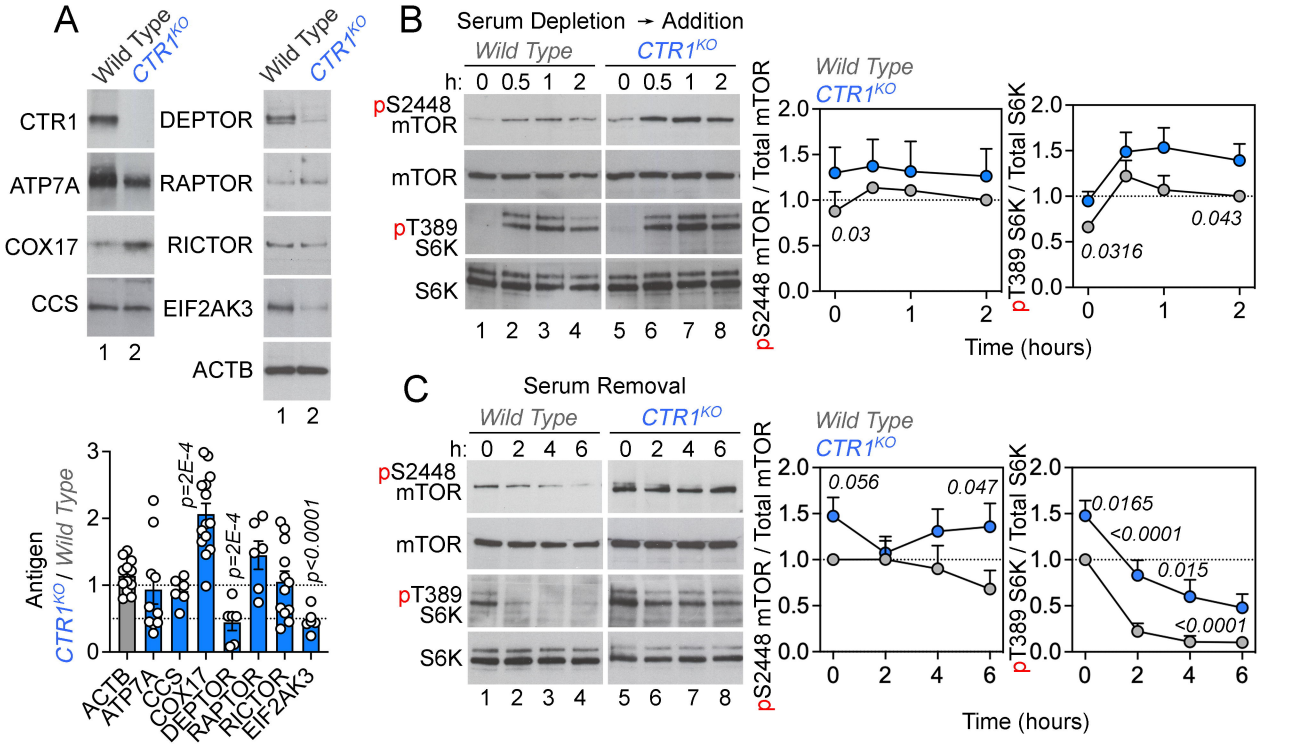
A
Wild Type
CTR1KO
CTR1
ATP7A
COX17
CCS
DEPTOR
RAPTOR
RICTOR
EIF2AK3
ACTB
1 2
Antigen
CTR1KO / Wild Type
p=2E-4
p=2E-4
p<0.0001
ACTB
ATP7A
CCS
COX17
DEPTOR
RAPTOR
RICTOR
EIF2AK3
B
Serum Depletion → Addition
Wild Type
CTR1KO
h: 0 0.5 1 2 0 0.5 1 2
pS2448 mTOR
mTOR
pT389 S6K
S6K
1 2 3 4 5 6 7 8
pS2448 mTOR / Total mTOR
0.03
pT389 S6K / Total S6K
0.0316
0.043
Time (hours)
C
Serum Removal
Wild Type
CTR1KO
h: 0 2 4 6 0 2 4 6
pS2448 mTOR
mTOR
pT389 S6K
S6K
1 2 3 4 5 6 7 8
pS2448 mTOR / Total mTOR
0.056
0.047
pT389 S6K / Total S6K
0.0165
<0.0001
0.015
<0.0001
Time (hours)

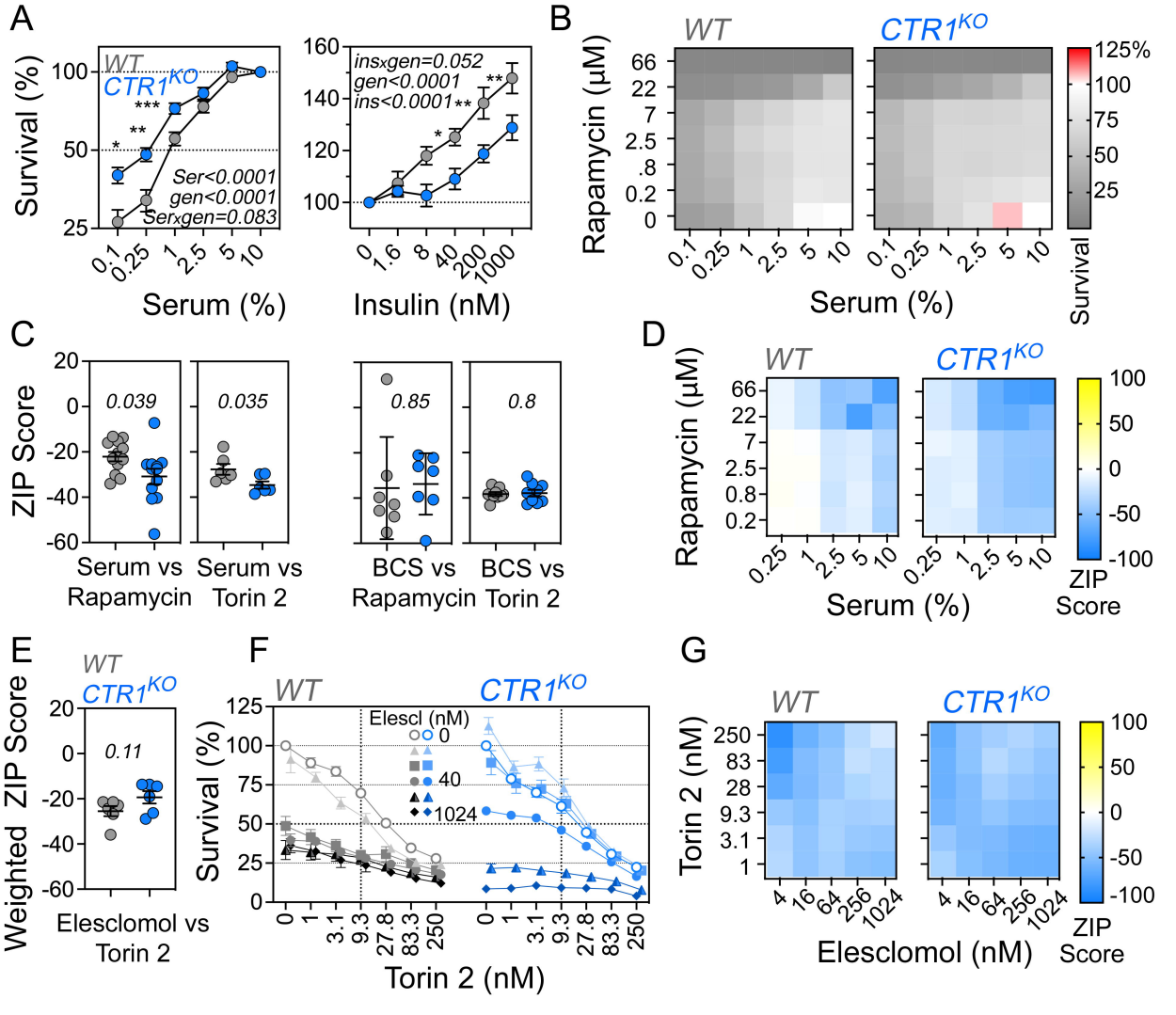
A
WT
CTR1KO
Survival (%)
Serum (%)
Ser<0.0001
gen<0.0001
Ser×gen=0.083
Insulin (nM)
ins×gen=0.052
gen<0.0001
ins<0.0001
B
WT
CTR1KO
Rapamycin (μM)
Serum (%)
Survival
C
ZIP Score
0.039
0.035
0.85
0.8
Serum vs Rapamycin
Serum vs Torin 2
BCS vs Rapamycin
BCS vs Torin 2
D
WT
CTR1KO
Rapamycin (μM)
Serum (%)
ZIP Score
E
WT
CTR1KO
Weighted ZIP Score
0.11
Elesclomol vs Torin 2
F
WT
CTR1KO
Survival (%)
Elescl (nM)
0
40
1024
Torin 2 (nM)
G
WT
CTR1KO
Torin 2 (nM)
Elesclomol (nM)
ZIP Score

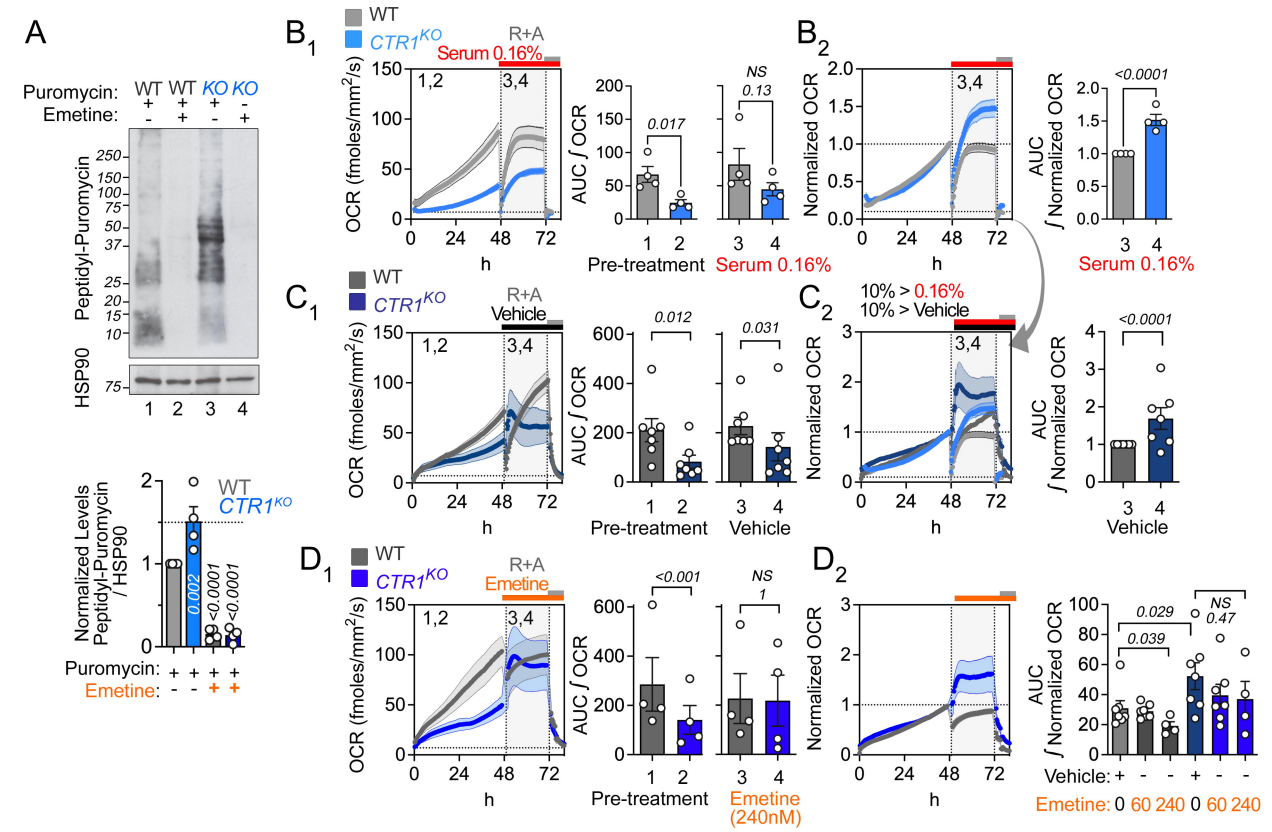
A
Puromycin: WT WT KO KO
Emetine: + + + -
- + - +
250
150
100
75
50
37
25
20
15
10
Peptidyl-Puromycin
HSP90
75
1 2 3 4
Normalized Levels Peptidyl-Puromycin / HSP90
WT
CTR1KO
0.002
<0.0001
<0.0001
Puromycin: + + + +
Emetine: - - + +
B1
WT
CTR1KO
R+A
Serum 0.16%
OCR (fmoles/mm2/s)
1,2
3,4
h
AUC ∫ OCR
0.017
NS
0.13
Pre-treatment
Serum 0.16%
B2
Normalized OCR
AUC ∫ Normalized OCR
<0.0001
Serum 0.16%
C1
Vehicle
0.012
0.031
Pre-treatment
Vehicle
C2
10% > 0.16%
10% > Vehicle
<0.0001
Vehicle
D1
Emetine
<0.001
NS
1
Pre-treatment
Emetine (240nM)
D2
0.029
0.039
NS
0.47
Vehicle: + - - + - -
Emetine: 0 60 240 0 60 240

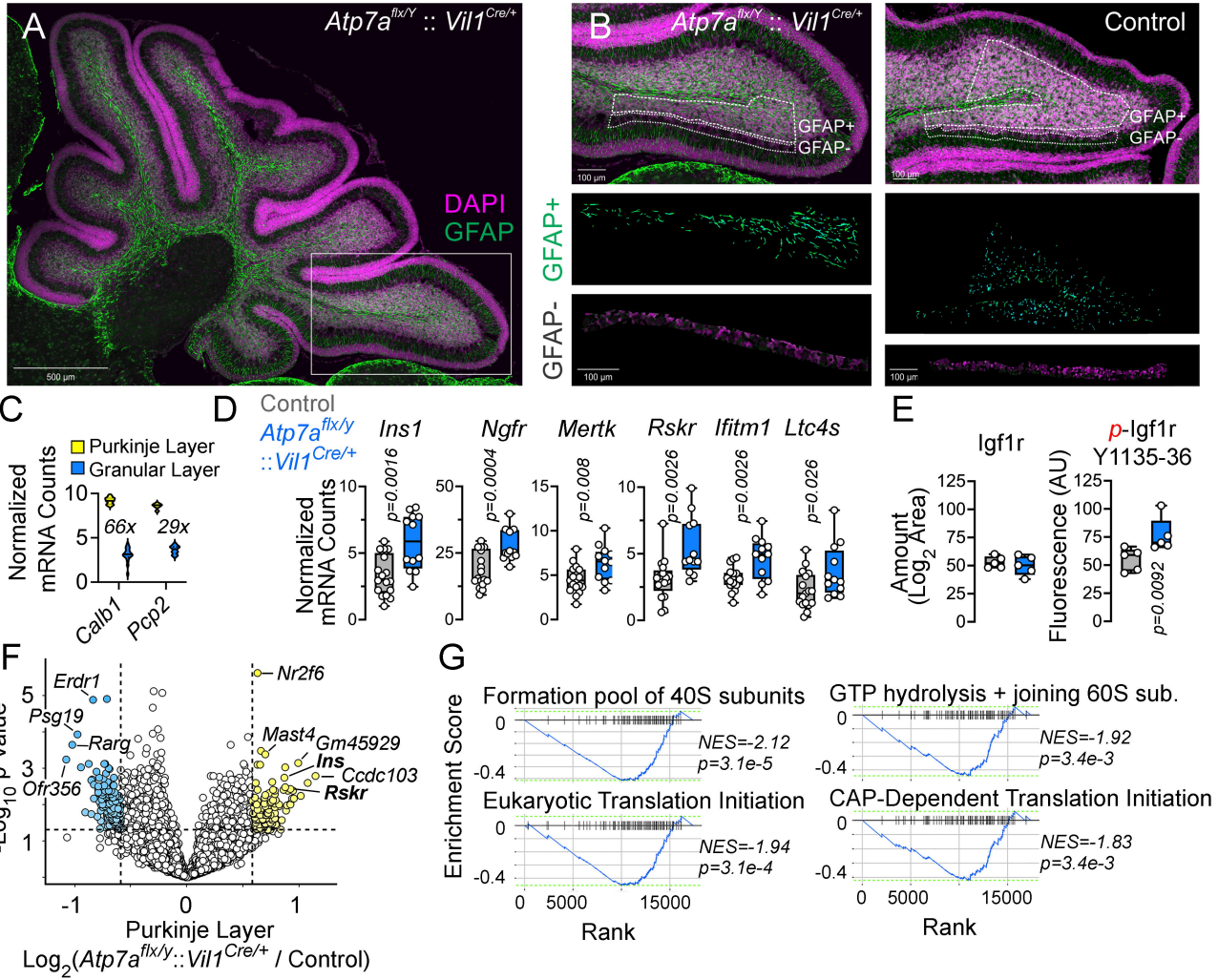
A
Atp7a flx/Y :: Vil1 Cre/+
DAPI
GFAP
500 µm
B
Atp7a flx/Y :: Vil1 Cre/+
GFAP+
GFAP-
100 µm
Control
GFAP+
GFAP-
100 µm
GFAP+
GFAP-
100 µm
100 µm
C
Purkinje Layer
Granular Layer
Normalized mRNA Counts
66x
29x
Calb1
Pcp2
D
Control
Atp7a flx/y ::Vil1 Cre/+
Normalized mRNA Counts
Ins1
p=0.0016
Ngfr
p=0.0004
Mertk
p=0.008
Rskr
p=0.0026
Ifitm1
p=0.0026
Ltc4s
p=0.026
E
Igf1r
Amount (Log2 Area)
p-Igf1r Y1135-36
Fluorescence (AU)
p=0.0092
F
Erdr1
Psg19
Rarg
Ofr356
Nr2f6
Mast4
Gm45929
Ins
Ccdc103
Rskr
-Log10 p Value
Purkinje Layer
Log2(Atp7a flx/y::Vil1 Cre/+ / Control)
G
Formation pool of 40S subunits
NES=-2.12
p=3.1e-5
GTP hydrolysis + joining 60S sub.
NES=-1.92
p=3.4e-3
Eukaryotic Translation Initiation
NES=-1.94
p=3.1e-4
CAP-Dependent Translation Initiation
NES=-1.83
p=3.4e-3
Enrichment Score
Rank
Rank

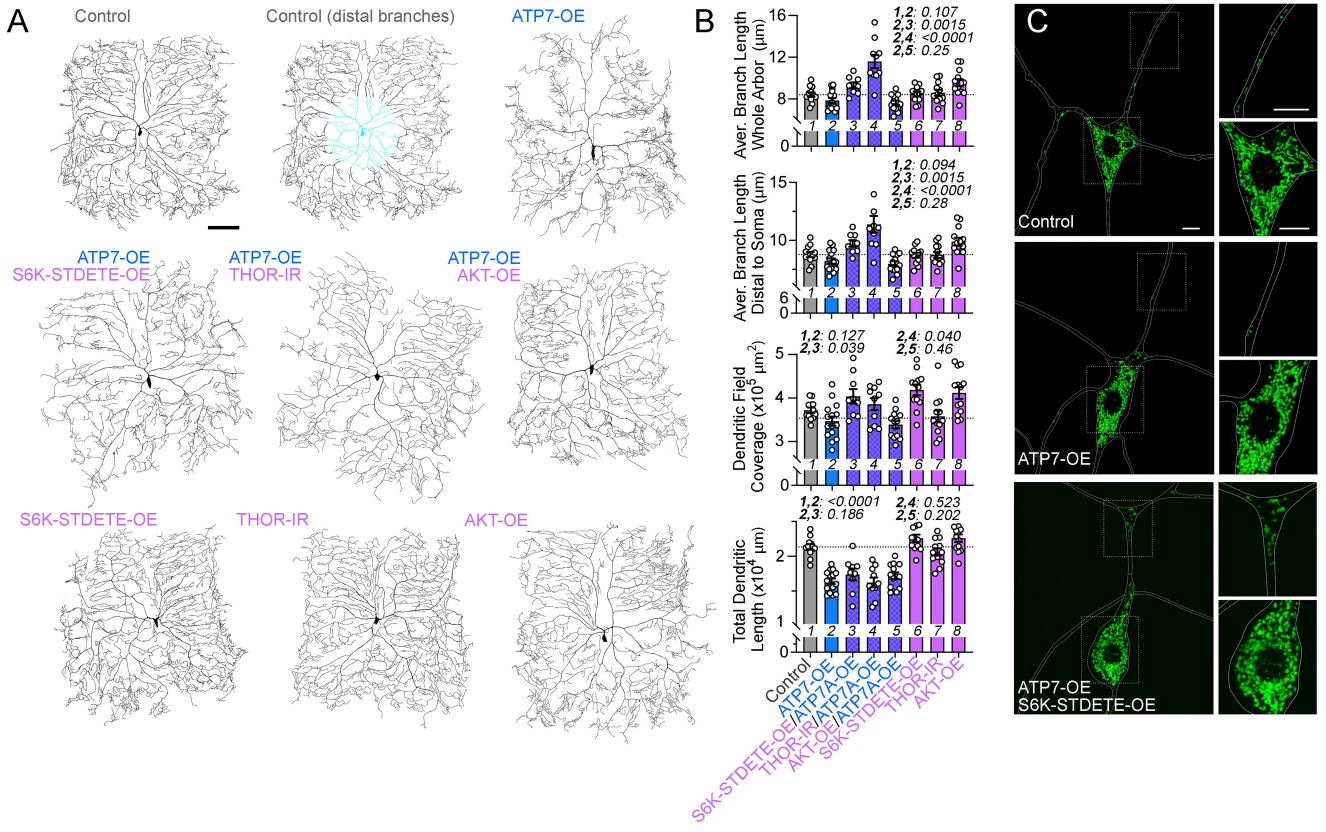
A
Control
Control (distal branches)
ATP7-OE
ATP7-OE
S6K-STDETE-OE
ATP7-OE
THOR-IR
ATP7-OE
AKT-OE
S6K-STDETE-OE
THOR-IR
AKT-OE
B
Aver. Branch Length Whole Arbor (µm)
1,2: 0.107
2,3: 0.0015
2,4: <0.0001
2,5: 0.25
Aver. Branch Length Distal to Soma (µm)
1,2: 0.094
2,3: 0.0015
2,4: <0.0001
2,5: 0.28
Dendritic Field Coverage (x10³ µm²)
1,2: 0.127
2,3: 0.039
2,4: 0.040
2,5: 0.46
Total Dendritic Length (x10⁴ µm)
1,2: <0.0001
2,3: 0.186
2,4: 0.523
2,5: 0.202
Control
ATP7-OE
S6K-STDETE-OE
ATP7-OE
THOR-IR
ATP7-OE
AKT-OE
ATP7-OE
S6K-STDETE-OE
THOR-IR
AKT-OE
C
Control
ATP7-OE
ATP7-OE
S6K-STDETE-OE